



Escola de Camins
Escola Tècnica Superior d'Enginyeria de Camins, Canals i Ports
UPC BARCELONATECH

Numerical Analysis of Interior Aircraft Structures made of Composite Materials

Treball realitzat per:

Lei Pan

Dirigit per:

Xavier Martínez Garcia

Màster en:

**MASTER'S DEGREE IN NUMERICAL METHODS IN
ENGINEERING**

Barcelona, 05, June 2019

ETSECCPB - Barcelona School of Civil Engineering

TREBALL FINAL DE MÀSTER

Contents

Contents-----	I
Abstract -----	1
1 Introduction -----	2
1.1 Background and Motivation -----	2
1.2 Objectives-----	2
1.3 Outline -----	3
2 Methodology -----	4
2.1 Finite Element Method -----	4
2.2 Multiscale Homogenization-----	6
2.2.1 General Background -----	6
2.2.2 First-order Homogenization-----	7
2.2.3 FE ² homogenization -----	10
3 Analysis of the beam -----	12
3.1 Geometry and boundary conditions-----	12
3.1.1 Beam model and mesh-----	12
3.2 Analysis considering an isotropic material -----	13
3.2.1 Material and basic settings -----	13
3.2.2 Midspan centralized load case -----	13
3.2.3 Uniform load case -----	15
3.3 Analysis with a multiscale procedure-----	16
3.3.1 Material, basic settings and RVE-----	16
3.3.2 Midspan centralized load case -----	17
3.3.3 Uniform load case -----	18
4 Analysis of the airplane interior cabin bin (Hatrack)-----	21
4.1 Geometry, boundary conditions and sandwich structure -----	21
4.1.1 Model, boundary conditions -----	21
4.1.2 Mesh, basic settings -----	22
4.1.3 Sandwich structure -----	22

Contents

4.2	Analysis considering isotropic materials	23
4.2.1	Materials	23
4.2.2	Results of load case 1	24
4.2.3	Results of load case 2	37
4.2.4	Conclusions	48
4.3	Analysis with a multiscale procedure	50
4.3.1	Material, RVEs	50
4.3.2	Results	52
4.3.3	Conclusions	72
5	Conclusions	73
6	References	74

Abstract

This work is focusing on using the numerical methods based on finite element method and multiscale analysis to study the aircraft structures made of eco-composite materials. In order to achieve this purpose, the PLCd code and the GiD pre/postprocess software have been introduced into this work. Before the simulations, the theories of FEM, multiscale analysis and FE^2 homogenization procedure have been discussed. The validations of PLCd code is conducted through testing the midspan tension stresses of the simple supported beam considering isotropic material under two load cases. The solutions given by PLCd code show that the errors are convergent with the increasing number of elements, no matter which method, with or without multiscale analysis procedure, is used. Another finding is that using quadratic elements will be more accurate compared to linear elements. And the stress concentration phenomenon has occurred in the results. The simulations of the cabin bin with isotropic materials under two load cases are conducted to study the stress field and the displacement field. The first load case corresponds to having the cabin bin completely loaded, while the second one corresponds to have only half of the cabin bin loaded. The results give the conclusion that the load case 1 is more dangerous. For the sandwich structure, the cores have undertaken much smaller stresses. And the results of the stress field of the cabin bin are meaningful for us since we can take measurements to avoid the damages on the areas where the stresses are large. The areas having large stresses include the upside boundary condition areas on the sides, the bottom boundary condition areas on the bottom plate and the back part, and the cross areas between the bottom plate and sides. Then the eco-composites have been used in the cabin bin. The results of the simulation show that the application of the honeycomb structure to the core parts will increase the stresses on it because of its large empty spaces. Consequently, we need to use highly stiff and highly strong material in the core parts to avoid damages. For the skins, the application of the eco-composites will help the structure to decrease the stresses on them. And the stresses on the cabin bin with isotropic materials or eco-composites are both lower than the stress thresholds of corresponding materials.

Key Words: finite element method, composite structure, multiscale analysis, sandwich structure

1 Introduction

1.1 Background and Motivation

Nowadays, the composite materials have already been widely implemented in aircrafts to build lightweight structures. Since the composite materials possess excellent mechanical properties like high stiffness while they are much lighter compared to traditionally used materials. For instance, steels or aluminums. The important role of composite materials in aircraft industry leads to the reduction of fuel consumption and increased capability of carrying more clients. However, these composites made of carbon-fibers reinforced plastics (CFRP) or glass-fibers reinforced plastics (GFRP) all need huge energy consumption in their producing procedures, which has limited their opportunities to be more economical. Furthermore, the high cost spent on the recycling of these composite materials is another negative factor. Consequently, with the endless demanding for more efficient and economical aircrafts, people need to seek other possibilities to solve these problems existing in the producing and using phases.

Consequently, the ecologically improved renewable composite materials are under investigations in order to avoid the problems mentioned above about CFRP and GFRP. Following works are parts of the ECO-COMPASS project whose target is to develop ecological composite materials that can also be renewed [1]. Because of the lacks of enough researches on the ecological composite materials and the caring about safety, ECO-COMPASS project focuses on implementing ecological composite materials on the interior and secondary structures on the aircrafts.

To achieve the aim of designing structures with minimal cost on certification tests, numerical techniques should be involved in our analysis stage. In this work, finite element method (FEM) is used with the code PLCd [2], developed for solving composite material problems, on GiD pre/postprocess platform.

1.2 Objectives

The main objective of this work is to simulate the cabin bin, made of sandwich structure, by using the multiscale analysis method. The following objectives are achieved through the conduction of this work:

- i) Presenting the multiscale homogenization formulations and the FE^2 homogenization procedure, which are the theories of the multiscale analysis of PLCd code.
- ii) Conducting the validations of the PLCd code by simulating a simple supported beam to prove its accuracy.
- iii) Simulating the cabin bin with isotropic materials to study its displacement field and stress field under different load cases. Comparing the results of different load cases to find which load case is more dangerous.
- iv) Simulating the cabin bin with the eco-composites by using the multiscale analysis procedure to study its displacement field and stress field. Through the comparison with the results of using isotropic material, the differences of using the eco-composites will be found.

1.3 Outline

The following contents are divided to 3 chapters to give a comprehensive view of this work.

In chapter 2, the methodologies related to this work have been introduced. The section 2.1 has taken the Laplace equation as an example to present the basic theory and procedure of finite element method. The section 2.2 that introduces the theory of multiscale analysis has 3 parts. The part 2.2.1 describes the general background of the multiscale analysis. Then the first-order homogenization theory and its formulations are shown in part 2.2.2. The last part of section 2.2 has presented the FE^2 homogenization algorithm.

In chapter 3, the simulations of the beam are shown, which is aimed at learning the capabilities and the formulations that have been included in this work. The section 3.1 gives the geometry and boundary conditions of the beam. And the following section 3.2 has conducted the first analysis of the beam with isotropic material to learn the program features, mesh requirements and the expected precision on the results. The last section 3.3 is the second analysis of beam conducted by using the multiscale analysis procedure. And the representative volume element used in this case is corresponding to the isotropic material in section 3.2. Under this situation, the comparison of the results obtained in section 3.2 and section 3.3 is analyzed.

The chapter 4, which has shown the simulations of the cabin bin, is following the same structure of chapter 3. The geometry and boundary conditions of the cabin bin are presented in section 4.1. In section 4.2, in order to learn about the performance of the structure of the cabin bin, the first analysis of the cabin bin is conducted by considering isotropic materials. In this case, the panel with sandwich structure of the cabin bin has glass fiber skins (Considered as isotropic material) and a foam core. The last section 4.3 has replaced the isotropic materials used in section 4.2 with eco-composites and the multiscale analysis procedure is used to study the complex internal micro-structure of these materials. The results are shown in section 4.3.

Chapter 5 gives some conclusions from the results obtained in above contents.

2 Methodology

The constitutive laws which are suitable for simple materials are no longer useful when it comes to solving more complicated composite materials. This new demand, building appropriate constitutive formulations for composite materials, has promoted several developments to appear in past decades.

Truesdell and Toupin [3] proposed classical mixing theory. Then, other researchers extended this theory by editing its compatibility assumption to make it be capable of solving any reinforced composite. The Serial-Parallel theory developed by S. Oller and E. Onate [4, 5] has taken into account the contribution from serial direction while the classical theory only considers the parallel direction's effect. Besides the mixing theories, multiscale homogenization method [6] is another option to help us analyze composite materials. The typical feature of multiscale homogenization is the concept of representative volume element (RVE) [7], which is the bridge between macroscale and microscale. RVE should be small enough compared to global domain but also needs to fulfill the request that it can represent the material's properties.

Finite element method is the numerical technique chosen for our work to solve the composite materials structural model based on above serial-parallel and multiscale homogenization theories.

2.1 Finite Element Method

The finite element method (FEM) is a numerical technique for solving partial differential equations [8] established in numerous scientific areas like solid and fluid mechanics, electromagnetics, thermal problems, etc. Through several decades' developments, FEM analysis has shown its unique and powerful charm by enabling us to get accurate approximated solutions without conducting expensive experiments in our research and engineering projects. In this work, the FEM is used to simulate the composite materials structure to help us analyze its stresses and displacements under particular load cases. Following contents briefly introduce the theory of FEM, taking Laplace equation as an example.

Considering the Laplace equation on one dimension:

$$-\Delta u = f \quad \text{on } \Omega \quad (2.1)$$

With boundary conditions:

$$u = u_D \quad \text{on } \partial\Omega_D \quad (2.2)$$

$$\partial_n u = q \quad \text{on } \partial\Omega_N \quad (2.3)$$

Above is the strong form of Laplace equation. Let's consider the simplified situation:

$$u_D = 0 \quad \text{and} \quad \Omega = \Omega_D \quad (2.4)$$

We multiply Laplace equation with a test function v and integrate on Ω :

Methodology

$$-\int_{\Omega} v \Delta u dx = \int_{\Omega} v f dx \quad \text{on } \Omega \quad (2.5)$$

Integrating by parts with the assumption that $v = 0$ on $\partial\Omega_D$:

$$\int_{\Omega} \nabla v \cdot \nabla u dx = \int_{\Omega} v f dx \quad \text{on } \Omega \quad (2.6)$$

We can define the following spaces:

$$L^2(\Omega) = \left\{ u(x): \int_{\Omega} u^2 dx < \infty \right\} \quad (2.7)$$

$$H^1(\Omega) = \{u \in L^2(\Omega): |\nabla u| \in L^2(\Omega)\} \quad \text{and} \quad H_0^1(\Omega) = \{u \in H^1(\Omega): u_{\partial\Omega_D} = 0\} \quad (2.8)$$

Then, the weak form of Laplace equation which is more general:

$$\text{Find } u \in H_0^1(\Omega): \int_{\Omega} \nabla v \cdot \nabla u dx = \int_{\Omega} v f dx, \quad \forall v \in H_0^1(\Omega) \quad (2.9)$$

In order to solve the weak form, we need to replace space $H_0^1(\Omega)$ with finite-dimensional subset:

$$V \equiv H_0^1(\Omega) \quad (2.10)$$

Through the change of space, we get the discrete form of the Laplace equation:

$$\text{Find } u \in V: \int_{\Omega} \nabla v \cdot \nabla u dx = \int_{\Omega} v f dx, \quad \forall v \in V \quad (2.11)$$

By using finite element mesh we can construct the space V :

$$V = \{N_1, N_2, \dots, N_i, \dots, N_n\} \quad (2.12)$$

Where the N_i is the shape function having following properties if we use linear shape functions:

$$N_i(x_i) = 1 \quad \text{and} \quad N_i(x_j) = 0, i \neq j \quad (2.13)$$

The test function can be written as:

$$v(x) = v_1 N_1(x) + v_2 N_2(x) + \dots + v_n N_n(x) \quad (2.14)$$

Consequently, we can get:

$$\text{Find } \mathbf{u} \in \mathbb{R}^n: u_i \int_{\Omega} \nabla N_j(x) \cdot \nabla N_i(x) dx = \int_{\Omega} v_i f dx, \quad i, j \in 1, 2, 3, \dots, n \quad (2.15)$$

We transform it to linear system:

$$\mathbf{A}\mathbf{u} = \mathbf{f} \quad (2.16)$$

Where:

$$A_{ij} = \int_{\Omega} \nabla N_j(x) \cdot \nabla N_i(x) dx \quad (2.17)$$

$$f_i = \int_{\Omega} v_i f dx \quad (2.18)$$

Through solving above linear system, we can get \mathbf{u} solution on the domain.

2.2 Multiscale Homogenization [9]

The multiscale homogenization combined with the concept of representative volume element (RVE) has achieved a high reputation for its convenience and accuracy on computing the behavior of composite material. RVE is regarded as a microscopic subregion representing the entire microscale structure from the average point of view. With the help of RVE, we are able to firstly solve the problems, like strain and stress, on microscale in the RVE model and then applying the results of RVE model to get the solutions on macroscale. The constitutive law on macroscale is not needed in multiscale homogenization analysis with RVE concept. The problem on microscale is boundary value problem (BVP) with particular boundary conditions.

Among the developed multiscale homogenization methods, the first-order homogenization method is one of the most popular choices. Following is the basic theory of first-order homogenization method.

2.2.1 General Background

In this work, we consider infinitesimal strains. We have two configurations, one is Ω_0 and another one is Ω_t . They are respectively the material (reference) configuration and spatial (current) configuration. And the connection between two configurations is the deformation map $\boldsymbol{\varphi}$:

$$\boldsymbol{\varphi}: \Omega_0 \rightarrow \Omega_t | \mathbf{x} = \boldsymbol{\varphi}(\mathbf{X}, t) \quad \mathbf{x} \in \Omega_0 \quad \text{and} \quad \mathbf{X} \in \Omega_t \quad (2.25)$$

And the tangent deformation map \mathbf{F} :

$$\mathbf{F}: \Omega_0 \rightarrow \Omega_t | d\mathbf{x} = \mathbf{F}(\mathbf{X}, t) \cdot d\mathbf{X} \quad (2.26)$$

$$\mathbf{F} = \text{grad}\boldsymbol{\varphi}(\mathbf{X}, t) = \frac{\partial \boldsymbol{\varphi}}{\partial \mathbf{X}} = \nabla_{\mathbf{X}} \quad (2.27)$$

However, above formulation is not satisfied anymore when we consider the finite material line in a finite volume. As a result, we need to use Taylor series expression for $\Delta \mathbf{x}$ in current configuration:

$$\Delta \mathbf{x} = \mathbf{F}(\mathbf{X}_0) \cdot \Delta \mathbf{X} + \frac{1}{2} \mathbf{G}(\mathbf{X}_0) : \Delta \mathbf{X} \otimes \Delta \mathbf{X} + \mathcal{O}(\Delta \mathbf{X}_0^3) \quad (2.28)$$

Where \mathbf{G} is the gradient of the deformation gradient tensor and \mathbf{G} is symmetric:

$$\mathbf{G} = \text{grad}\mathbf{F} = \nabla \mathbf{F} \quad (2.29)$$

2.2.2 First-order Homogenization

The domain Ω considered in this work is periodic, so the RVE model can represent its microstructure. Figure 2.1 shows the infinitesimal point \mathbf{X}_0 and its corresponding RVE around \mathbf{X}_0 that we have defined in the material configuration of the domain.

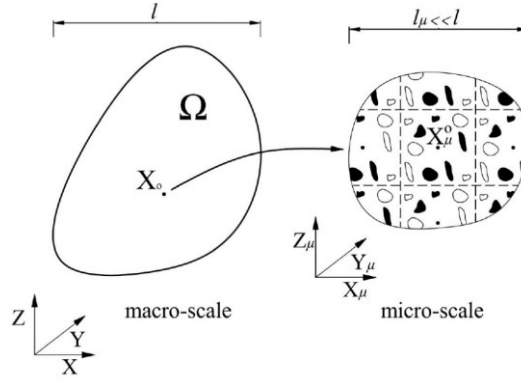


Figure 2.1. Macrostructure and microstructure around of the point X_0

Since the RVE is considered much smaller than the macroscale as discussed before, For the material point \mathbf{X}_μ^0 in the RVE we can apply the Taylor series to approximate its deformed position \mathbf{x}_μ^0 in spatial configuration:

$$\mathbf{x}_\mu(\mathbf{X}_0, \mathbf{X}_\mu) \cong \mathbf{x}_\mu^0 + \mathbf{F}(\mathbf{X}_0) \cdot \Delta \mathbf{X}_\mu + \mathbf{w}(\mathbf{X}_\mu) \quad (2.30)$$

$$\Delta \mathbf{X}_\mu = \mathbf{X}_\mu - \mathbf{X}_\mu^0, \quad \mathbf{X}_\mu \in \Omega_\mu \quad (2.31)$$

\mathbf{X}_μ^0 and \mathbf{x}_μ^0 are respectively the material and spatial coordinate system of the RVE, which equal to zero for simplification. \mathbf{X}_μ represents the original material point of \mathbf{x}_μ in material configuration.

By setting:

$$\mathbf{X}_\mu^0 = 0, \quad \mathbf{x}_\mu^0 = 0 \quad (2.32)$$

We get:

$$\mathbf{x}_\mu(\mathbf{X}_0, \mathbf{X}_\mu) \cong \mathbf{F}(\mathbf{X}_0) \cdot \mathbf{X}_\mu + \mathbf{w}(\mathbf{X}_\mu) \quad (2.33)$$

The displacement field \mathbf{u}_μ in RVE:

$$\mathbf{u}_\mu = \mathbf{x}_\mu - \mathbf{X}_\mu \quad (2.34)$$

Introducing the expression of \mathbf{x}_μ :

$$\mathbf{u}_\mu = [\mathbf{F}(\mathbf{X}_0) - \mathbf{I}] \cdot \mathbf{X}_\mu + \mathbf{w}(\mathbf{X}_\mu) \quad (2.35)$$

Where \mathbf{I} is the second order unit tensor.

From above displacement field, we can find that \mathbf{u}_μ is coupled by the macroscale ($\mathbf{F}(\mathbf{X}_0)$) and microscale (\mathbf{X}_μ). Through the average theories introduced by Hill [8], we can build following relationship between the gradient of deformation tensor on microscale \mathbf{F}_μ and the gradient of deformation tensor on macroscale \mathbf{F} :

$$\mathbf{F}(\mathbf{X}_0) = \frac{1}{V_\mu} \int_{\Omega_\mu} \mathbf{F}_\mu(\mathbf{X}_0, \mathbf{X}_\mu) dV \quad (2.36)$$

V_μ is the volume of the RVE in the material configuration.

We have:

$$\mathbf{F}_\mu(\mathbf{X}_0, \mathbf{X}_\mu) = \nabla \mathbf{x}_\mu(\mathbf{X}_0, \mathbf{X}_\mu) \cong \mathbf{F}(\mathbf{X}_0) + \nabla \mathbf{w}(\mathbf{X}_\mu) \quad (2.37)$$

\Rightarrow

$$\frac{1}{V_\mu} \int_{\Omega_\mu} \mathbf{F}_\mu(\mathbf{X}_0, \mathbf{X}_\mu) dV = \frac{1}{V_\mu} \int_{\Omega_\mu} \nabla \mathbf{x}_\mu(\mathbf{X}_0, \mathbf{X}_\mu) dV = \mathbf{F}(\mathbf{X}_0) + \frac{1}{V_\mu} \int_{\Omega_\mu} \nabla \mathbf{w}(\mathbf{X}_\mu) dV \quad (2.38)$$

\Rightarrow

$$\mathbf{F}(\mathbf{X}_0) = \frac{1}{V_\mu} \int_{\Omega_\mu} \nabla \mathbf{x}_\mu(\mathbf{X}_0, \mathbf{X}_\mu) dV - \frac{1}{V_\mu} \int_{\Omega_\mu} \nabla \mathbf{w}(\mathbf{X}_\mu) dV \quad (2.39)$$

By applying the divergence theorem, above formulation can be transformed to integration on the surface:

$$\mathbf{F}(\mathbf{X}_0) = \frac{1}{V_\mu} \int_{\partial\Omega_\mu} \mathbf{x}_\mu(\mathbf{X}_0, \mathbf{X}_\mu) \otimes \mathbf{N} dA - \frac{1}{V_\mu} \int_{\partial\Omega_\mu} \mathbf{w}(\mathbf{X}_\mu) \otimes \mathbf{N} dA \quad (2.40)$$

Where $\partial\Omega_\mu$ is the boundaries of RVE in the material configuration and \mathbf{N} is the outward unit normal on $\partial\Omega_\mu$.

As we can see, the average theory is satisfied only when following equations are true:

$$\frac{1}{V_\mu} \int_{\Omega_\mu} \nabla \mathbf{w}(\mathbf{X}_\mu) dV = 0 \quad \text{and} \quad \frac{1}{V_\mu} \int_{\partial\Omega_\mu} \mathbf{w}(\mathbf{X}_\mu) \otimes \mathbf{N} dA = 0 \quad (2.41)$$

Which gives the integration restriction on the RVE boundaries.

Next step is to get the microscopic and macroscopic strain tensor. Taking the infinitesimal deformation framework into account, the strain tensor in the microscale is:

$$\mathbf{E}_\mu(\mathbf{X}_0, \mathbf{X}_\mu) = \frac{1}{2} \left(\mathbf{F}_\mu(\mathbf{X}_0, \mathbf{X}_\mu) + \mathbf{F}_\mu^T(\mathbf{X}_0, \mathbf{X}_\mu) \right) - \mathbf{I} \quad (2.42)$$

\Rightarrow

$$\mathbf{E}_\mu(\mathbf{X}_0, \mathbf{X}_\mu) = \frac{1}{2} \left(\mathbf{F}(\mathbf{X}_0) + \mathbf{F}^T(\mathbf{X}_0) \right) - \mathbf{I} + \frac{1}{2} \left(\nabla \mathbf{w}(\mathbf{X}_\mu) + \nabla \mathbf{w}(\mathbf{X}_\mu)^T \right) \quad (2.43)$$

Applying the volume average theory to the microscopic strain tensor:

$$\mathbf{E}(\mathbf{X}_0) = \frac{1}{V_\mu} \int_{\Omega_\mu} \mathbf{E}_\mu(\mathbf{X}_0, \mathbf{X}_\mu) dV = \frac{1}{2} \left(\mathbf{F}(\mathbf{X}_0) + \mathbf{F}^T(\mathbf{X}_0) \right) - \mathbf{I} \quad (2.44)$$

\Rightarrow

$$\mathbf{E}_\mu(\mathbf{X}_0, \mathbf{X}_\mu) = \mathbf{E}(\mathbf{X}_0) + \frac{1}{2}(\nabla \mathbf{w}(\mathbf{X}_\mu) + \nabla \mathbf{w}(\mathbf{X}_\mu)^T) = \mathbf{E}(\mathbf{X}_0) + \mathbf{E}_\mu^\omega(\mathbf{X}_\mu) \quad (2.45)$$

$$\mathbf{E}_\mu^\omega(\mathbf{X}_\mu) = \frac{1}{2}(\nabla \mathbf{w}(\mathbf{X}_\mu) + \nabla \mathbf{w}(\mathbf{X}_\mu)^T) \quad (2.46)$$

The Hill-Mandel energy condition [10,11] has given the stress tensor relationship between microscale and macroscale. Its meaning is the virtual work of \mathbf{X}_0 must equal to the virtual work of RVE in volume average sense:

$$\mathbf{S} : \delta \mathbf{E}(\mathbf{X}_0) = \frac{1}{V_\mu} \int_{\Omega_\mu} \mathbf{S}_\mu : \delta \mathbf{E}_\mu dV \quad (2.47)$$

Where \mathbf{S} and \mathbf{S}_μ are respectively the macroscopic and microscopic stress tensors.

\Rightarrow

$$\mathbf{S} : \delta \mathbf{E}(\mathbf{X}_0) = \frac{1}{V_\mu} \int_{\Omega_\mu} \mathbf{S}_\mu : \delta \mathbf{E}(\mathbf{X}_0) dV + \frac{1}{V_\mu} \int_{\Omega_\mu} \mathbf{S}_\mu : \delta \mathbf{E}_\mu^\omega(\mathbf{X}_\mu) dV \quad (2.48)$$

Applying the volume average theory for \mathbf{S} and \mathbf{S}_μ in RVE:

$$\mathbf{S}(\mathbf{X}_0, \mathbf{X}_\mu) \equiv \frac{1}{V_\mu} \int_{\Omega_\mu} \mathbf{S}_\mu(\mathbf{X}_0, \mathbf{X}_\mu) dV \quad (2.49)$$

\Rightarrow

$$\int_{\Omega_\mu} \mathbf{S}_\mu : \delta \mathbf{E}_\mu^\omega(\mathbf{X}_\mu) dV = 0 \quad (2.50)$$

Which is the RVE variational equilibrium equation.

We define the RVE material constitutive tensor \mathbf{C}_μ , then we have:

$$\mathbf{S}_\mu(\mathbf{X}_0, \mathbf{X}_\mu) = \mathbf{C}_\mu(\mathbf{X}_\mu) : \mathbf{E}_\mu(\mathbf{X}_0, \mathbf{X}_\mu) = \mathbf{C}_\mu(\mathbf{X}_\mu) : \mathbf{E}(\mathbf{X}_0) + \mathbf{C}_\mu(\mathbf{X}_\mu) : \mathbf{E}_\mu^\omega(\mathbf{X}_\mu) \quad (2.51)$$

\Rightarrow

$$\mathbf{S}(\mathbf{X}_0, \mathbf{X}_\mu) = \frac{1}{V_\mu} \int_{\Omega_\mu} \mathbf{C}_\mu(\mathbf{X}_\mu) dV : \mathbf{E}(\mathbf{X}_0) + \frac{1}{V_\mu} \int_{\Omega_\mu} \mathbf{C}_\mu(\mathbf{X}_\mu) : \mathbf{E}_\mu^\omega(\mathbf{X}_\mu) dV \quad (2.52)$$

Above formulation shows that the stress tensor on macroscale not only depends on the macroscopic strain tensor $\mathbf{E}(\mathbf{X}_0)$, but also needs to consider the microscopic strain tensor $\mathbf{E}_\mu^\omega(\mathbf{X}_\mu)$ in the RVE.

2.2.3 FE^2 homogenization [12,13]

The multiscale analysis in PLCd code has introduced FE^2 homogenization into the FEM implementation. The FE^2 homogenization has following three steps:

- i) Initial analysis of the RVE to get the mechanical elastic behavior of the composite micro-model. This is characterized by the material stiffness tensor.
- ii) The local solutions in the unit cell, when it becomes non-linear, by the given overall strain. This rule is described in detail in reference [14]
- iii) After knowing the microscale stress, applying the homogenization rule to compute the macroscale stress.

Figure 2.2 and figure 2.3 have shown the procedures of multiscale analysis with the FE^2 homogenization.

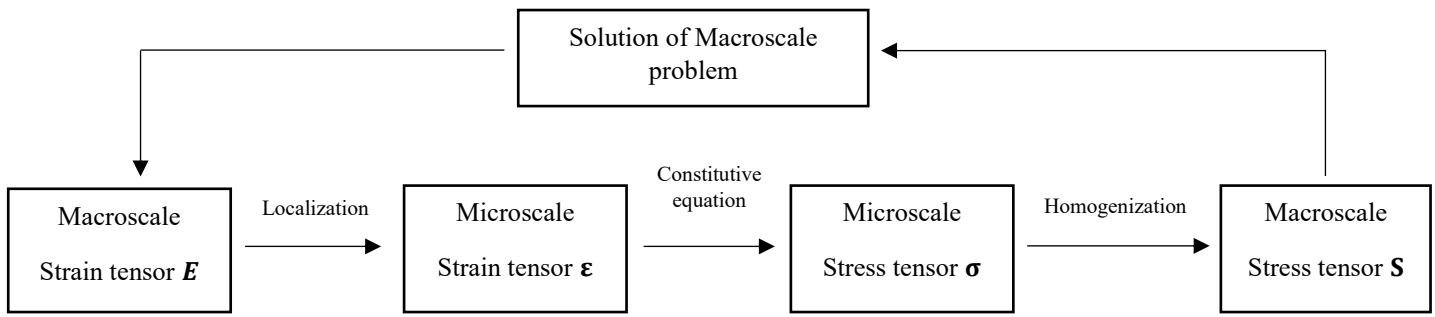


Figure 2.2. FE^2 homogenization

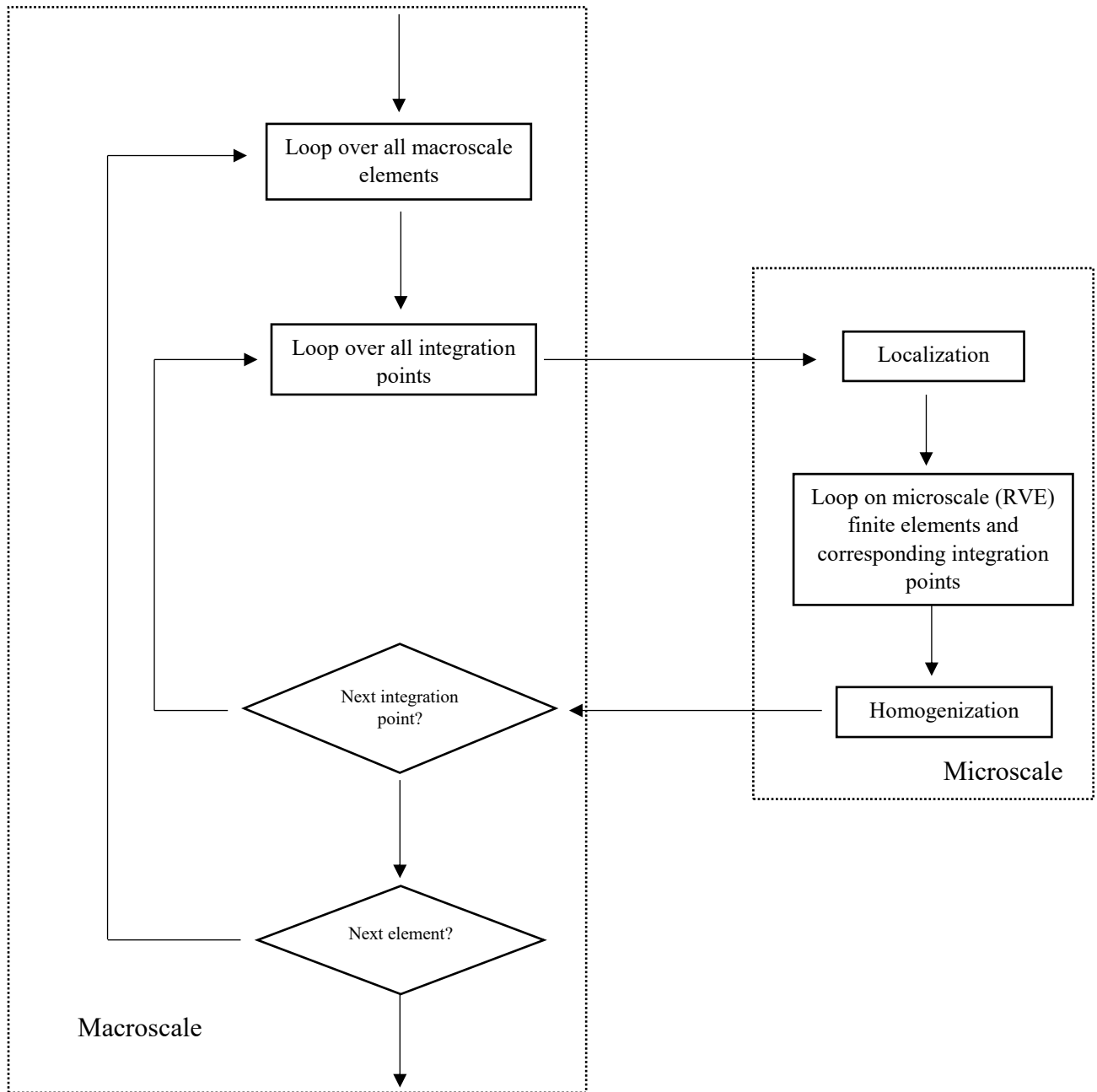


Figure 2.3. Problem solving procedure using FE^2 homogenization method

3 Analysis of the beam

In order to learn the PLCd code and validate its accuracy, the simulations of the beam have been conducted. The elements that have been implemented into the beam model in each case have different number and types. And two situations are considered in this part, one is the model considering isotropic material and another one is the model having used multiscale analysis procedure.

The main purpose of this part is to get myself used to conducting accurate numerical simulations through FEM and multiscale analysis.

3.1 Geometry and boundary conditions

3.1.1 Beam model and mesh

The model chosen for the validation procedure is the simple supported beam under two different load cases, including midspan centralized load or uniform load. The size of the beam is presented in table 3.1.

Size of the beam	Length(mm)	Width(mm)	Height(mm)
	10	0.5	0.5

Table 3.1. The size of the beam

The geometry and the boundary conditions of the beam are shown in figure 3.1.

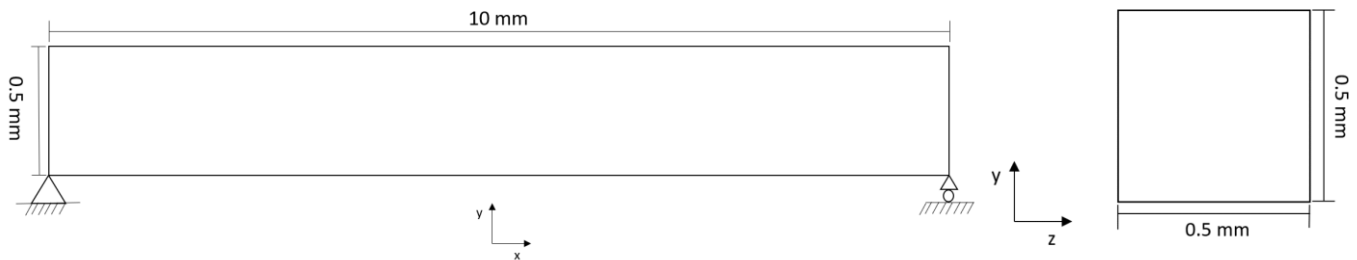


Figure 3.1. The geometry of the simple supported beam

The mesh of the beam model using 20000 elements has been shown in figure 3.2. For each load case, the quadratic and linear hexahedra elements are considered separately and different number of elements are implemented.

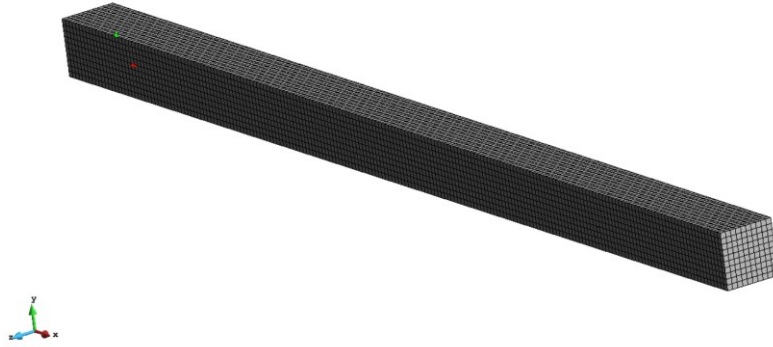


Figure 3.2. The mesh of the simple supported beam

3.2 Analysis considering an isotropic material

3.2.1 Material and basic settings

The Euler beam theory has been considered here since the ratio of length and height $\lambda = \frac{L}{H} = 20 > 10$. The total force applied in this part is 1 N. The material chosen for the model is steel, whose Young's Modulus is 206 MPa and Poisson Ratio is 0.30. And we don't consider the nonlinear behavior.

3.2.2 Midspan centralized load case

Because we have considered Euler beam theory, the analytical solution of the midspan tension stress on X direction of the beam under midspan centralized load should be:

$$\sigma_{mid-tension} = \frac{M_{mid}}{I} \cdot \frac{H}{2} = 120 \text{ MPa} \quad (3.1)$$

The numerical solutions are shown in figure 3.3 and we have used both linear and quadratic elements. Because of the existence of stress concentration phenomenon, the solutions of the stress field on some parts of the beam, like the area where the centralized load has been applied on, are much larger than the analytical values. Therefore, the tension stress on the midspan and bottom area of the beam is chosen to compare with the analytical solution to avoid the influence of stress concentration phenomenon. And following discussions in terms of the beam will follow this rule.

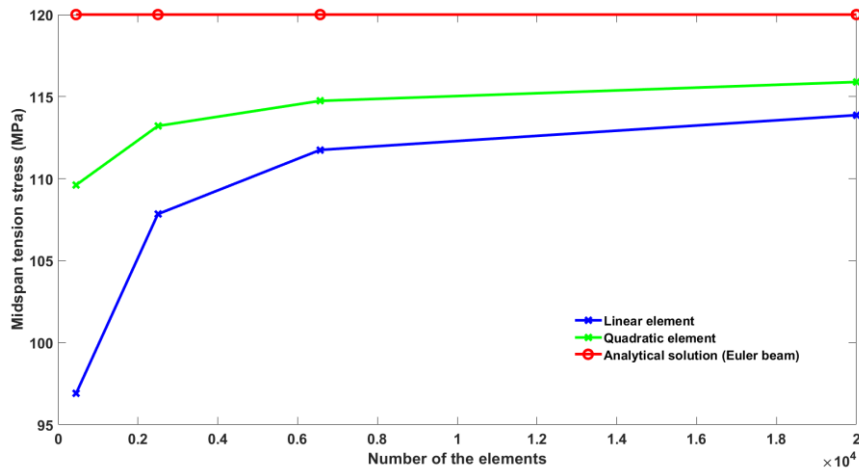


Figure 3.3. The stress solutions of simple supported beam under midspan centralized load

From figure 3.3 we can see that the solutions are convergent with the increasing elements. And the accuracy of applying quadratic element is higher compared to the linear element case using same number of elements.

Midspan load case		
Elements Number	Error (Linear, %)	Error (Quadratic, %)
450	19.25	8.66
2500	10.13	5.66
6566	6.88	4.38
20000	5.1	3.425

Table 3.2. The stress errors for midspan load case

The error results obtained in table 3.2 show that the solutions are convergent and the lowest error is 3.425%, which is acceptable.

In centralized load case, part of the error comes from the stress concentration phenomenon. Taking beam model using 20000 linear elements for instance, the concentration stress phenomenon appears on the middle area where the centralized load has been applied on.

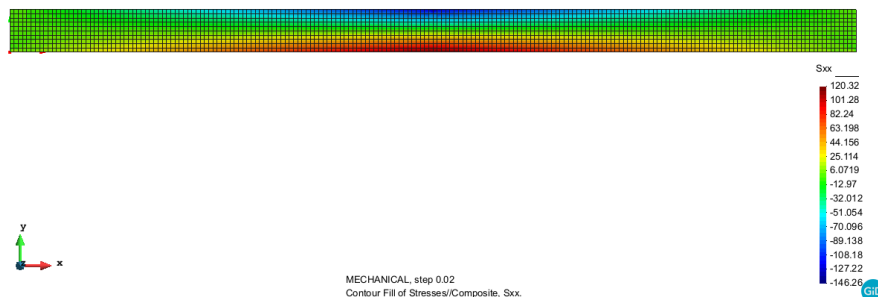


Figure 3.4. The stress solution of simple supported beam under midspan centralized load using 20000 elements (Linear element)

Analysis of the beam

In figure 3.4, the maximum compression stress happens on the midspan area, whose absolute value is 146.26 MPa. This is larger than the analytical result, which is supposed to be 120 MPa. We can see the stress concentration phenomenon in figure 3.5.

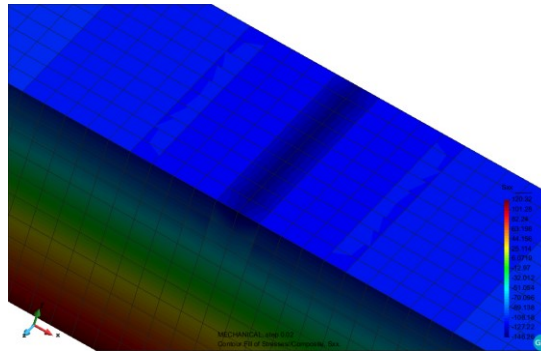


Figure 3.5. The stress concentration phenomenon happening on midspan area

3.2.3 Uniform load case

For uniform load case, the analytical solution of the midspan tension stress of simple supported beam under uniform load changes to:

$$M_{mid} = \frac{1}{8} \cdot ql^2 \quad (3.2)$$

$$\sigma_{mid-tension} = \frac{M_{mid}}{I} \cdot \frac{H}{2} = 60 \text{ MPa} \quad (3.3)$$

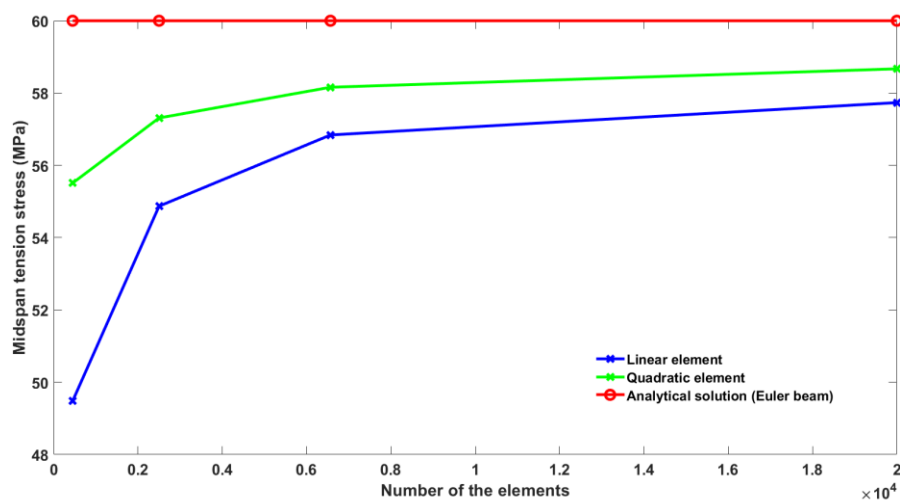


Figure 3.6. The stress solutions of simple supported beam under uniform load

Figure 3.6 presents the solutions obtained for both linear and quadratic elements. As we can see, both solutions are convergent.

Elements Number	Uniform load case	
	Error (Linear, %)	Error (Quadratic, %)
450	17.53	7.48
2500	8.55	4.48
6566	5.27	3.07
20000	3.78	2.21

Table 3.3. The stress errors for uniform load case

From table 3.3, it is possible to find that the accuracy has been improved. This is caused by the disappearance of the stress concentration phenomenon which has impacts on the stress distribution. Since the load is no longer centralized load, the lowest error becomes to 2.21% when we apply 20000 quadratic elements and this result proves that PLCd code is reliable.

Figure 3.7 shows the stress field on X direction of the beam using 20000 linear elements under uniform load. We can see that the maximum compression stress is becoming very close to the analytical solution, meaning the problem of stress concentration phenomenon has been improved under uniform load case.

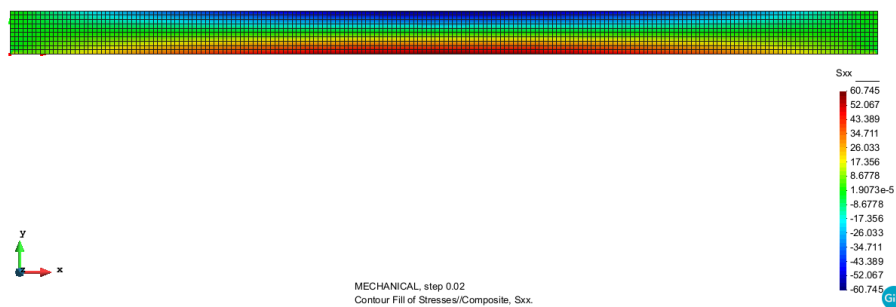


Figure 3.7. The stress solution of simple supported beam under uniform load using 20000 elements (Linear element)

3.3 Analysis with a multiscale procedure

3.3.1 Material, basic settings and RVE

In this part, the steel is still chosen as the material of the beam, whose Young’s Modulus is 206 MPa and Poisson Ratio is 0.30. In this case, the RVE is defined with only one material, steel, in order to get the results as exactly same as the results we have obtained with a macro-model in which the steel is used as an isotropic material in section 3.2. Nonlinear behavior is not considered. The RVE model and mesh for the beam are demonstrated in figure 3.8. The main purpose of this simulation is to help me be familiar with the numerical simulation using multiscale analysis procedure.

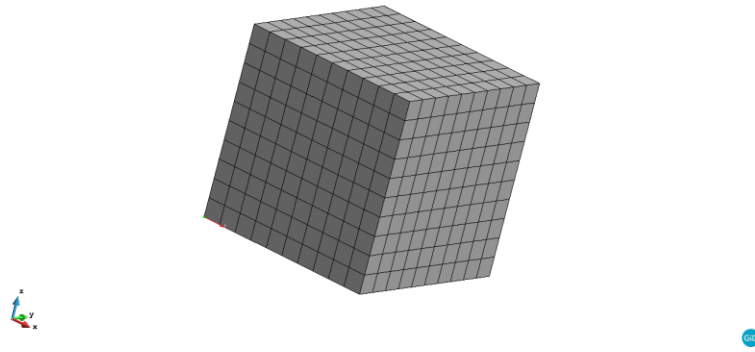


Figure 3.8. The geometry and mesh of the RVE model used for the beam

3.3.2 Midspan centralized load case

As we know from the contents in part 3.2.2, the analytical solution of the midspan tension stress on the X direction of the beam under centralized midspan load is 120 MPa. The solutions obtained from PLCd code by applying linear and quadratic elements are shown in Figure 3.9.

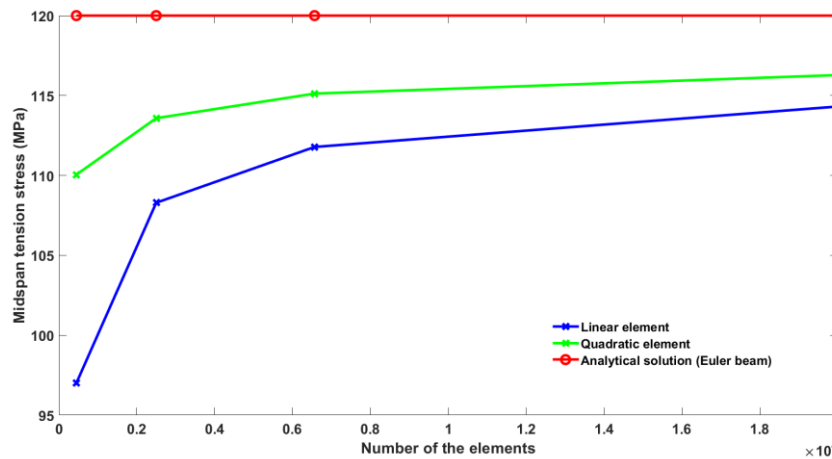


Figure 3.9. The stress solutions of simple supported beam under midspan centralized load by using multiscale analysis. From figure 3.9 we can find that solutions obtained by using linear and quadratic elements are both convergent. And the accuracy of the solution that has implemented the quadratic elements is higher than the solution using linear elements.

Midspan load case		
Elements Number	Error (Linear, %)	Error (Quadratic, %)
450	19.16	8.29
2500	9.76	5.35
6566	6.85	4.07
20000	4.74	3.10

Table 3.4. The stress errors for midspan load case by using multiscale analysis

Table 3.4 shows the errors of the stress solutions by using linear and quadratic elements. By increasing the number of the elements, the numerical solutions are approaching the analytical solution and the lowest error

Analysis of the beam

is 3.10%, which is lower than the corresponding error in part 3.2.2 whose value is 3.425%. The error results prove that the PLCd code based on multiscale analysis is also accurate.

Figure 3.10 gives the stress results on X direction of the beam under midspan load using 20000 quadratic elements. The maximum compression stress happening on the middle of the beam, supposed to have same absolute value as the tension stress, is -193.22 MPa and its absolute value is much larger than the theoretical value. This is caused by the stress concentration phenomenon under the midspan load.

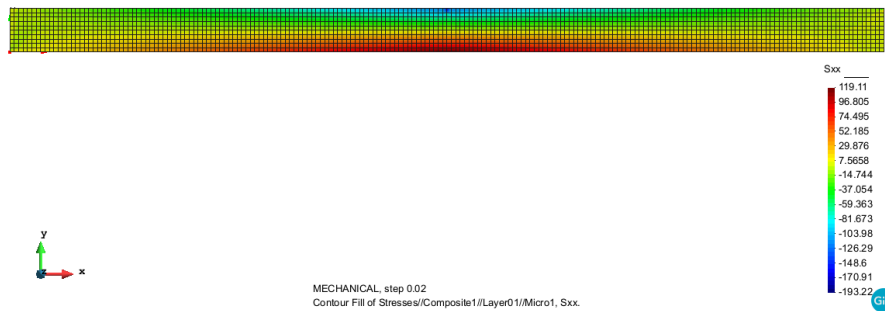


Figure 3.10. The stress solution of simple supported beam under midspan centralized load using 20000 elements by using multiscale analysis (Quadratic element)

Figure 3.11 shows the microscopic stress solutions on the midspan (Including upside and bottom faces on Y direction) area of the beam under midspan centralized load. The chosen elements are element 10000 (Left) and element 9991(Right), representing the upside midspan area and bottom midspan area respectively. The S_{xx} stress on the RVEs of element 10000 and element 9991 are -127.46 MPa and 97.578 MPa .

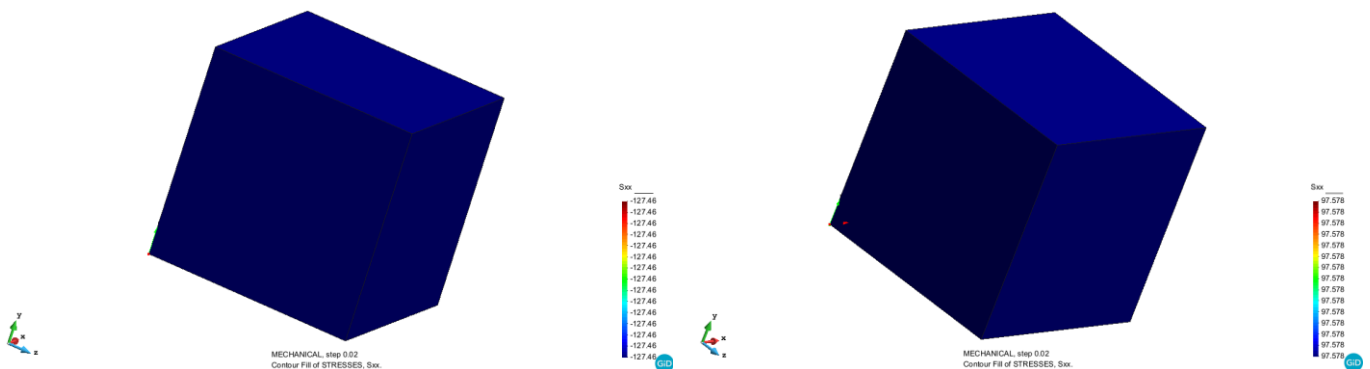


Figure 3.11. The stress solutions on microscopic scale on element 10000 (Left) and element 9991(Right) under centralized load by using multiscale analysis

3.3.3 Uniform load case

The maximum analytical solution of the tension stress of the beam should be 60 MPa under the uniform load

in our problem. Figure 3.12 shows the solutions of the midspan tension stress on X direction of the beam under uniform load using multiscale analysis of PLCd code.

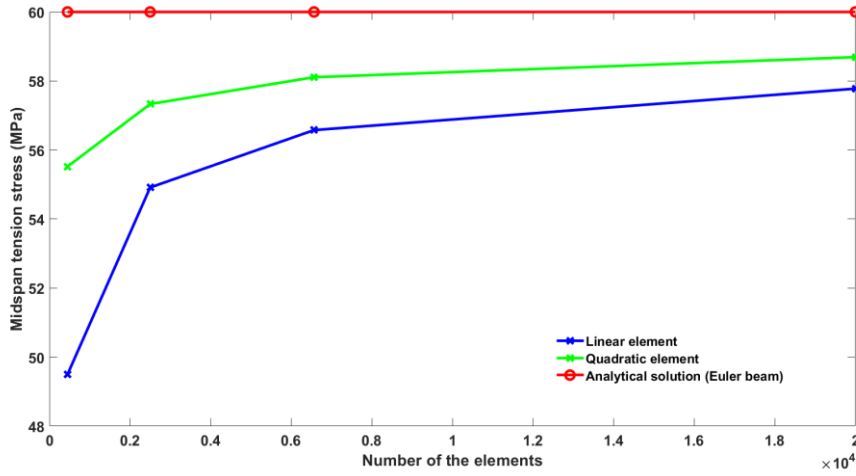


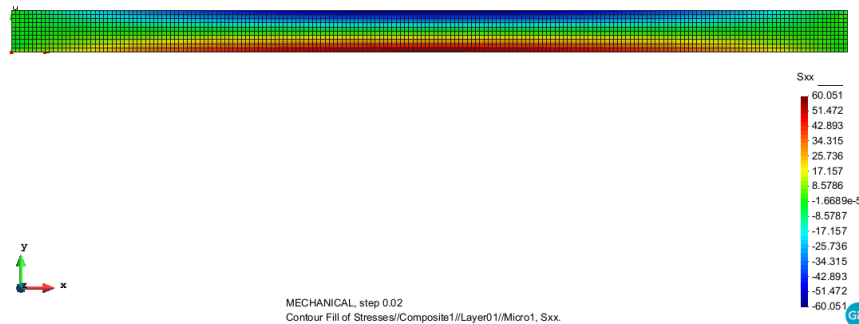
Figure 3.12. The stress solutions of simple supported beam under uniform load by using multiscale analysis

From figure 3.12 we can find that no matter what type of the elements are implemented, the solutions are both convergent. However, the accuracy of applying quadratic elements is higher comparatively.

Uniform load case		
Elements Number	Error (Linear, %)	Error (Quadratic, %)
450	17.5	7.47
2500	8.48	4.45
6566	5.71	3.15
20000	3.7	2.18

Table 3.5. The stress errors for uniform load case by using multiscale analysis

In table 3.5, we can also find the convergence of our solutions with the increasing number of elements. The lowest value of the errors in table 3.5 is 2.18 %, proving the high accuracy of multiscale analysis method in PLCd code. The tension stress field on X direction of the beam, using 20000 quadratic elements, is shown in figure 3.13.



Analysis of the beam

Figure 3.13. The stress solution of simple supported beam under uniform load using 20000 elements by using multiscale analysis (Quadratic element)

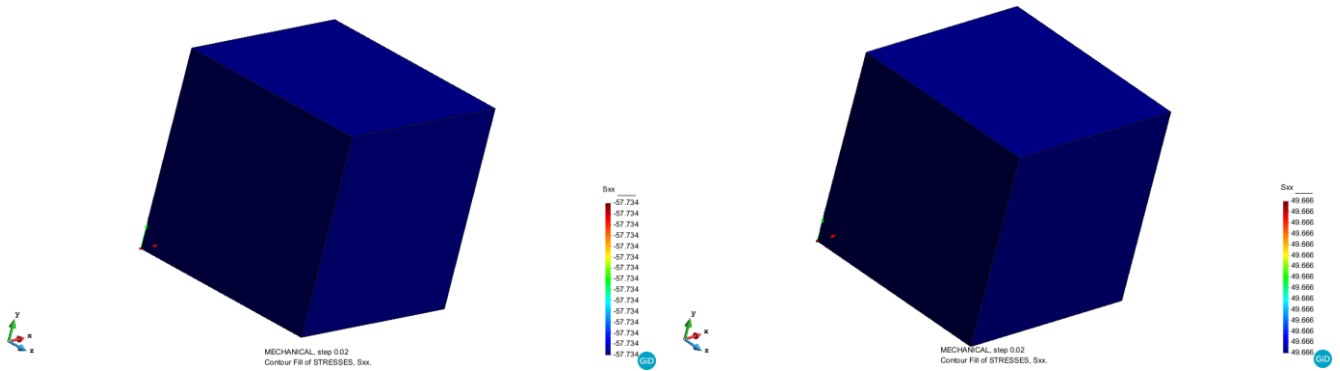


Figure 3.14. The stress solutions on microscopic scale on element 10000 (Left) and element 9991(Right) under uniform load by using multiscale analysis

Figure 3.14 shows the microscopic stress solutions on the midspan (Including upside and bottom faces on Y direction) area of the beam under uniform load. The upside midspan area and bottom midspan area are respectively represented by element 10000 and element 9991. The S_{xx} stress on the RVEs of element 10000 and element 9991 are -57.734 MPa and 49.666 MPa .

4 Analysis of the airplane interior cabin bin (Hatrack)

According to the numerical calculation request of ECO-COMPASS project, a cabin bin (Hatrack) manufactured with eco-composites should be analyzed. In order to achieve this aim, the simulation of the cabin bin considering isotropic materials is conducted first to study the performance of the structure and whether the boundary conditions are applied correctly. Then, the cabin bin with eco-composites is analyzed. The cabin bin's sandwich laminates made of eco-composites have ramie woven skins and an eco-honeycomb core. The materials of the skins and core are characterized with two RVEs respectively and the whole analysis is conducted with multiscale analysis procedure.

4.1 Geometry, boundary conditions and sandwich structure

4.1.1 Model, boundary conditions

Figure 4.1 presents the geometry of the cabin bin and its size is shown in table 4.1. We can also find the boundary conditions in figure 4.1.

Size of the cabin bin	Length(mm)	Width (Down, mm)	Width (Up, mm)	Height(mm)
bin	1032	592.8	356.2	250.8

Table 4.1. The size of the cabin bin

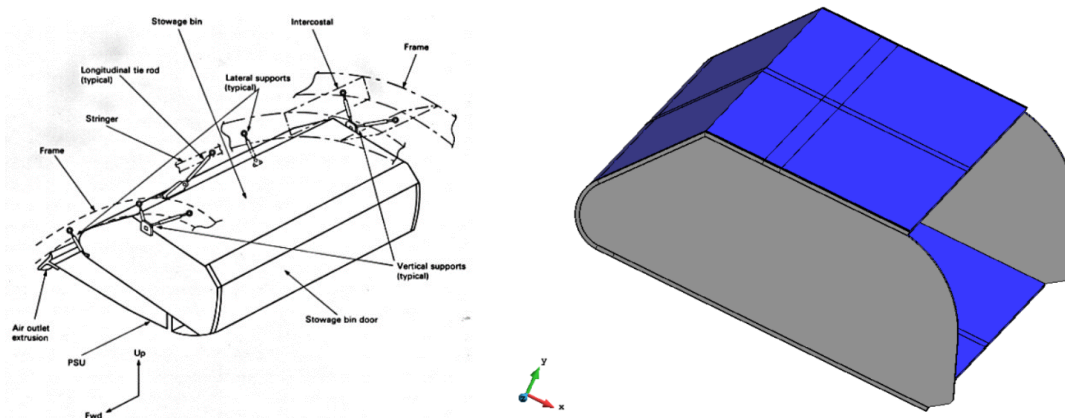


Figure 4.1. The geometry of the cabin bin and corresponding simplified model

The boundary conditions, drawn in blue and included in the circles, on the cabin bin model are shown in figure 4.2. They are line boundary condition type in PLCd and they are fixed on all directions according to the figure 4.1.

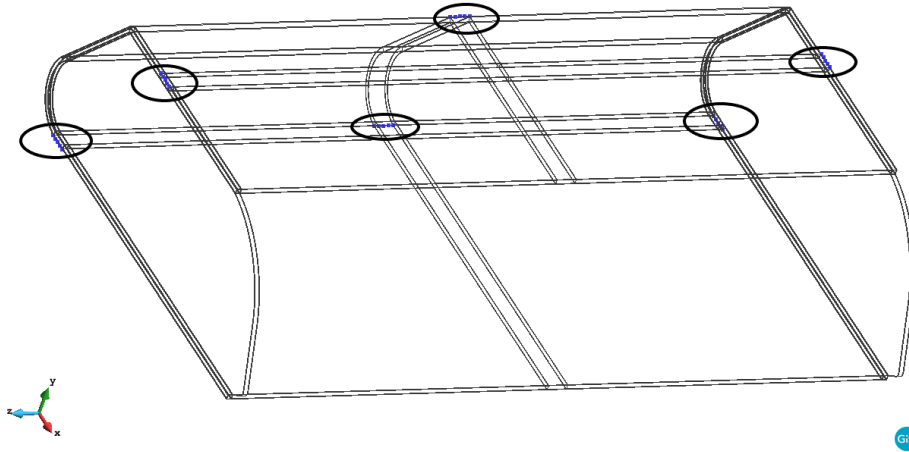


Figure 4.2. The boundary conditions on the cabin bin model (Drawn in blue color and included in the circles)

4.1.2 Mesh, basic settings

The geometry and corresponding mesh of the simplified model are shown in figure 4.3. We have implemented totally 77331 linear hexahedra elements for this model. Nonlinearity is not considered in our work. There are two load cases. The first one is that the area force exits on the hole bottom plate and its value is 0.9454 kN/m^2 , as we consider the total force on the cabin bin is 70 kg and the gravity coefficient is 0.8. Another load case is simulating the situation that only half of the plate is under area force and its value is still 0.9454 kN/m^2 .

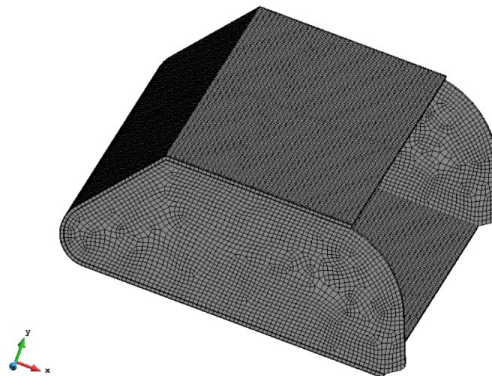


Figure 4.3. The mesh of the cabin bin model

4.1.3 Sandwich structure

The sandwich structure is applied for the cabin bin model and its structure is presented in figure 4.4. As we can see, the sandwich structure is composed by two components, skin and core, that have different mechanical properties. The outstanding properties of the skin component are high stiffness, reduced thickness and high

strength. Relatively, the core of the sandwich structure is made of material with much lighter weight and much lower stiffness. The typical example of the core is the honeycomb structure that will be implemented in the following part related to the multiscale analysis. However, for the honeycomb structure, since there are lots of empty spaces, the stresses on the core will be very large, which requires the material with high stiffness and high strength. The benefits making the sandwich structure attractive for aircraft industry are:

- i) They are much lighter.
- ii) They are highly stiff and strong.

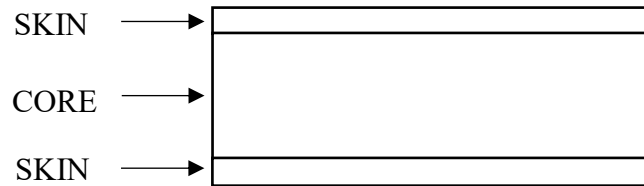


Figure 4.4. The sandwich structure

The size of the sandwich structure is shown in table 4.2.

Size of the sandwich structure	CORE (mm)	SKIN (mm)
	6	1

Table 4.2. The size of the sandwich structure

4.2 Analysis considering isotropic materials

4.2.1 Materials

The materials used for the cabin bin in this part are a quasi-isotropic glass fiber prepreg manufactured by Gurit: PF811-G231-32, and a foam made by BASF: Divinycell F50. The information about these two materials is shown in table 4.3. For the glass fiber, even though it is quasi-isotropic, it will be regarded as isotropic in this work to facilitate the simulations. The tension strength and compression strength of Divinycell F50 are 1.9 MPa and -0.6 MPa [15]. For the glass fiber PF811-G231-32, its strength under $21\text{ }^{\circ}\text{C}$ is 400 MPa [16].

Description	Material standard	Material	Manufacturer	Remark
CORE		Divinycell F50	BASF	Foam
SKIN	ABS5047-42	PF811-G231-32	Gurit	Glass fiber prepreg

Table 4.3. The information of the materials for the core and skin parts

Table 4.4 shows the material properties of the core and skin parts of the sandwich structure. The materials are considered as isotropic materials.

Material properties	Young's Modulus (MPa)	Poisson Ratio
CORE	40	0.32
SKIN	24000	0.27

Table 4.4. The material properties of the core and skin parts

4.2.2 Results of load case 1

In load case 1, the whole bottom plate is under area force whose value is 0.9454 kN/m^2 . In figure 4.5 we can see the load case 1.

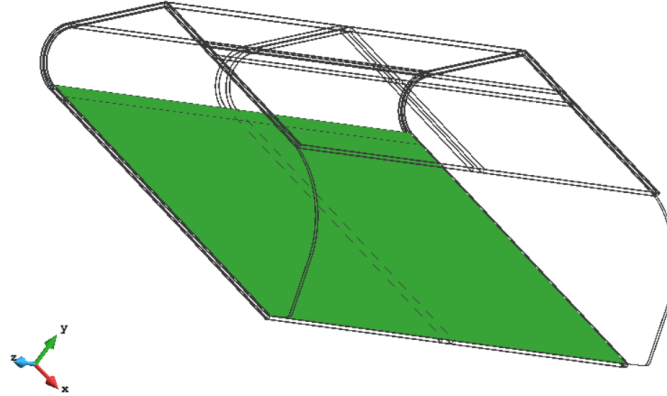


Figure 4.5. The load case 1

Displacement field

Figure 4.6 shows the displacement field of the cabin bin. The unit of the displacement field is mm . From this result, we can find that the displacements of the bottom plate are much larger compared to other parts' displacements. The maximum displacement happens on the middle of the front edge of the bottom plate, whose value is -7.2948 mm . Since the area force, boundary conditions and the structure are all symmetric, the displacement field is consequently symmetric.

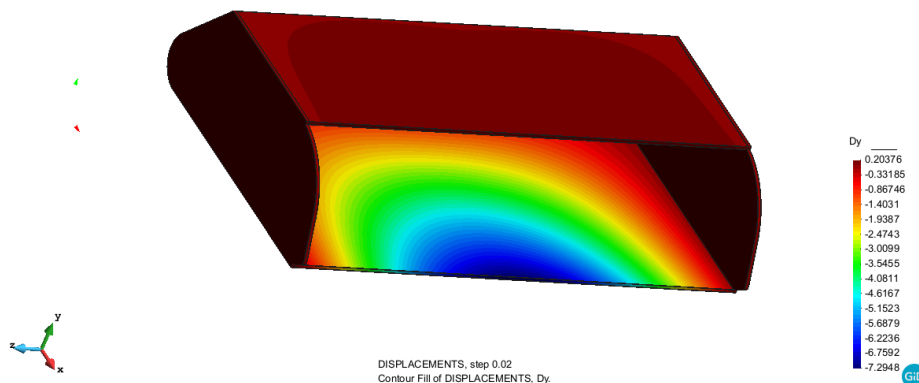


Figure 4.6. The displacement field of the cabin bin under load case 1

Principal Stress field

For the stress field on the cabin bin, the stress concentration phenomenon will be ignored in order to get the

accurate maximum stress and this procedure is conducted through the MIN and MAX functions in the postprocess of GiD, which can give us the real maximum and minimum values. The unit of the stress field is *MPa*.

i. Plate area

Skin

Figure 4.7 shows the S11 principal tension stress field on the plate. The stress field on the upside plate is uniform and small. However, on the bottom plate the stress field becomes much more complicated. For the inside skin of the bottom plate, the large stresses arise on the area near the boundary condition and two sides. The result is different for the outer skin of the bottom plate, since we can notice that the areas with large stresses are the complements of the inside skin's large stresses areas. On the area of the outer skin of the bottom plate where the boundary condition has been applied, the maximum S11 stress appears. On this area, we need to take more attention to avoid the fractures. The maximum S11 principal tension stress is 15.554 MPa .

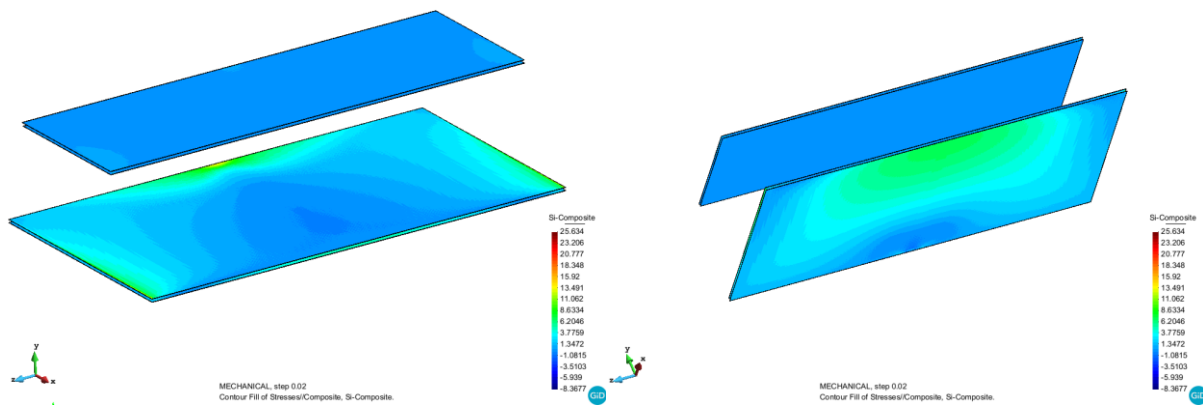


Figure 4.7. The S11 principal stress field on the skins of plates under load case 1

For the S33 principal compression stress, the result is presented in Figure 4.8. As we can see, on the upside plate and the inside skin of the bottom plate, the S33 stresses are very small. For the outer skin of the bottom plate, small S33 stresses are appearing on the most areas. However, around the area near the boundary condition, the S33 stresses become much larger. The maximum S33 stress is -41.822 MPa and its absolute value is also larger than the maximum S11 stress.

As we can see, the maximum S11 and S33 stresses on the skins of the plates are both lower than the stress threshold of the glass fiber, which is 400 MPa .

Analysis of the airplane interior cabin bin (Hatrack)

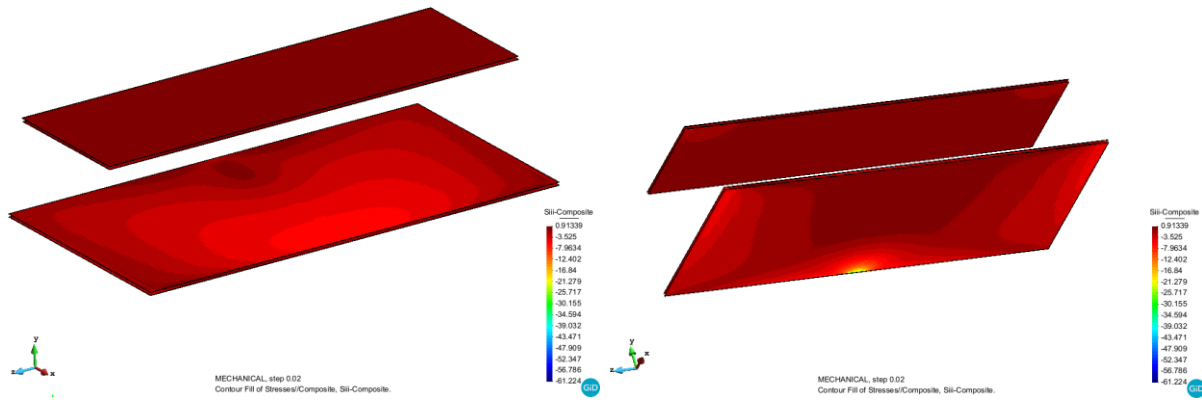


Figure 4.8. The S33 principal stress field on the skins of plates under load case 1

Core

The S11 principal tension stress field on the cores of the plates is shown in figure 4.9. As we can see, because of the special sandwich structure and the different mechanical properties applied on, the skin part has undertaken much larger stresses. As a result, the core of the structure can be made of much lighter materials with high stiffness, causing the reduction of weight and cost. Like the situation of the skins, on the upside core the S11 stresses are small. The areas with large S11 stresses include the area around the bottom boundary condition and the corners of the front side of the bottom core. The maximum S11 stress is $0.08534 MPa$. Another phenomenon is that the S11 stresses on the area where the bottom boundary condition has been applied are smallest, meaning the S33 stresses will be largest on this area.

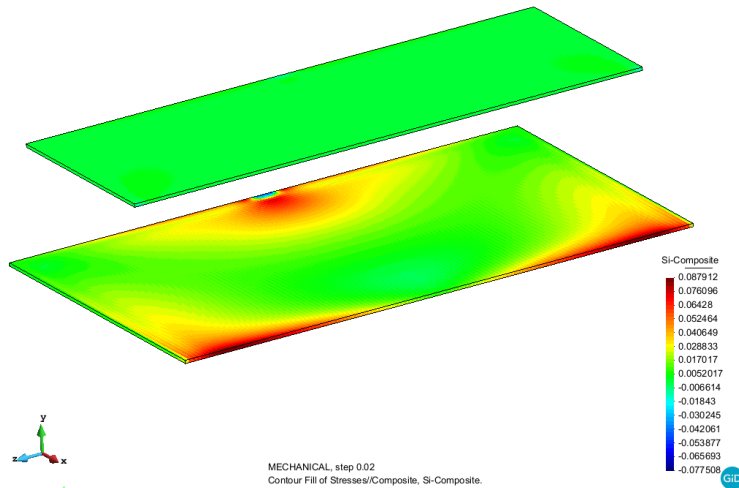


Figure 4.9. The S11 principal stress field on the cores of plates under load case 1

Figure 4.10 shows the S33 principal compression stress field on the cores of the plates. The S33 stresses are still very small on the upside core. The maximum S33 stress happens on the area where we apply the bottom boundary condition and its value is $-0.15684 MPa$.

As we can see, the maximum S11 and S33 stresses on the cores of the plates are both lower than the stress thresholds of the foam material, which are $1.9 MPa$ for the tension strength and $-0.6 MPa$ for the compression strength.

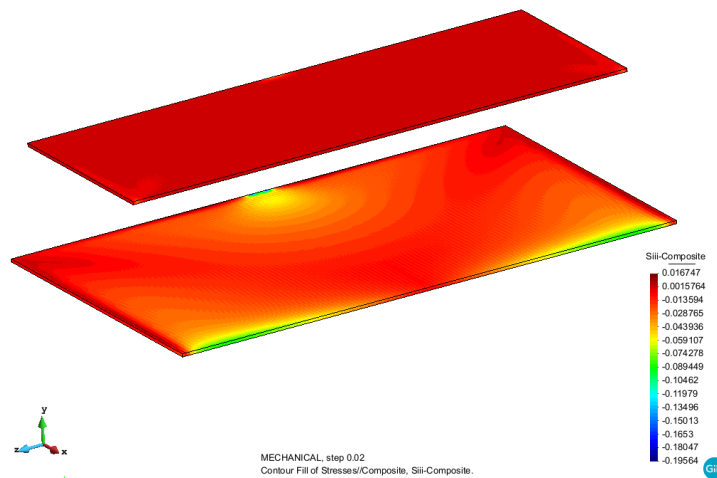


Figure 4.10. The S33 principal stress field on the cores of plates under load case 1

ii. Sides area

Skin

The S11 principal tension stress field on the skins of the sides is shown in figure 4.11. For the skins of the sides, its maximum S11 principal tension stress on the skins is 29.539 MPa , which is about doubling the maximum value on plates' skin. The areas where the stresses are large include the upside boundary condition areas on the sides part, the cross areas between the skins of sides and the skins of plates and the half of inside skins of sides.

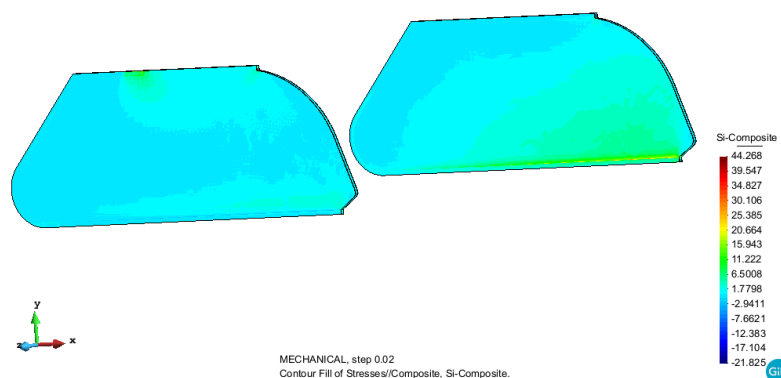


Figure 4.11. The S11 principal tension stress field on the skins of sides under load case 1

The areas where the large S11 principal tension stresses happen on are shown in figure 4.12. These areas need more attentions and strengthen measures to avoid damages on the structures.

Analysis of the airplane interior cabin bin (Hatrack)

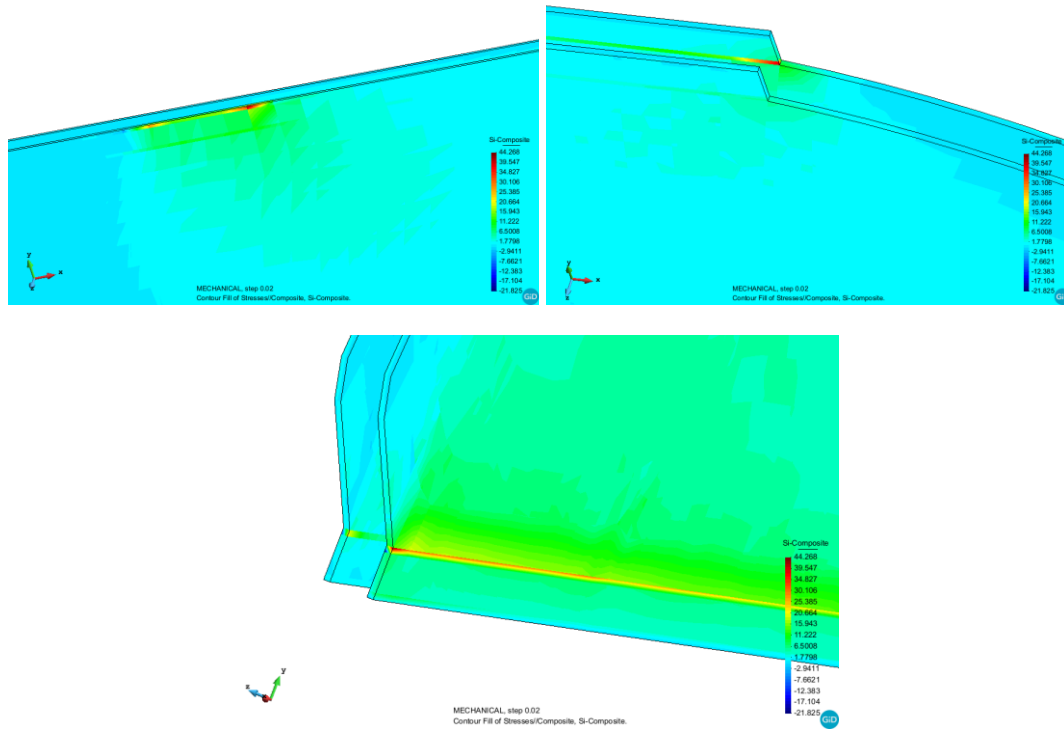


Figure 4.12. The large S11 principal tension stresses on the skins of sides under load case 1

Figure 4.13 shows the S33 principal compression stress field on the skins of the sides of the cabin bin. The maximum value is -51.369 MPa and its absolute value is larger than the maximum S11 principal tension stress. Most areas of the sides are under small compression stresses, except some areas like the cross area between the skins of plates and sides.

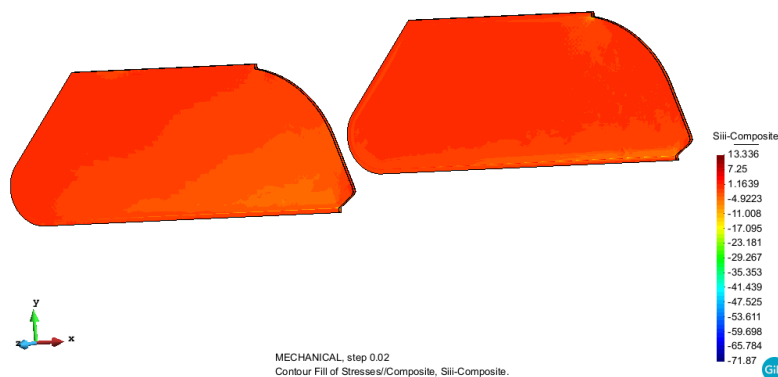


Figure 4.13. The S33 principal compression stress field on the skins of sides under load case 1

Figure 4.14 shows the cross areas between the upside skin of the bottom plate and the skins of two sides, where the S33 stresses are large.

As we can see, the maximum S11 and S33 stresses on the skins of the sides are both lower than the stress threshold of the glass fiber, which is 400 MPa .

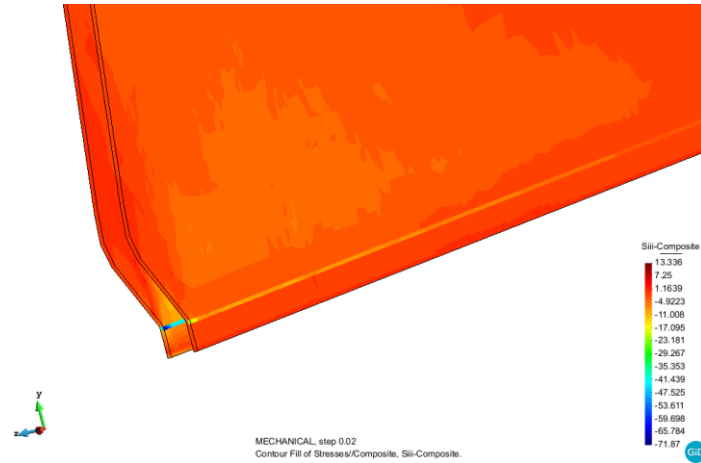


Figure 4.14. The large S33 principal compression stresses on the skins of sides under load case 1

Core

The S11 principal tension stress field on the cores of the sides is shown in figure 4.15. It can be seen that large S11 stresses happen on the areas near the cross areas between the cores of sides and bottom plate and these areas are drawn in red color. The maximum S11 stress is 0.15557 MPa . On other areas, the stresses are small.

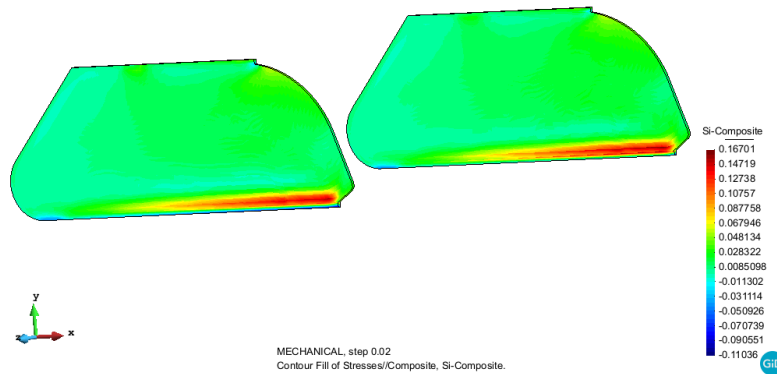


Figure 4.15. The S11 principal compression stress field on the cores of sides under load case 1

Figure 4.16 has shown the S33 principal compression stress field on the cores of the sides. From figure 3.1 we can find that the S33 stresses are very small on the most areas of the cores. The large S33 stresses are showing on the cross area between the cores of the sides and the bottom plate. The maximum S33 stress can be found on the bottom faces of the cores. The maximum S33 stress is -0.45437 MPa .

As we can see, the maximum S11 and S33 stresses on the cores of the sides are both lower than the stress thresholds of the foam material, which are 1.9 MPa for the tension strength and -0.6 MPa for the compression strength.

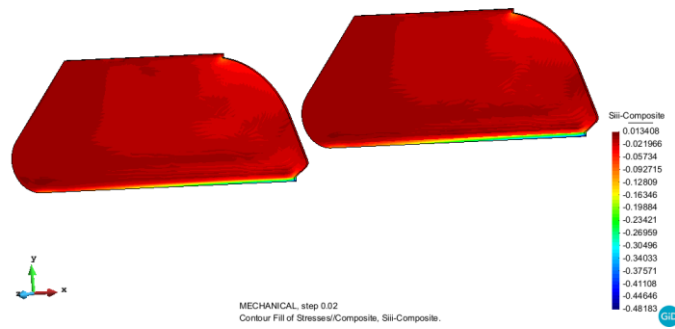


Figure 4.16. The S33 principal compression stress field on the cores of sides under load case 1

The large S33 principal compression stresses on the cores of sides is shown in figure 4.17.

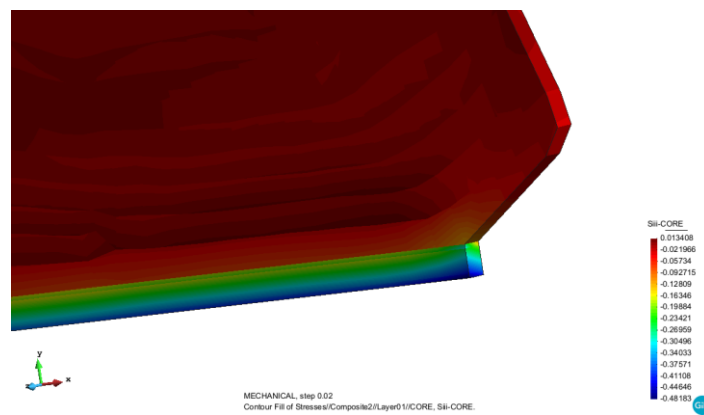


Figure 4.17. The large S33 principal compression stresses on the cores of sides under load case 1

iii. Back area

Skin

Figure 4.18 shows the S11 principal tension stress field on the skins of back part when we apply the load case 1. As we can see, the S11 stresses are large on the areas near the bottom boundary condition area where the maximum S11 stress is arising on. On other areas of the back part, the stresses have much smaller values.

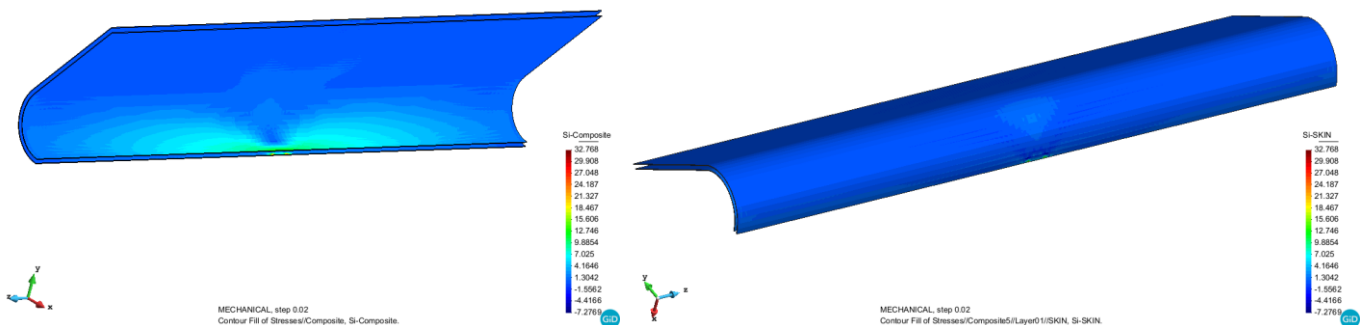


Figure 4.18. The S11 principal tension stress field on the skins of back part under load case 1

Figure 4.19 shows that where the large S11 principal tension stresses have occurred and the maximum value is 19.905 MPa.

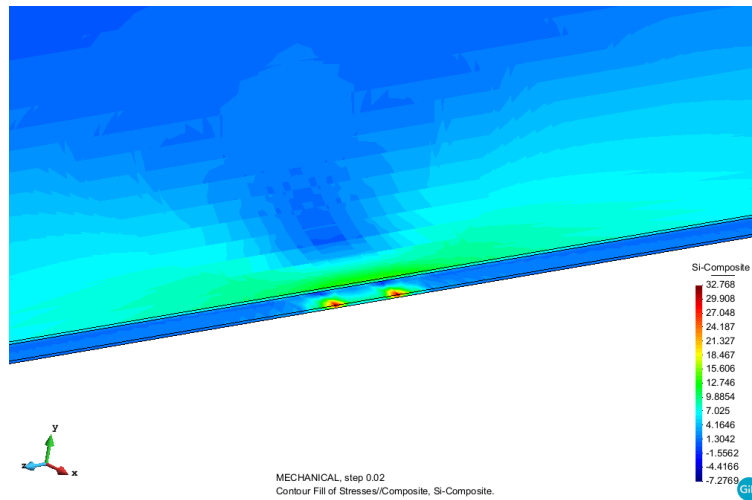


Figure 4.19. The large S11 principal tension stresses on the skins of back part under load case 1

In figure 4.20 we can see the S33 principal compression stress field on the skins of the back part. Like the situation of the S11 stress field, on the most areas of the back part, the stresses are small. However, because of the boundary condition that we have applied, the S11 stresses near the bottom boundary condition are much larger and this area is where we should be care of.

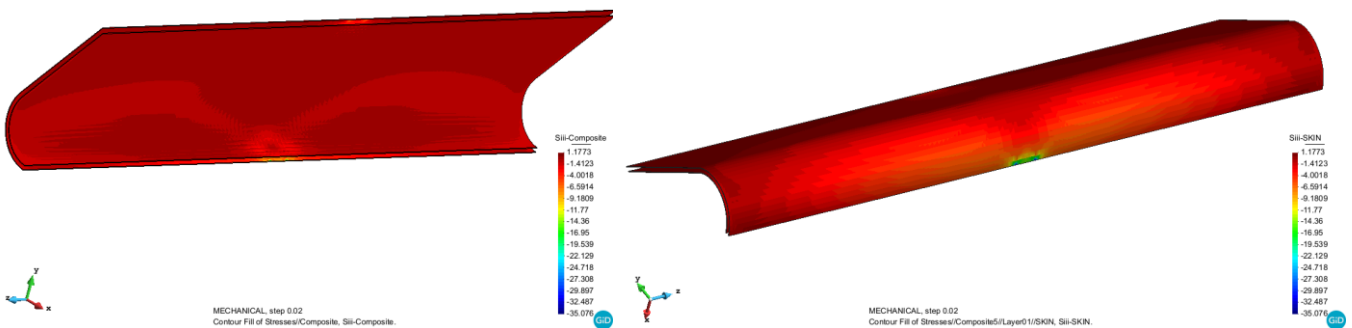


Figure 4.20. The S33 principal compression stress field on the skins of back part under load case 1

On the bottom boundary condition area of the outer skin, we can find the maximum S33 stress. The maximum value is -25.016 MPa and it is also the area where the maximum S11 stress happens. Figure 4.21 shows the bottom boundary condition area on the skins of the back part where the S33 stresses are large.

As we can see, the maximum S11 and S33 stresses on the skins of back part are both lower than the stress threshold of the glass fiber, which is 400 MPa .

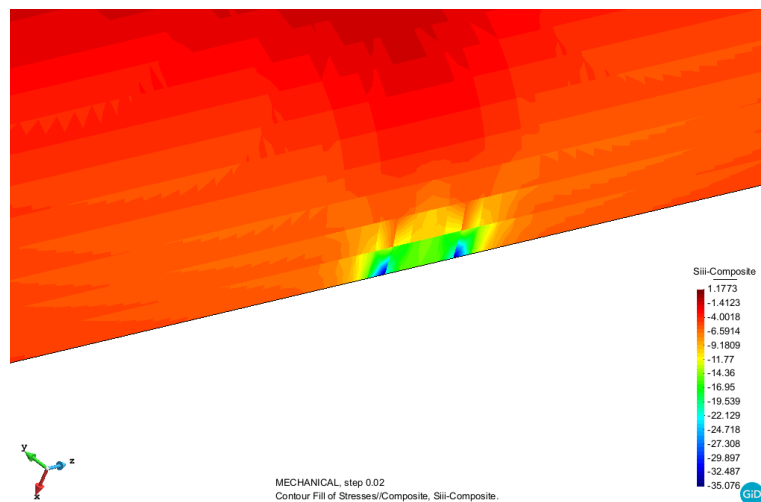


Figure 4.21. The large S33 principal compression stresses on the skins of back part under load case 1

Core

The S11 principal tension stress field on the core of the back part is shown in figure 4.22. On the bottom boundary condition area, the values of the S11 stresses are negative. However, the S11 stresses are large on the areas around the boundary condition area and the maximum S11 stress is 0.14193 MPa . On other areas of the core, the S11 stresses are small.

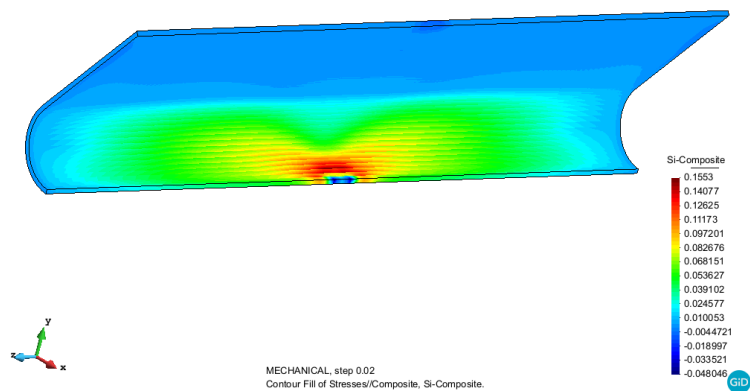


Figure 4.22. The S11 principal tension stress field on the cores of back part under load case 1

The S33 principal compression stress field on the core of the back part is shown in figure 4.23. From this figure we can see that except the bottom boundary condition area, the S33 stresses are very small on the most areas of the core. The large S33 stresses appear on the bottom boundary condition area and its maximum value is -0.16354 MPa .

As we can see, the maximum S11 and S33 stresses on the cores of the back part are both lower than the stress thresholds of the foam material, which are 1.9 MPa for the tension strength and -0.6 MPa for the compression strength.

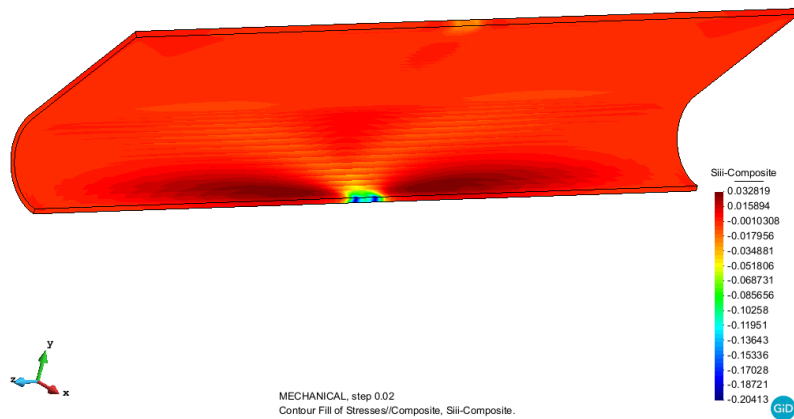


Figure 4.23. The S33 principal compression stress field on the cores of back part under load case 1

Bending stress field

For the bending stress field, the discussions will only focus on the bottom plate, which has undertaken the bending force mostly. The directions of the bending stresses S_{xx} and S_{zz} are shown in the left part of figure 4.24.

Skin

The S_{xx} bending stress field on the skins of the plates is shown in figure 4.24. As we can see, the stresses on the skins of the upside plate are small. On the inside skin of the bottom plate, the tension stresses are large on the area near the bottom boundary condition, drawn in dark red. For the outer skin of the bottom plate, on the area around the bottom boundary condition, we can find large compression stresses. The maximum tension stress is $6.6227 MPa$ and the maximum compression stress is $-24.285 MPa$.

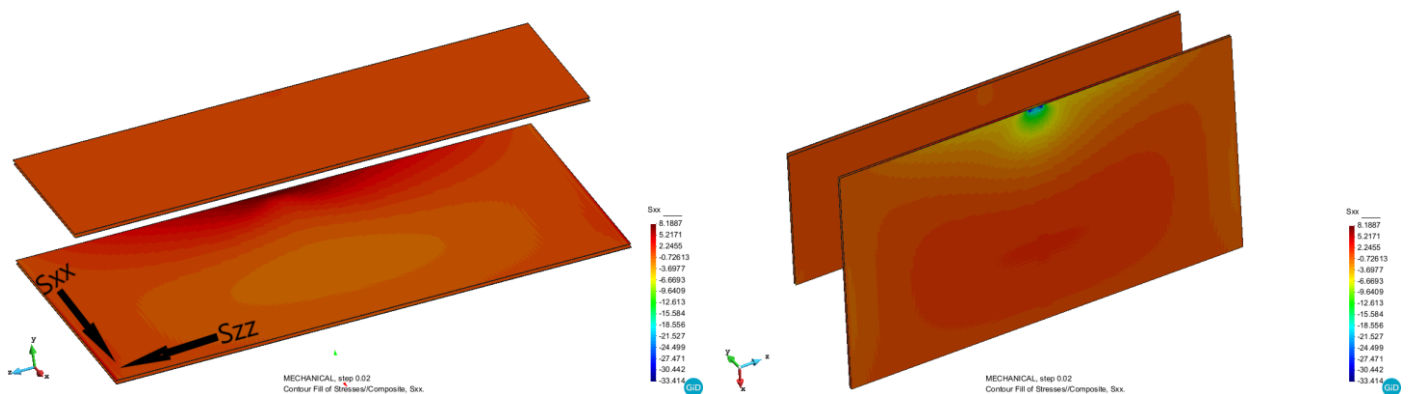


Figure 4.24. The S_{xx} bending stress field on the skins of plates under load case 1

Figure 4.25 shows the tension and compression distribution of the S_{xx} stress field on the skins of the plates. The areas without showing the stresses are under tension stresses while other areas are representing the

Analysis of the airplane interior cabin bin (Hatrack)

compression stresses areas.

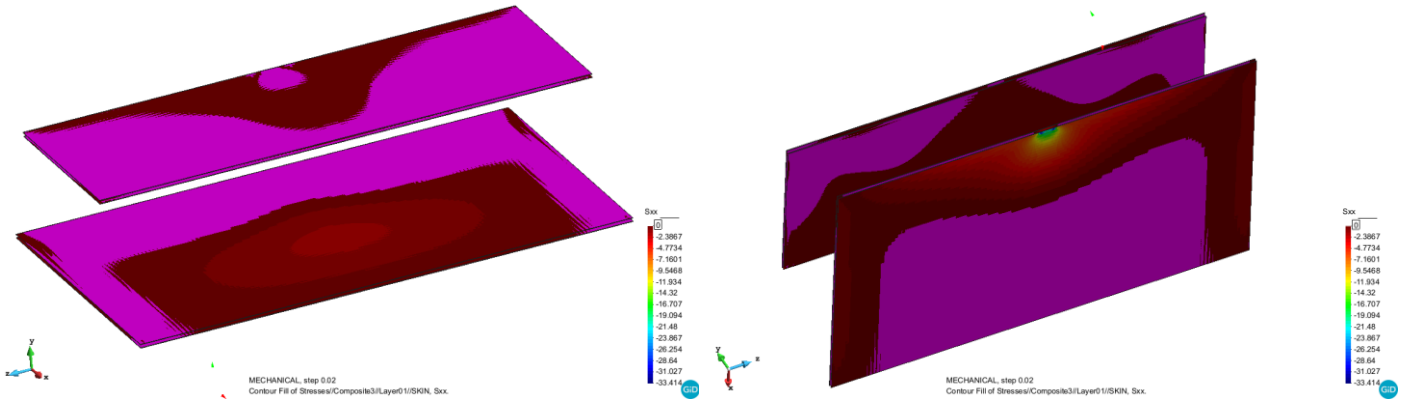


Figure 4.25. The tension and compression stresses’ distribution of Sxx stresses on the skins of plates

The Szz bending stress field on the skins of the plates is shown in figure 4.26. Like the situation of the Sxx bending stress field, on the skins of the upside plate, the Szz bending stresses are small. On the inside skin of the bottom plate, the areas where the tension stresses are large are the area near the bottom boundary condition and the two front corners. The compression stresses are large on the middle and front area of the inside skin. For the outer skin of the bottom plate, the Szz stress field is the complementation of the stress field of inside skin. The area having large compression stresses, the bottom boundary condition area and the two front corners, are the area where the tension stresses are large on the inside skin. The maximum Szz tension stress appears on the right corner of the inside skin and its value is 6.8125 MPa . The maximum Szz compression stress can be found on the bottom boundary condition area and its value is -17.306 MPa .

The tension and compression stresses’ distribution of Szz stresses is shown in figure 4.27. The tension stresses have been represented by the areas without showing the stresses.

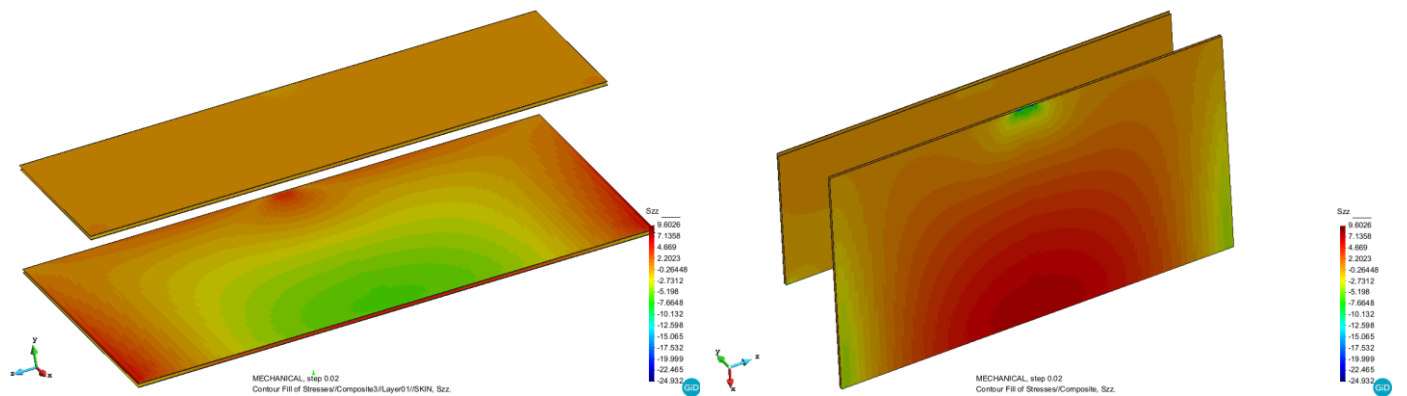


Figure 4.26. The Szz bending stress field on the skins of plates under load case 1

Analysis of the airplane interior cabin bin (Hatrack)

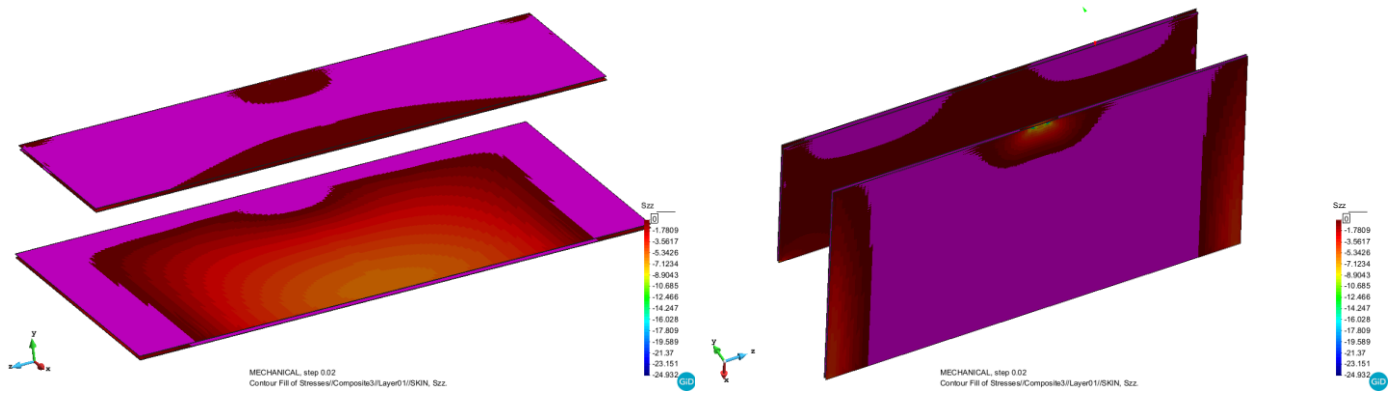


Figure 4.27. The tension and compression stresses' distribution of Szz stresses on the skins of plates

Core

The Sxx bending stress field on the cores of the plates is shown in figure 4.28. As we can see, the stress distribution on the cores are similar to the stress distribution on the skins. Near the bottom boundary condition area, the tension stresses are large. The bottom boundary condition area itself has large compression stresses. On the two sides of the core of the bottom plate, the tension stresses are large. The maximum tension and maximum compression stresses are both happening on the bottom boundary condition area and their values are 0.029449 MPa and -0.084093 MPa , which are very small compared the stresses on the skins.

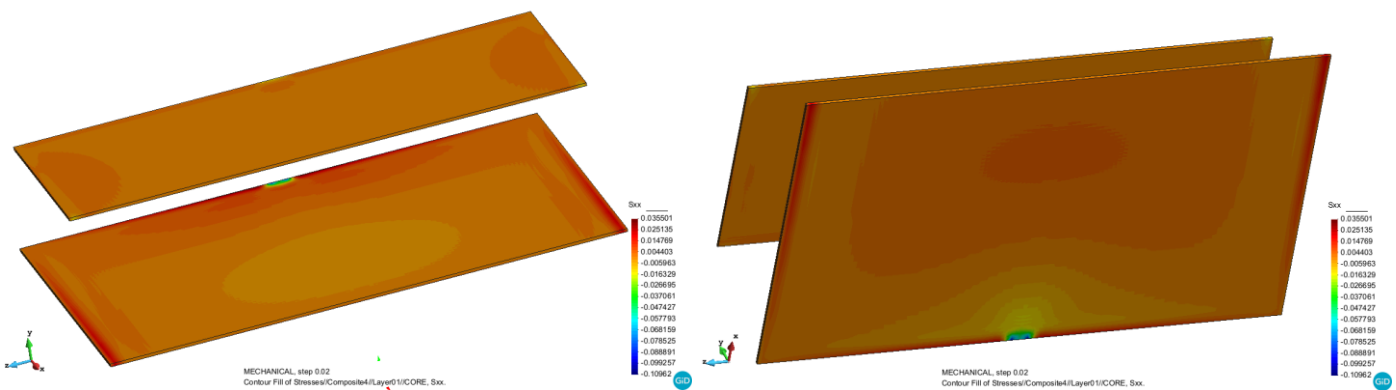


Figure 4.28. The Sxx bending stress field on the cores of plates under load case 1

Figure 4.29 has shown the tension and compression stresses' distribution of the Sxx stresses on the cores.

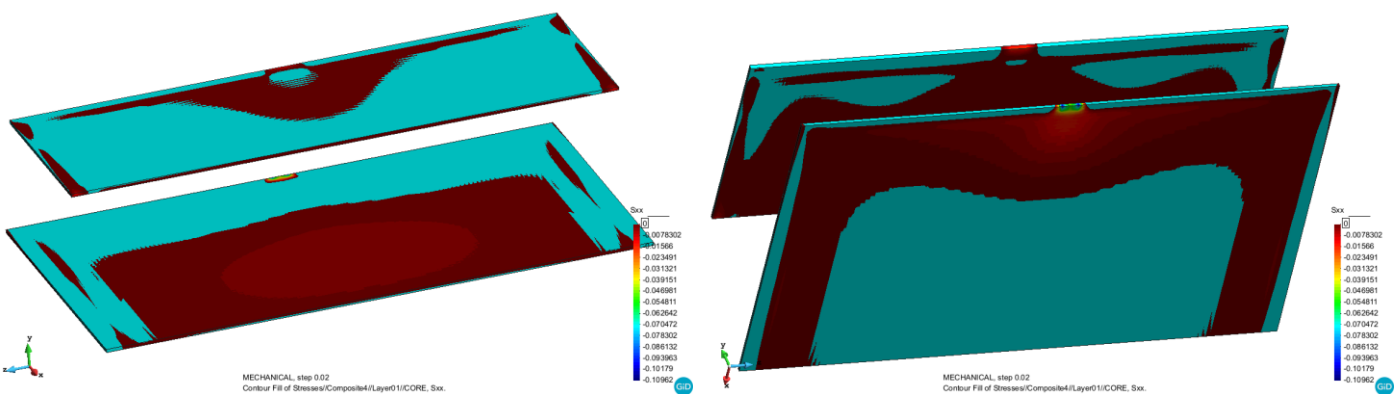


Figure 4.29. The tension and compression stresses' distribution of Sxx stresses on the cores of plates

From figure 4.30 we can find that the distribution of the Szz stresses is similar to the situation of the Sxx stress

Analysis of the airplane interior cabin bin (Hatrack)

field. The bottom boundary condition area has large compression stresses while the tension stresses are also large near this area. On the two sides of the bottom, the large tension stresses can be found. The maximum tension and maximum compression stresses are both appearing on the bottom condition area. The maximum tension stress is 0.025938 MPa and the maximum compression stress is -0.081009 MPa . They are also very small.

The tension and compression stresses' distribution of the S_{zz} stresses is shown in figure 4.31.

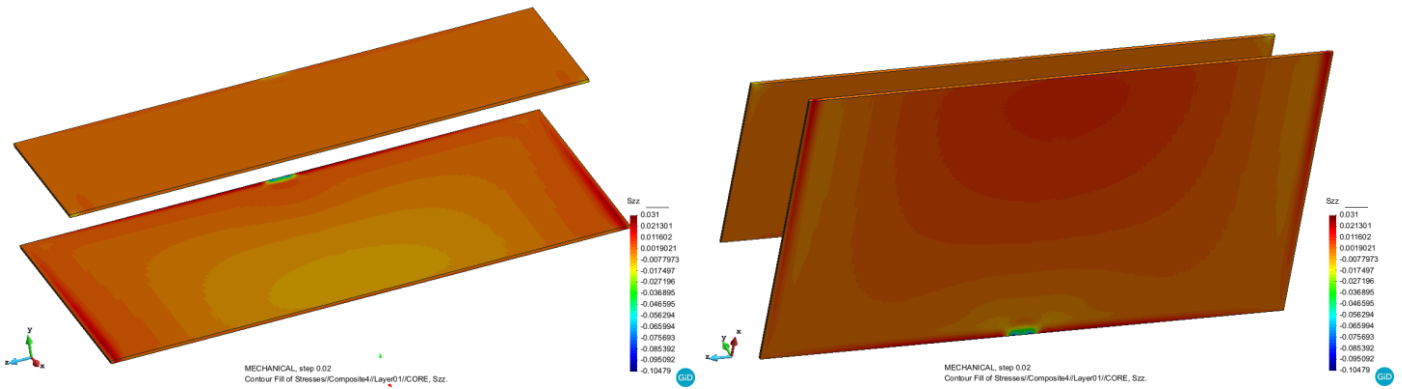


Figure 4.30. The S_{zz} bending stress field on the cores of plates under load case 1

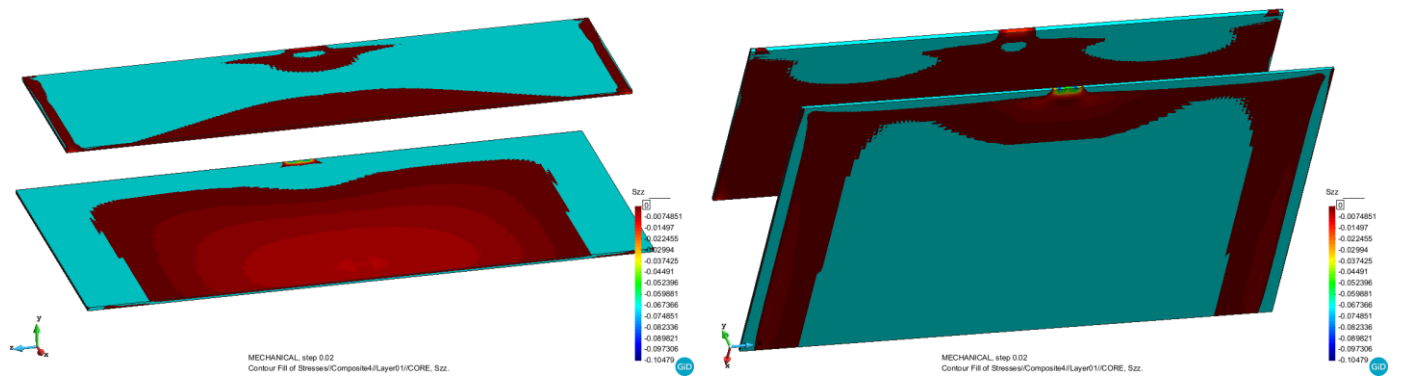


Figure 4.31. The tension and compression stresses' distribution of S_{zz} stresses on the cores of plates

4.2.3 Results of load case 2

The difference between two load cases is that the area force is applied only on half of the bottom plate in load case 2. And its value is still 0.9454 kN/m^2 and we can see this load case in figure 4.32. The load case 2 might be a critical situation for the structure since a torque force will be applied on the structure.

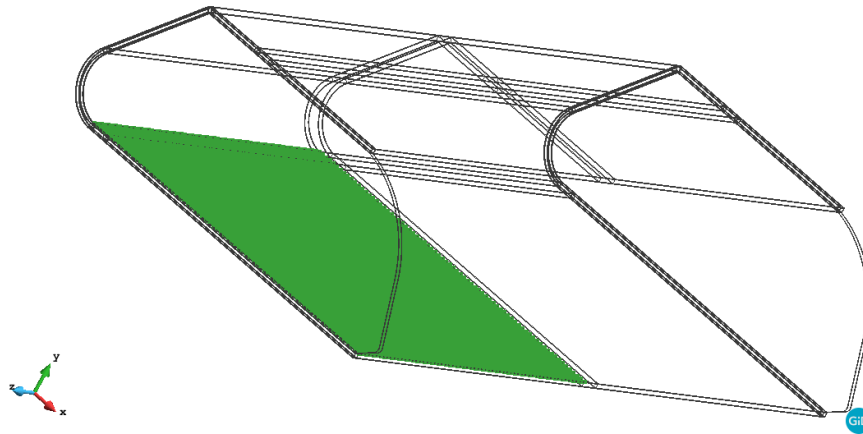


Figure 4.32. The load case 2

Displacement field

The displacement field of the cabin bin under load case 2 is shown in figure 4.33. In load case 1, the displacement field of the cabin bin is symmetric. However, in load case 2, since the area force is no longer symmetric, the displacement field on left half part of the structure becomes larger than the right half part. And its maximum displacement is -3.5022 mm now, which is about half of the maximum displacement value in load case 1. The maximum displacement still happens on the front edge of the bottom plate but it moves left compared to load case 1.

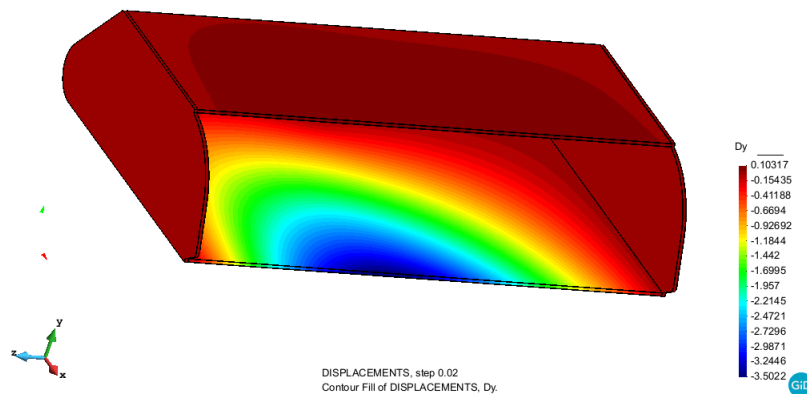


Figure 4.33. The displacement field of cabin bin under load case 2

Principal Stress field

The stress concentration will be also ignored in this part.

i. Plate area

Skin

Figure 4.34 shows the S11 principal tension stress field on the skins of the plates under load case 2. Similar to the situation of displacement field, the stress field becomes nonsymmetric and its values on the left part of the plates are larger. The areas where the S11 stresses are large are on the skins of the bottom plate. As figure has shown, these areas are the left side of the inside skin, the area near the bottom boundary condition on the inside skin and left part of the outer skin. On the skins of the upside plate, the S11 stresses are small like the situation of load case 1. However, the maximum S11 principal tension stress in load case 2 is 8.4327 MPa and this is smaller than its value in load case 1.

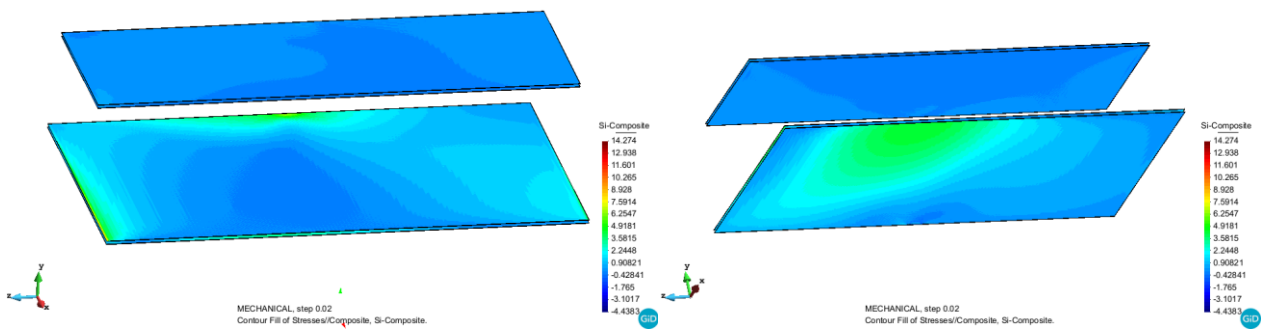


Figure 4.34. The S11 principal tension stress field on the skins of plates under load case 2

The S33 principal compression stress field on the skins of the plates is shown in figure 4.35. In load case 2, the maximum S33 principal stress still happens on the bottom boundary condition area and its value is -22.582 MPa . On other parts of the plates, the S33 stresses are not large.

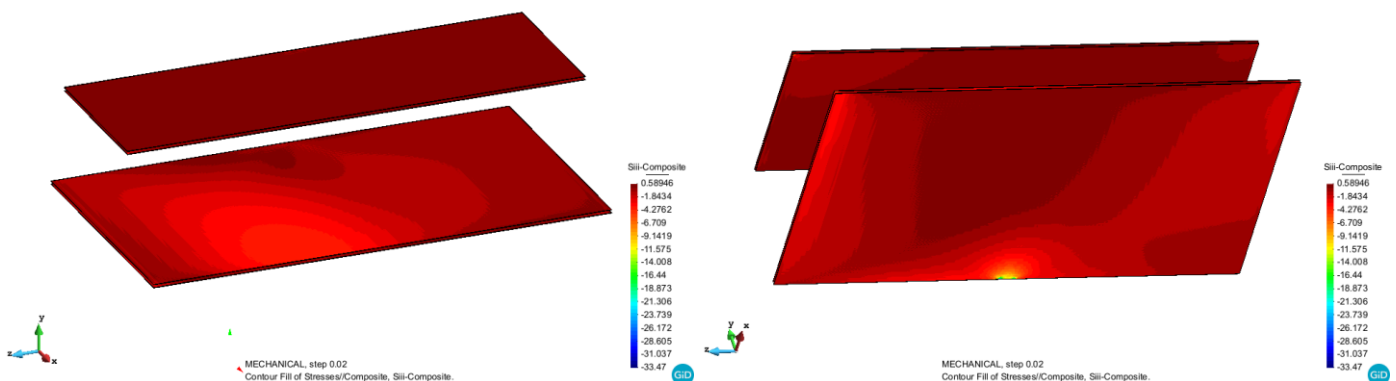


Figure 4.35. The S33 principal compression stress field on the skins of plates under load case 2

As we can see, the maximum S11 and S33 stresses on the skins of plates are both lower than the stress threshold of the glass fiber, which is 400 MPa.

Core

The S11 principal tension stress field on the cores of the plates is shown in figure 4.36. As we can see, the S11 stress field becomes nonsymmetric. The right and front corners of the bottom plate have large S11 stresses under the load case 1. However, in load case 2, the areas with large S11 stresses only have the area around the bottom boundary condition and the left and front corner. The maximum S11 stress is 0.06014 MPa and it has decreased compared to load case 1.

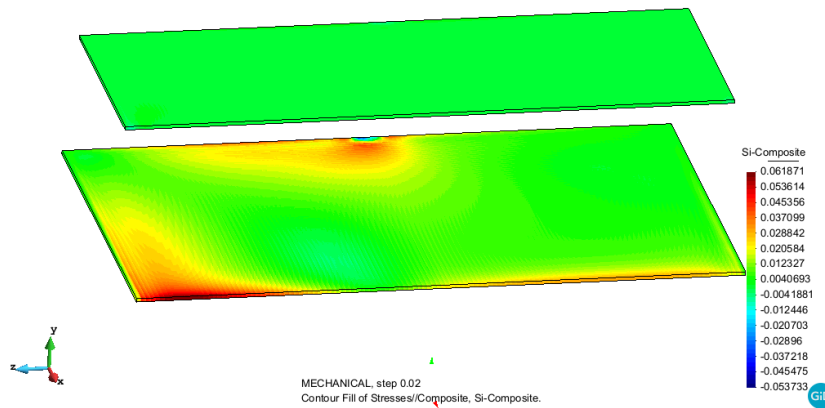


Figure 4.36. The S11 principal tension stress field on the skins of plates under load case 2

The S33 principal compression stress field on the cores of the plates is shown in figure 4.37. The S33 stress distribution is similar to the S11 stress distribution. The left and front corner of the bottom core and the boundary condition area have large S33 stresses. The maximum S33 stress is -0.10184 MPa and its value becomes smaller compared to load case 1.

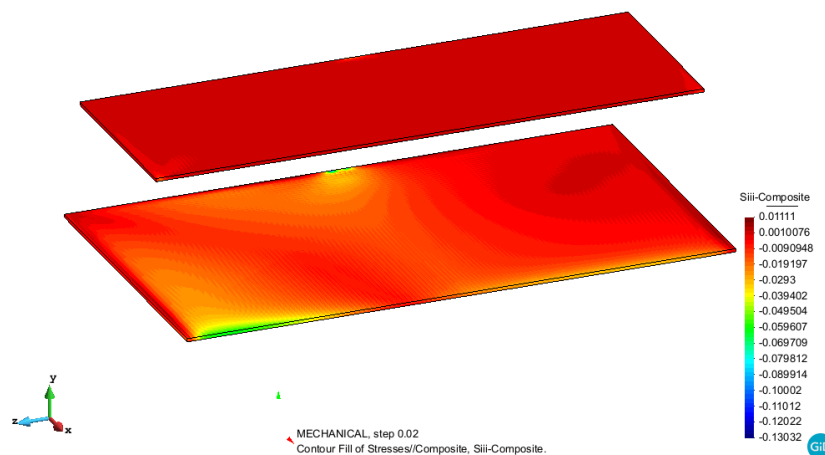


Figure 4.37. The S33 principal compression stress field on the skins of plates under load case 2

As we can see, the maximum S11 and S33 stresses on the cores of the plates are both lower than the stress thresholds of the foam material, which are 1.9 MPa for the tension strength and -0.6 MPa for the compression strength.

ii. Sides area

Skin

Figure 4.38 shows the S11 principal tension stress field on the skins of the sides. Taking a comparison between load case 1 and load case 2, we can find that the areas where the stresses are large become much smaller in load case 2. The upside boundary condition area on the outer skin of left side and the cross areas between the skins of left side and plates have large stresses. The maximum S11 stress value is 24.789 MPa , which is smaller than it in load case 1.

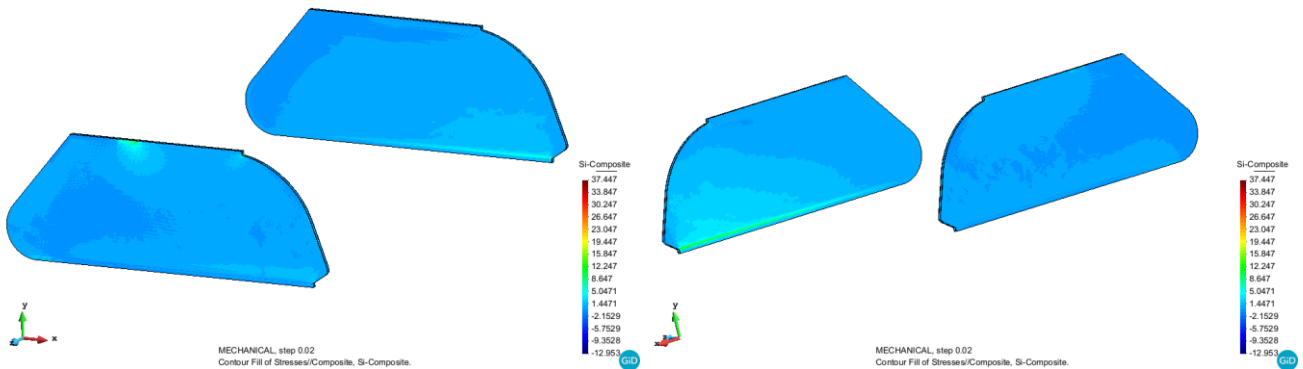


Figure 4.38. The S11 principal tension stress field on the skins of sides under load case 2

Figure 4.39 shows the areas where the S11 principal tension stresses are large and they are all on the left side, which is the difference between load case 1 and load case 2. Now, combining the results from two load cases, we are able to implement corresponding reinforcements on those areas having large stresses as shown.

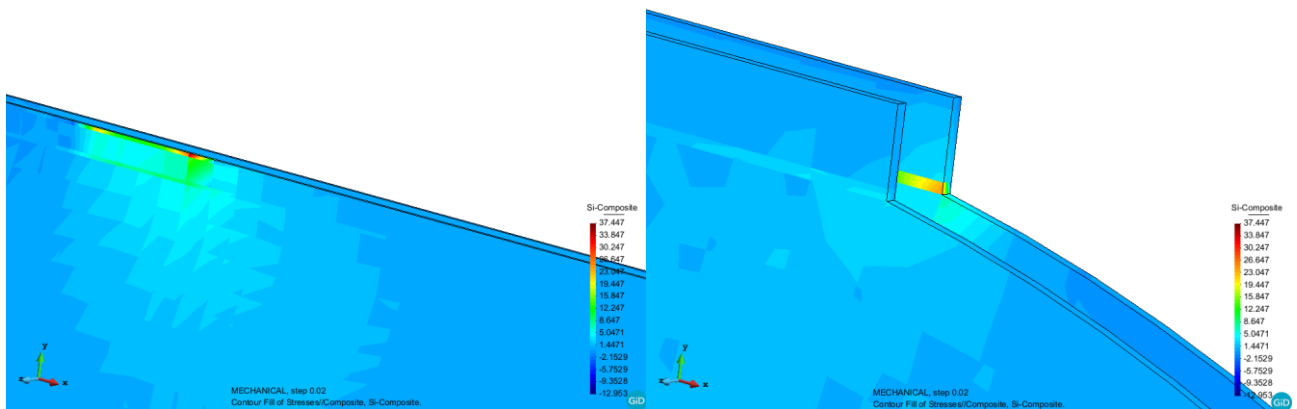


Figure 4.39. The large S11 principal tension stress areas on the skins of sides under load case 2

The S33 principal compression stress field on the skins of the sides is shown in figure 4.40. On the most areas,

Analysis of the airplane interior cabin bin (Hatrack)

the stresses are small. However, as we can see above, the cross areas between the skins of plates and the skins of sides could have large stresses and this still applies here. The maximum S33 principal stress appears on the cross area between the inside skin of the bottom plate and the inside skin of the left side. Its value is -31.083 MPa and this is smaller than the load case 1.

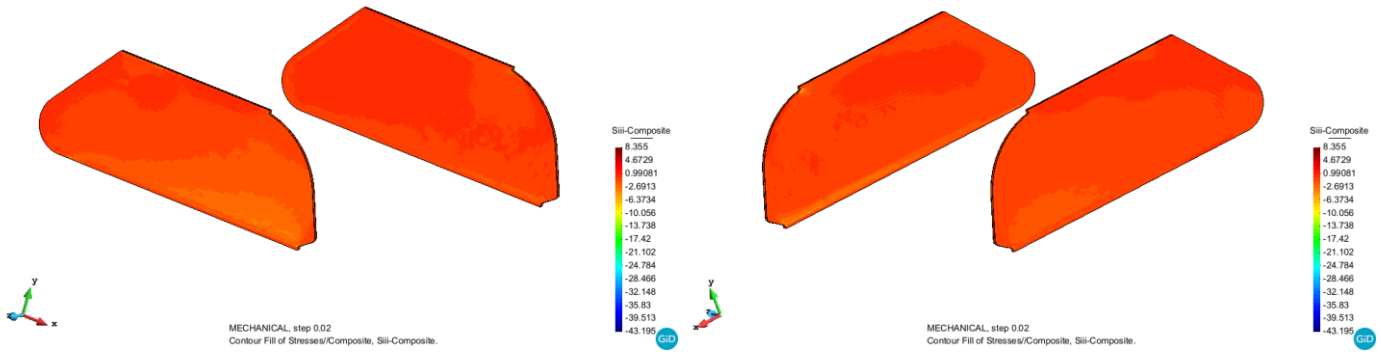


Figure 4.40. The S33 principal compression stress field on the skins of sides under load case 2

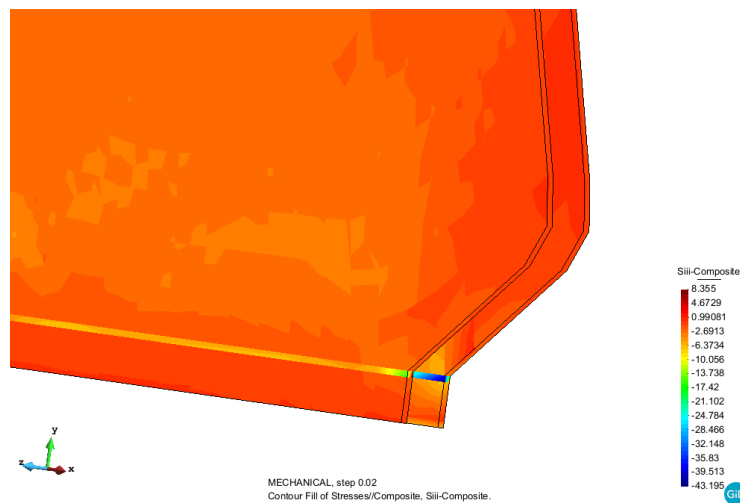


Figure 4.41. The large S33 principal compression stresses on the skins of sides under load case 2

Figure 4.41 shows the area having large S33 principal compression stresses.

As we can see, the maximum S11 and S33 stresses on the skins of sides are both lower than the stress threshold of the glass fiber, which is 400 MPa .

Core

The S11 principal tension stress field on the cores of the sides is shown in figure 4.42. The large S11 stresses are appearing on the cross area between the cores of left side and the cores of the bottom plate. And the maximum S11 stress is 0.11124 MPa , which has also decreased.

The S33 principal compression stress field on the cores of the sides is shown in figure 4.43. From this figure we can find that the S33 stresses are small on the most areas of the cores of the sides. And the large S33 stresses can be found on the bottom face of the left side and the maximum S33 stress is -0.32372 MPa , whose absolute value also decreases compared to the load case 1.

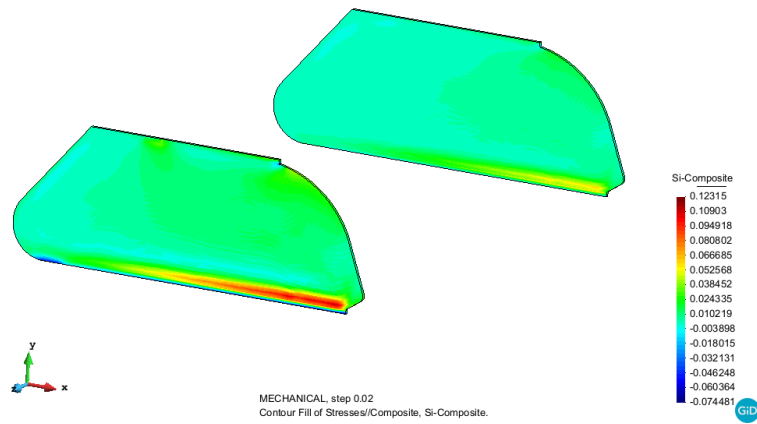


Figure 4.42. The S11 principal tension stress field on the cores of sides under load case 2

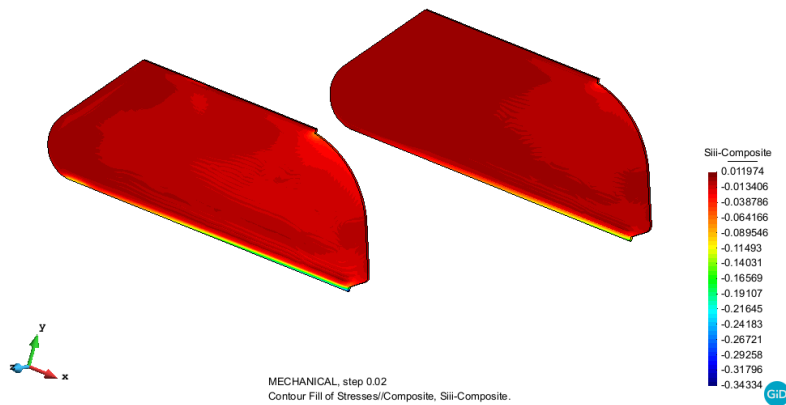


Figure 4.43. The S33 principal compression stress field on the cores of sides under load case 2

The figure 4.44 has shown the large S33 principal compression stress on the cores of the sides.

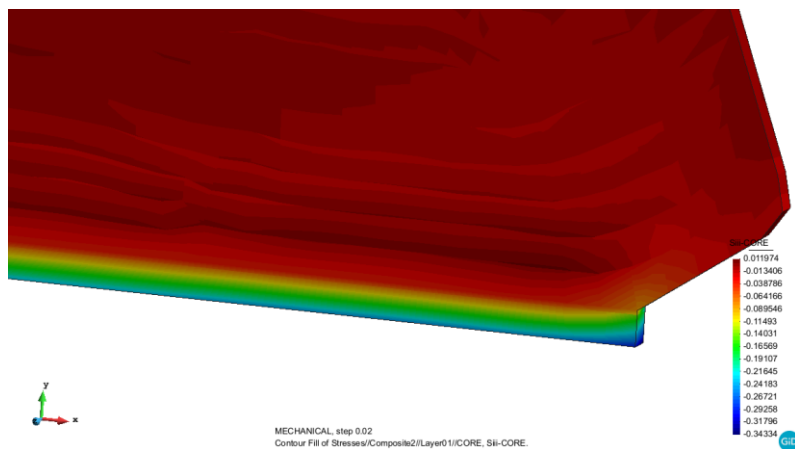


Figure 4.44. The large S33 principal compression stress on the cores of sides under load case 2

As we can see, the maximum S11 and S33 stresses on the cores of the sides are both lower than the stress thresholds of the foam material, which are 1.9 MPa for the tension strength and -0.6 MPa for the

compression strength.

iii. Back area

Skin

From figure 4.45 we can see the S11 principal tension stress field on the skins of the back part under load case 2. The S11 stresses near the bottom boundary condition area are large. And the maximum S11 principal stress is 10.633 MPa , which is smaller than the load case 1.

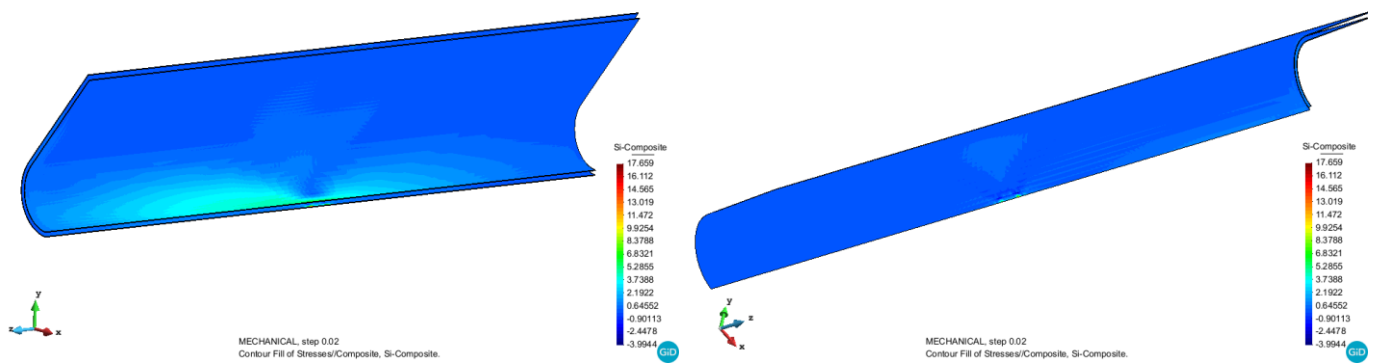


Figure 4.45. The S11 principal tension stress field on the skins of back part under load case 2

The bottom boundary condition area with large S11 principal tension stresses is shown in figure 4.46. Unlike the results in load case 1 that the stress field is symmetric, the S11 stresses are comparatively larger on the left part.

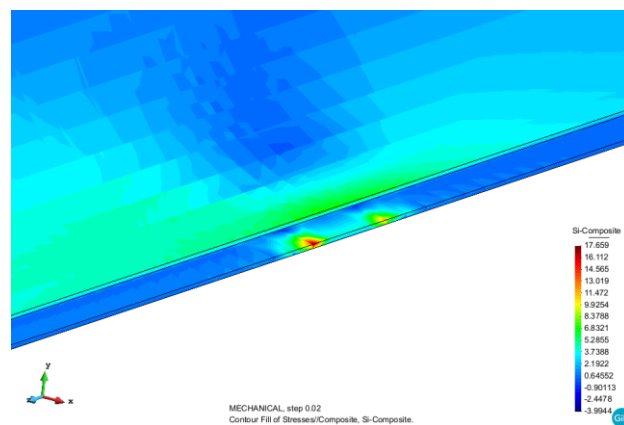


Figure 4.46. The large S11 principal tension stresses on the skins of back part under load case 2

Figure 4.47 shows the S33 principal stress field on the skins of the back part under load case 2. Except the bottom boundary condition area, other areas of the skins of the back part are under small S33 principal compression stresses. And the maximum value in this situation is -13.795 MPa and its absolute value is smaller compared to load case 1.

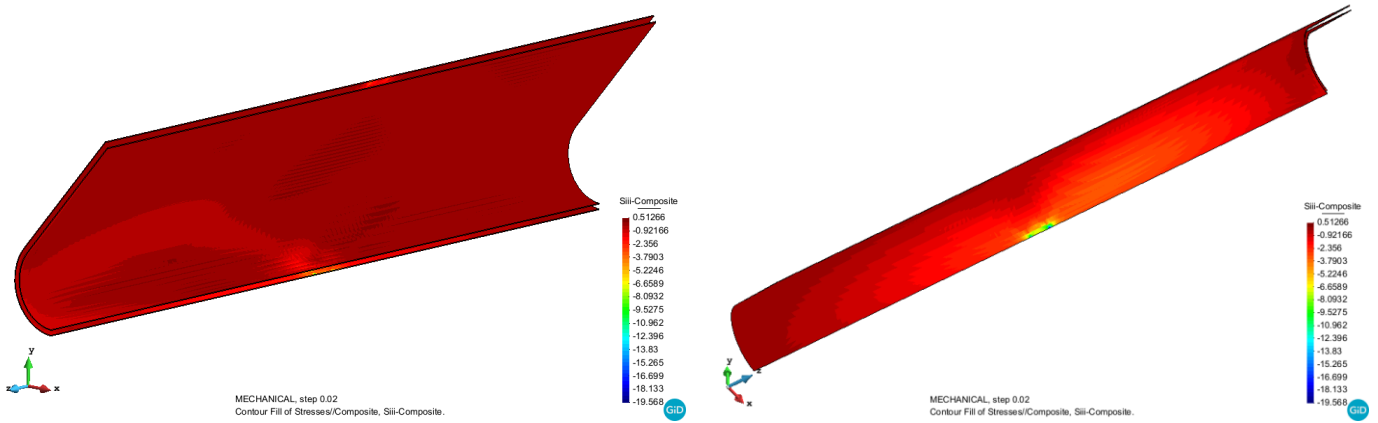


Figure 4.47. The S33 principal compression stress field on the skins of back part under load case 2

As we can see, the maximum S11 and S33 stresses on the skins of back part are both lower than the stress threshold of the glass fiber, which is 400 MPa.

Core

In figure 4.48, the S11 principal tension stress field on the core of the back part can be seen. On the curved part of the core, the stresses are large, especially on the area around the bottom boundary condition. The maximum S11 stress has decreased to 0.077295 MPa in load case 2. The S11 stresses are small on the flat part of the core.

Figure 4.49 shows the S33 principal compression stress field on the core of the back part. Unlike the situation of S11 stress field that the S11 stresses are large on the curved part of the core, the area with large S33 stresses is only the bottom boundary condition area. The maximum S33 stress is $-0.10382 MPa$, also becomes smaller.

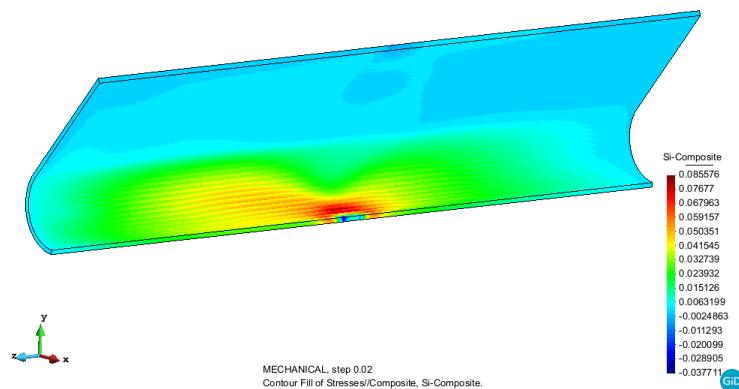


Figure 4.48. The S11 principal tension stress field on the core of back part under load case 2

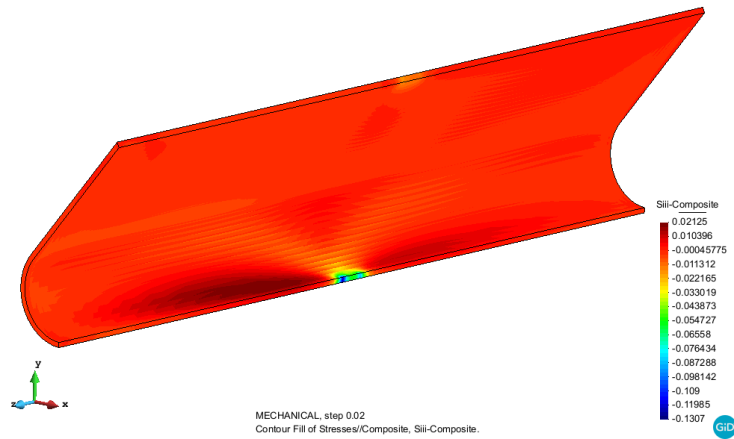


Figure 4.49. The S33 principal compression stress field on the core of back part under load case 2

As we can see, the maximum S11 and S33 stresses on the cores of back part are both lower than the stress thresholds of the foam material, which are 1.9 MPa for the tension strength and -0.6 MPa for the compression strength.

Bending stress field

Skin

The Sxx bending stress field on the skins of the plates under load case 2 is shown in figure 4.50. Comparing the corresponding stress field in load case 1, we can find that Sxx stresses are smaller in load case 2, although the torque force exits in this part. The stresses on the skins of upside plate are very small. On the two sides of the skin of the bottom plate, the tension stresses are no longer that large. The large tension stresses happen on the bottom boundary condition area on the inside skin. For the outer skin, the areas around the bottom boundary condition have large compression stresses. And we can find the maximum tension and maximum compression stresses on the bottom boundary condition area. The maximum tension stress is 3.4309 MPa, which has decreased compared to load case 1. The maximum compression stress is -12.715 MPa and its absolute value has also decreased.

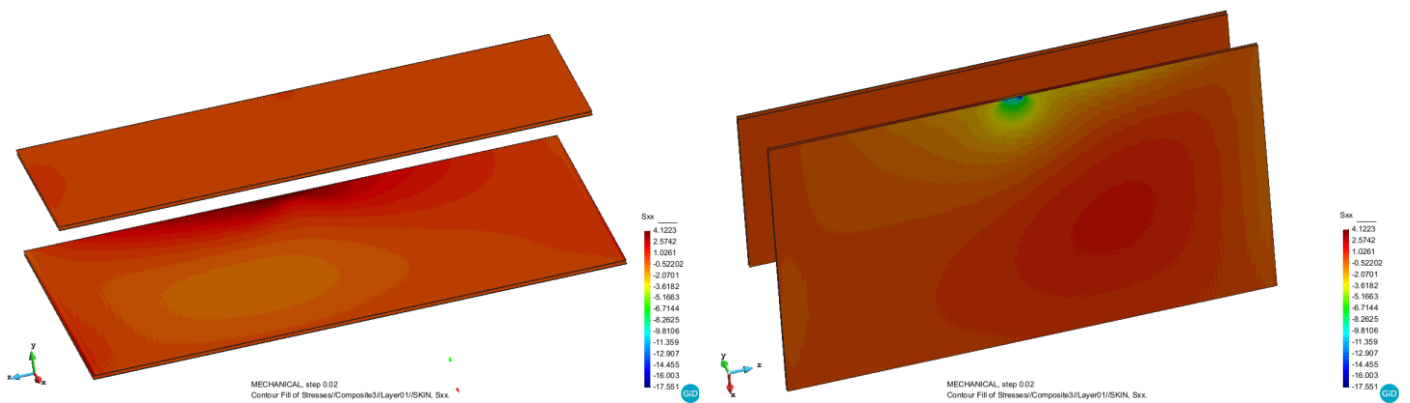


Figure 4.50. The Sxx bending stress field on the skins of plates under load case 2

Figure 4.51 has shown the tension and compression stresses' distribution of the Sxx stresses on the skins of the plate.

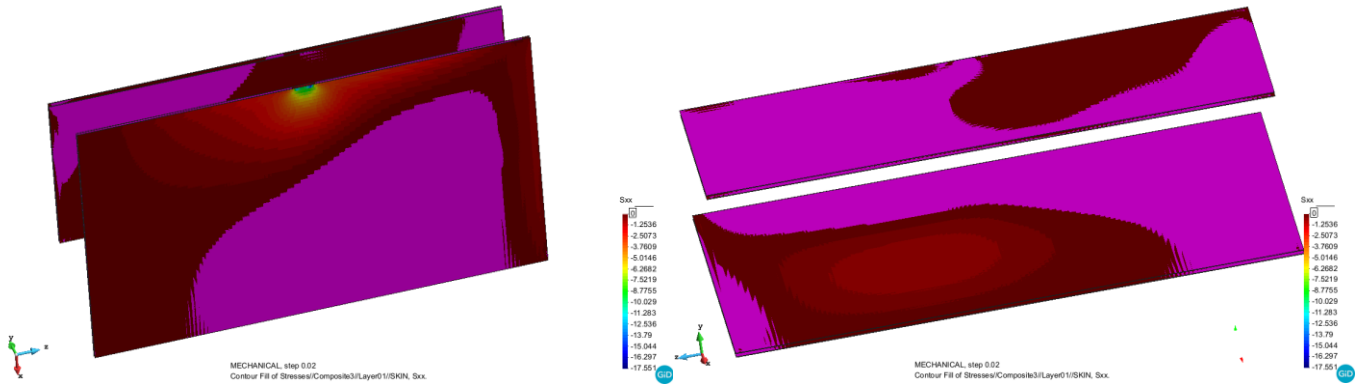


Figure 4.51. The tension and compression stresses' distribution of Sxx stresses on the skins of plates

The Szz bending stress field on the skins of the plates under load case 2 has been shown in figure 4.52. Same as the situation of Sxx stress field, the Szz stress field is no longer symmetric under load case 2. On the skins of the upside plate, the Szz stresses are very small. The left side of the inside skin of the bottom plate has large tension stresses. The large tension stresses also happen on the bottom boundary condition area on the inside skin and the most of the left part of the outer skin. On other areas of the skins, the compression stresses can be found. On the inside skin, the large compression stresses occur on the corresponding area where the tension stresses are large on the outer skin. It is same for the large compression stresses distribution on the outer skin and we can find them on the bottom boundary condition area and the left side. The maximum Szz tension stress is 4.2785 MPa and the maximum Szz compression stress is -9.7646 MPa . These values also have decreased compared to load case 1.

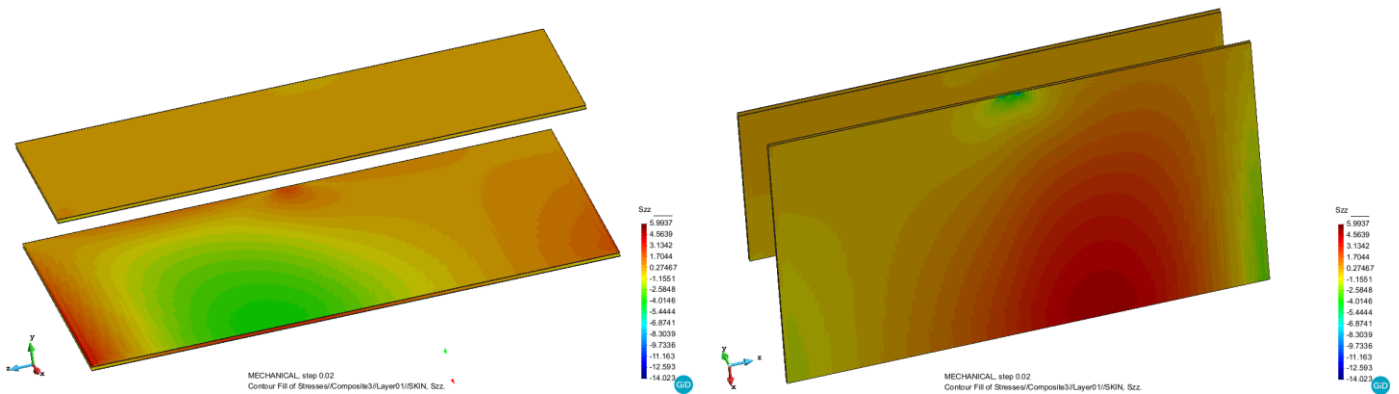


Figure 4.52. The Szz bending stress field on the skins of plates under load case 2

Analysis of the airplane interior cabin bin (Hatrack)

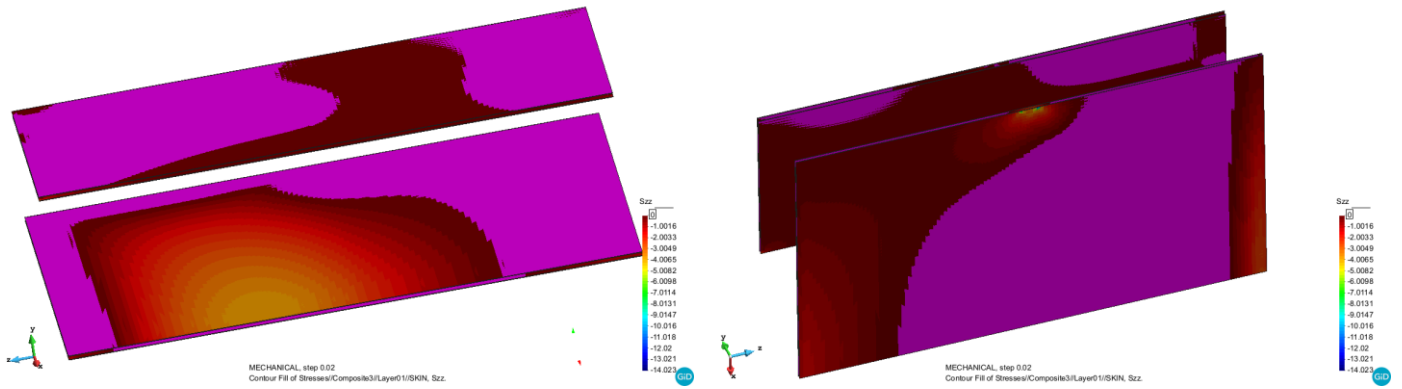


Figure 4.53. The tension and compression stresses' distribution of Szz stresses on the skins of plates

Figure 4.53 shows the tension and compression stresses' distribution of the Szz stresses on the skins under load case 2.

Core

The Sxx bending stress field on the cores of the plates under load case 2 has been shown in figure 4.54. The distribution of the Sxx stresses on the cores is similar to the situation of skins. Except that on the bottom boundary condition area we can only find the large compression stresses, although the large tension stresses appear on the areas near the bottom boundary condition. The maximum tension stress is 0.016763 MPa and the maximum compression stress is -0.054337 MPa.

The tension and compression stresses' distribution of Sxx stresses is shown in figure 4.55.

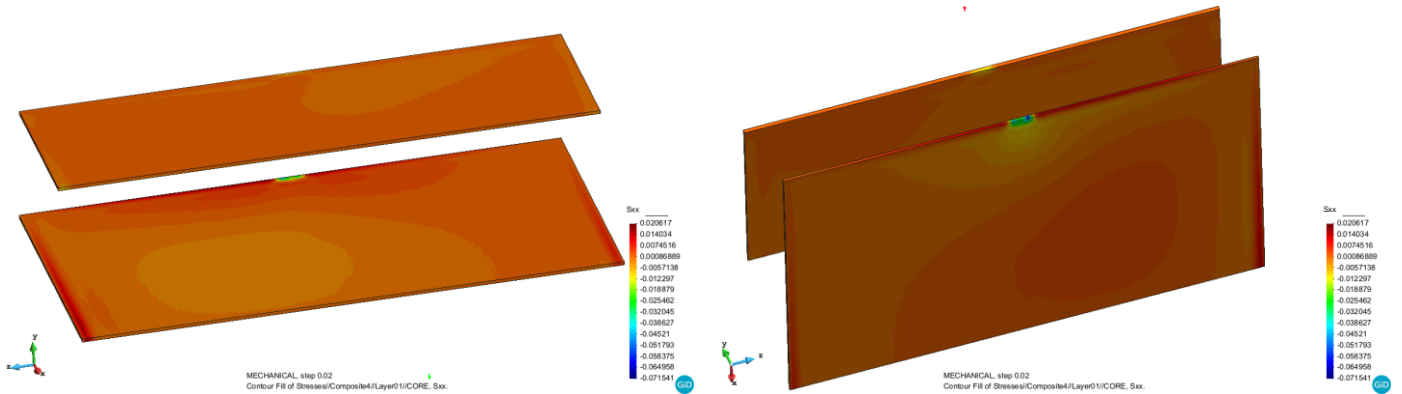


Figure 4.54. The Sxx bending stress field on the cores of plates under load case 1

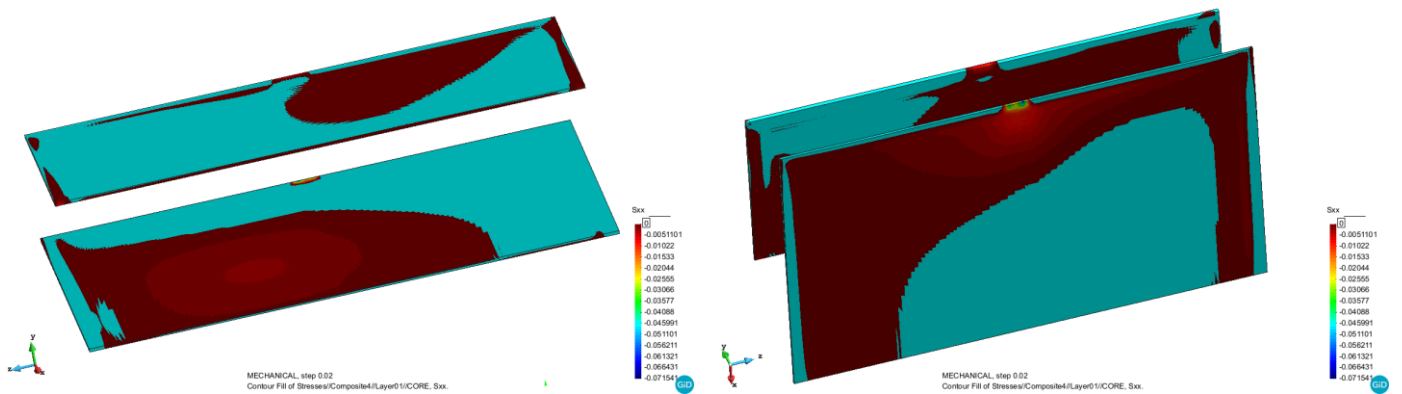


Figure 4.55. The tension and compression stresses' distribution of Sxx stresses on the cores of plates

Analysis of the airplane interior cabin bin (Hatrack)

The Szz bending stress field on the cores of the plates under load case 2 is shown in figure 4.56. As we can see, the distribution of the Szz stresses is similar to the case of Sxx stresses. The maximum tension stress happens on the left side of the core and its value is 0.015108 MPa . The maximum compression stress is -0.052908 MPa and it can be found on the bottom boundary condition area.

The Szz tension and compression stresses' distribution is shown in figure 4.57.

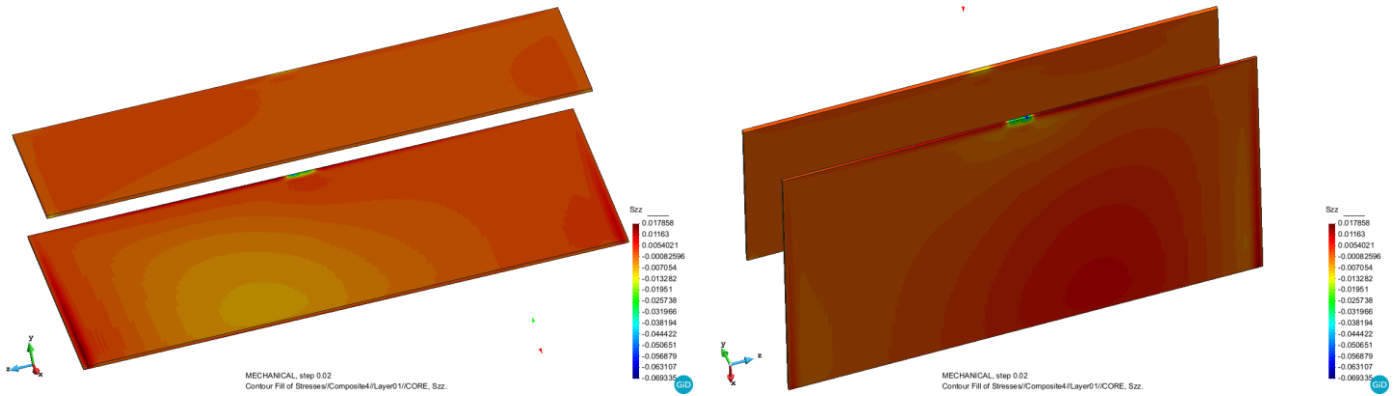


Figure 4.56. The Szz bending stress field on the cores of plates under load case 1

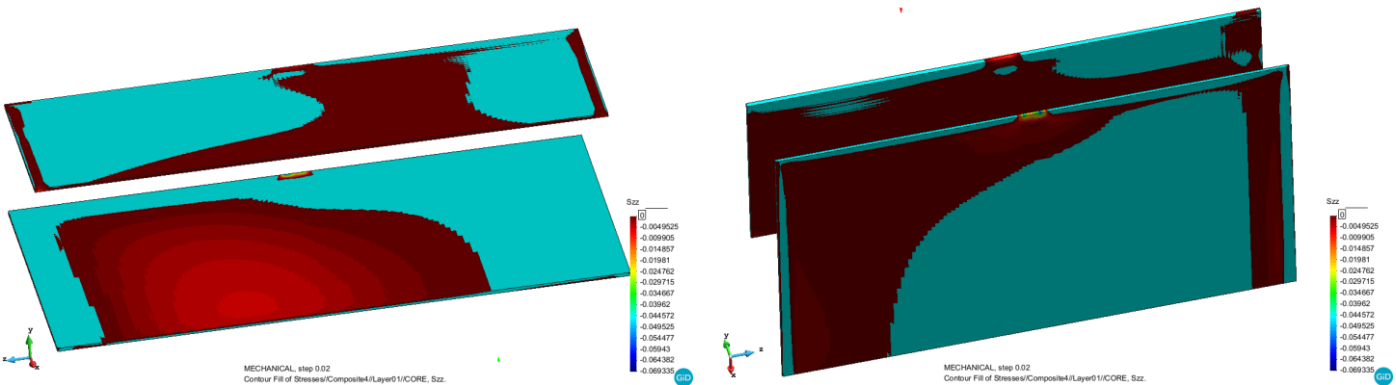


Figure 4.57. The tension and compression stresses' distribution of Szz stresses on the cores of plates

4.2.4 Conclusions

From above contents that we have discussed, we can get some useful conclusions to guide our design and optimization of the structure:

i) The load case 1 is more dangerous than the load case 2, since the principal stresses S11 and principal stress S33 on every part of the structure under load case 1 is larger than the load case 2. Consequently, the following part about multiscale analysis will only focus on the load case 1.

ii) The areas that have large principal stresses S11 and principal stress S33 should be taken into attention to implement measurements to reduce the stress concentrations produced by the supports and the crossing between bottom plate and sides. Like replacing the materials on those areas to the materials with higher

stiffness. These areas include the upside boundary condition area on the sides, the bottom boundary condition area on the bottom plate and the back part, and the cross areas between the sides and bottom plates. On other areas of the cabin bin, the stresses are not large.

iii) Thanks to the outstanding mechanical properties of sandwich structure, the core part of the structure has undertaken very small stresses and the skins are under much larger stress field, meaning that we can build lighter structure with higher stiffness.

iv) The maximum S11 and S33 stresses are both found in load case 1. On the skins, the maximum S11 principal tension stress is found on the upside boundary condition area of the sides and its value is 29.539 MPa . For the maximum S33 principal compression stress, it happens on the cross area between the inside skin of bottom plate and the inside skins of two sides, whose value is -51.369 MPa .

On the cores, the maximum S11 principal tension stress happens on the cross area between the core of bottom plate and the core of two sides and its value is 0.15557 MPa . The maximum S33 principal compression stress is appearing on the bottom face of two sides and the value is -0.45437 MPa .

By comparing the maximum stresses on the skins and cores with the materials used, we can find the performance of the cabin bin with isotropic materials. Since the strength of the glass fiber is 400 MPa , the stresses on the skins of cabin bin under two load cases are both lower than the its stress threshold. And for the foam core, its tension strength is 1.9 MPa and compression stress is -0.6 MPa . Therefore, the stresses on the cores of the cabin bin are also below the stress threshold of the foam cores.

4.3 Analysis with a multiscale procedure

4.3.1 Material, RVEs

In this part, the sandwich structure is still used for our model. The skin part corresponds to RVE_01 and the core part is the material represented by RVE_02. The RVE_02 is a honeycomb structure. The two RVEs and corresponding microstructures are shown in figure 4.58. The RVE_01 has three components: Fiber on X direction, Fiber on Y direction and matrix. For the RVE_02, there is only the matrix that has been implemented.

In RVE_01, the fibers on X and Y directions are woven ramie fibers and the matrix is epoxy matrix. The honeycomb structure (RVE_02) is manufactured from high temperature resistant aramid paper formed into a honeycomb structure, and coated with a phenolic resin [17]. The tension strength and compression strength of epoxy are 85 MPa and -112 MPa [18]. For the ramie fiber, its tension strength is about 560 MPa [19]. The strength of the honeycomb structure as a simple material is 2.4 MPa [17].

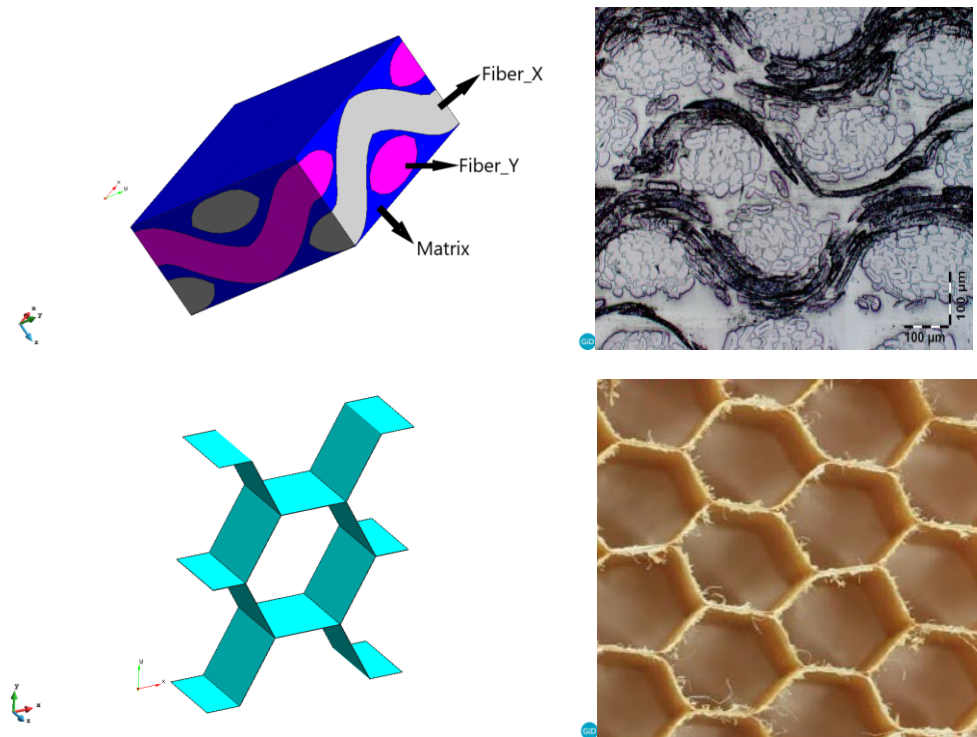


Figure 4.58. The RVE models for the skin and core together with the real microstructures (Upside: RVE_01, down: RVE_02)

Table 4.5 shows the material properties of the fibers and matrix used for RVE_01. The materials implemented here are all isotropic and nonlinearity is considered. Shear modulus are set to be zero in this part.

Material properties of the components		
Components	Young Modulus (MPa)	Poisson Ratio
Fiber_X (Woven ramie)	24000	0.01
Fiber_Y (Woven ramie)	24000	0.01
Matrix (Epoxy)	3500	0.25

Table 4.5. Material properties for the components of RVE_01

With above components, the material properties of the RVE_01 as a simple material are shown in table 4.6. The RVE_01 becomes anisotropic as the table 4.6 has presented. The material properties are obtained from the initial analysis of the RVE in which it has loads from different space directions in order to get the elastic stiffness tensor of the material, which is required by the FEM to evaluate the structure stiffness. Then, the anisotropic material parameters that define the composites can be obtained from the material stiffness tensor. Those are the ones shown in table 4.6 and table 4.8 for RVE_01 and RVE_02.

The RVE_01 Material properties			
Young Modulus (MPa)	Exx	Eyy	Ezz
	11750.02	11822.1	9907.3
Shear Modulus (MPa)	Gxy	Gxz	Gyz
	5239.05	4750.49	4733.67
Poisson Ratio	Pxy	Pyx	Pxz
	0.0804	0.0799	0.1115
	Pzx	Pyz	Pzy
	0.1323	0.11	0.1313

Table 4.6. The material properties of RVE_01 as a simple material

In table 4.6, we can see that Exx and Eyy are very close, this is because that the ramie fibers' distributions on X and Y directions are very similar. The slight difference is caused by that the RVE is developed from an image of the real material in which the fibers on X and Y directions are not exactly same. On the other hand, since the ramie fibers are not oriented in Z direction, Ezz is smaller than Exx and Eyy. For the Shear Modulus, the similar situation is found that Gxz and Gyz are very close but not exactly same while Gxy is larger.

In this part, we have implemented the honeycomb structure to the core parts, which has huge empty spaces. This leads to the increases of the stresses on the core parts, even though we will see that the stresses on the cores shown in macroscopic are still very small. This difference is caused by the computation procedure that the stresses on the macroscopic scale are the results of the volumetric average of the microscopic stresses in the RVE. As a result, the material with high stiffness and high strength is used to avoid the damage on the core parts.

The material property of the matrix of the RVE_02 is shown in table 4.7. The matrix is anisotropic for the Shear Modulus. The Shear Modulus on XZ direction is set to be 12000 MPa and on other directions it will be zero.

Material properties of the components			
Components	Young Modulus (MPa)	Shear Modulus (XZ, MPa)	Poisson Ratio
Matrix (Aramid paper)	18000	12000	0.3

Table 4.7. Material properties for the matrix of RVE_02

The material properties of RVE_02 as a simple material has been shown in table 4.7. We can see that the values of the Young Modulus and Shear Modulus on all directions are much smaller compared to RVE_01. For the Poisson Ratio, the Pxy and Pyx are larger than 0.5, which seems wrong since the Poisson Ratio should be less than 0.5. However, this makes sense for the honeycomb structure, as it will decrease its volume considerably when the forces are applied. For other materials like metal, the volume is assumed to be incompressible, which limits the maximum value of Poisson Ratio to 0.5. Therefore, because of the failure of

the incompressibility assumption for the honeycomb structure, the limitation of Poisson Ratio is no longer appropriate in this case. In PLCd, the limitation of the Poisson Ratio exits in the setting section of materials. Consequently, Pxy and Pyx are both set as 0.45 to satisfy the request.

The RVE_02 Material properties			
Young Modulus (MPa)	E _{xx}	E _{yy}	E _{zz}
	34.88	35.10	138.31
Shear Modulus (MPa)	G _{xy}	G _{xz}	G _{yz}
	10.20	41.06	30.54
Poisson Ratio	P _{xy}	P _{yx}	P _{xz}
	0.5348	0.5313	0.3000
	P _{zx}	P _{yz}	P _{zy}
	0.0756	0.3000	0.0761

Table 4.8. The material properties of RVE_02 as a simple material

From table 4.8 we can also find that the Young’s Modulus on Z direction is much larger compared to the other two directions. This result is reasonable since the stiffness on Z direction is larger than the other two, caused by that the honeycomb cells are oriented on Z direction and there are larger deformations on X and Y directions.

4.3.2 Results

Displacement field

The displacement field of the cabin bin under load case 1, calculated by the multiscale analysis, is shown in figure 4.59. Since we have applied different materials in this part, the maximum displacement happening on the middle of the front edge of the bottom plate becomes larger. From the figure we can see that the value of maximum displacement is -12.691 mm . And except the bottom plate, other parts of the cabin bin have much smaller displacements. Because of the symmetricities existing in the area force, structure and boundary conditions, the displacement field is also symmetric.

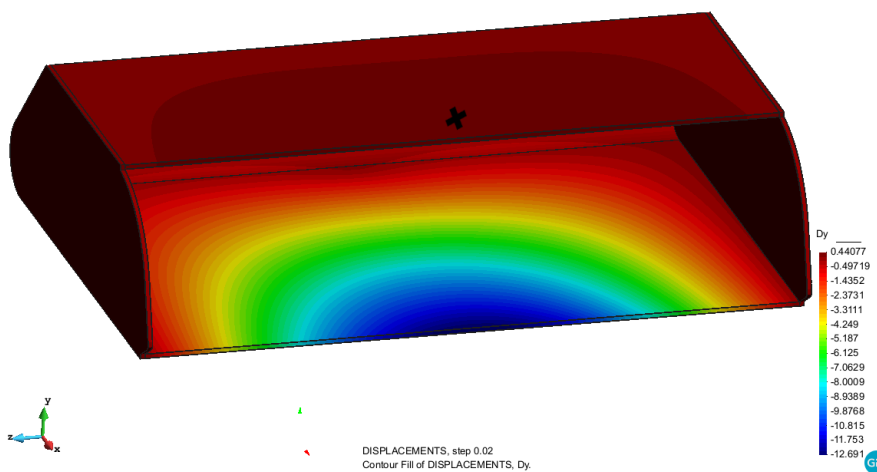


Figure 4.59. The displacement field of the cabin bin under load case 1

Microscopic procedure

The numerical result of the displacement on Y direction of the microscopic procedure is shown in figure 4.60. The RVEs chosen in this part are representing the skin and core of the upside plate. Their positions are shown in figure 4.59 with a fork mark on the upside plate.

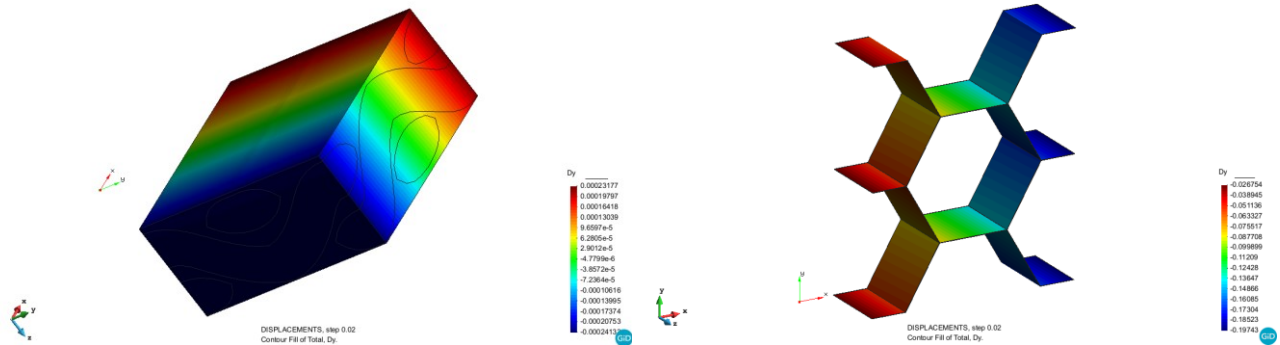


Figure 4.60. The displacement solutions on the chosen RVEs of microscopic procedure

Principal Stress field

The indexes chosen for the discussion about stress field will be S11 principal tension stress and S33 principal compression stress. In order to show the differences on the stress field, caused by the use of the eco-composites, the stresses in following part will be compared to the load case 1 in part 4.2.2. Therefore, the descriptions about the increasing and decreasing of the stresses are all based on the comparison between following part and the load case 1 in part 4.2.2.

Because of the stress concentration phenomenon, a normal numerical issue, we will see that some elements have much larger stresses compared to other areas where this problem is not existing. Therefore, following discussions about the stress field will ignore this phenomenon and the maximum stress pointed out below will be considered under this condition.

Another issue is that since on the macroscopic scale the stresses are calculated as the volumetric average values with respect to the RVEs and the RVE_02 model has very large empty spaces, the stresses on the RVE_02 are actually much larger than the macroscopic stresses on the core parts of the cabin bin. For the RVE_01, the real stresses on the fibers and matrix are close to the average values.

Last, even though the macroscopic stresses on the cores are not the actual stresses, it still has meanings from an average perspective. The macroscopic stresses can point out where the stresses are large and then we can choose the elements on these areas to show the real stresses. In following part, since the real stresses on cores are much larger than the macroscopic stresses, the microscopic stresses on the cores will be shown. And the strength of the honeycomb structure is given as a simple material, therefore it is necessary to compare the macroscopic stresses with the strength to check the safety of the cores of cabin bin.

i. Plates area

Skin

The S11 principal tension stress field of the skin of cabin bin has been shown in figure 4.61. The S11 stresses are not large on the most areas of the plates' skin, especially on the upside plate. The areas having large S11 stresses include the boundary condition area and the two sides of the inside skin of the bottom plate. Without the consideration of stress concentration phenomenon, the maximum S11 stress on the skins of plates is 13.823 MPa, which has decreased.

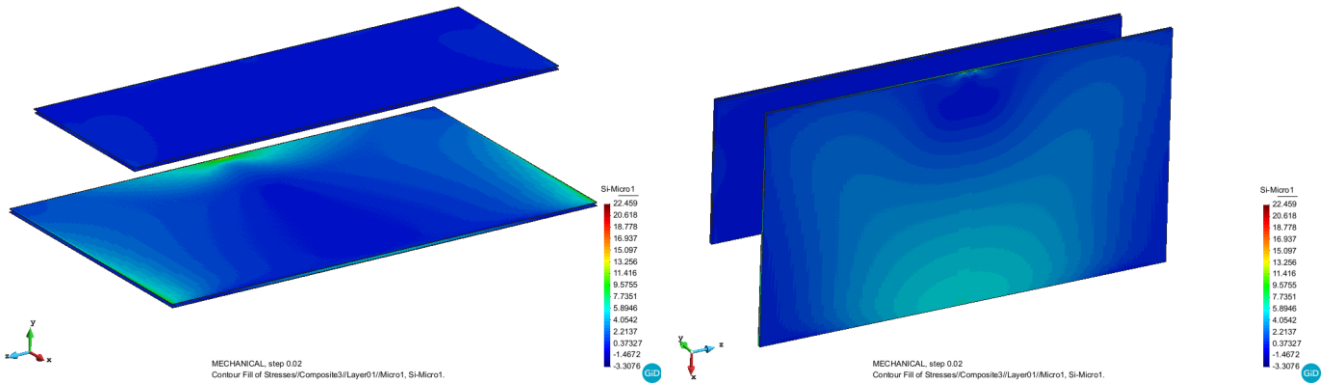


Figure 4.61. The S11 principal tension stress field on the skins of plates under load case 1

The S33 principal compression stress field on the skins of the plates is shown in figure 4.62. Similar to the situation of the S11 stress field, the S33 stresses on the most areas of the plates' skins are small. However, on the boundary condition area where the maximum S33 compression stress appears, the absolute value of the maximum S33 stress is about three times than the maximum S11 stress. The maximum S33 compression stress is -34.798 MPa and its absolute value has decreased. Combining the truth that the S11 also becomes smaller, we can conclude that the application of the eco-composites has helped the structure to decrease the stress field. And this conclusion will be confirmed by following discussions.

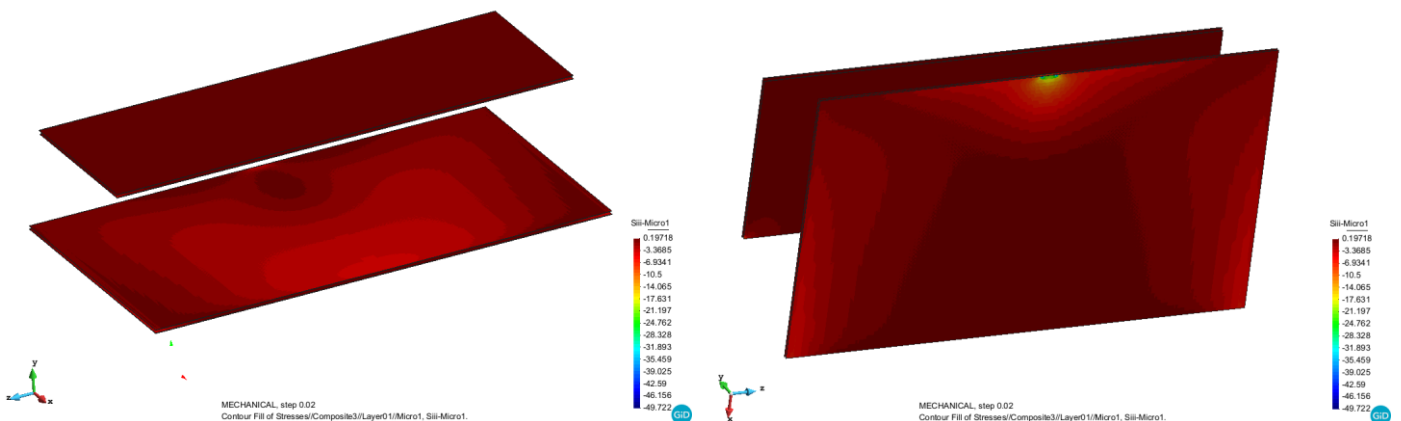


Figure 4.62. The S33 principal compression stress field on the skins of plates under load case 1

As we can see, the maximum S11 and S33 stresses on the skins of plates are both lower than the stress thresholds of the epoxy and ramie fibers.

Core

The chosen elements to show the microscopic S11 and S33 stresses are shown in figure 4.63. They are element 60734, element 38672 and element 24353.

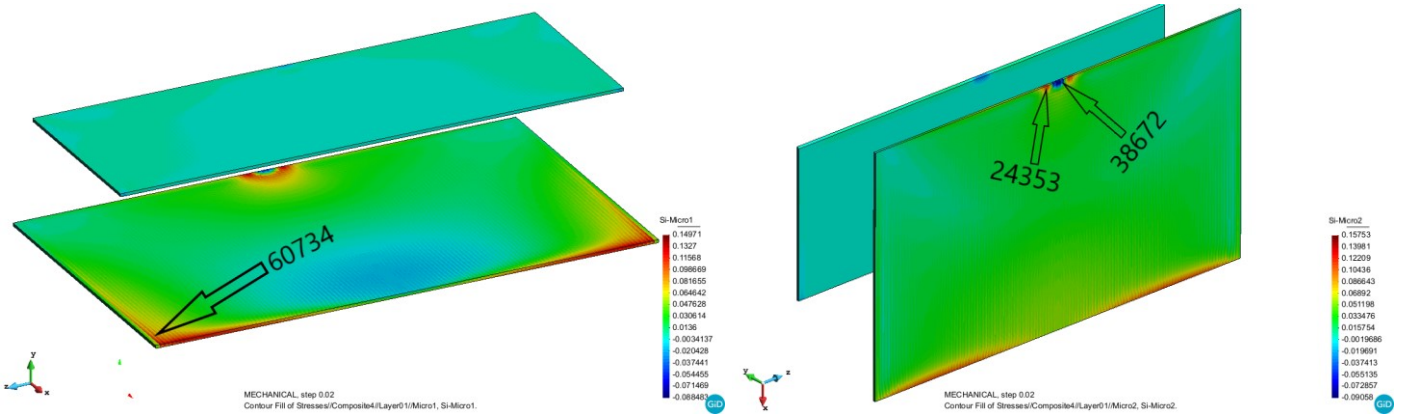
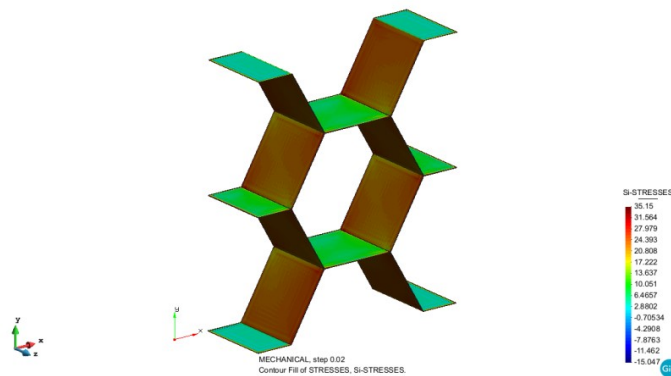


Figure 4.63. The S11 principal tension stress field on the cores of plates under load case 1

The S11 principal tension stress field on the cores of the plates is shown in figure 4.63. Compared to the skins, the S11 stresses on the cores are much smaller. The areas where the S11 stresses are large on the cores are similar to the situation of skins. The S11 stresses are large on the boundary condition area of the bottom core and the bottom core’s front corners. And the maximum S11 stress is 0.13217 MPa, which becomes larger.

The microscopic S11 stress fields on the RVEs of element 60734, element 38672 and element 24353 are shown in figure 4.64. On the RVE of element 60734, the maximum S11 stress is 35.15 MPa. The maximum S11 stress on the RVE of element 38672 is close to the RVE of element 60734 and its value is 35.043 MPa. The maximum S11 stress on the RVE of element 24353 is 71.751 MPa, about doubling the maximum S11 stresses on the other two RVEs.



Analysis of the airplane interior cabin bin (Hatrack)

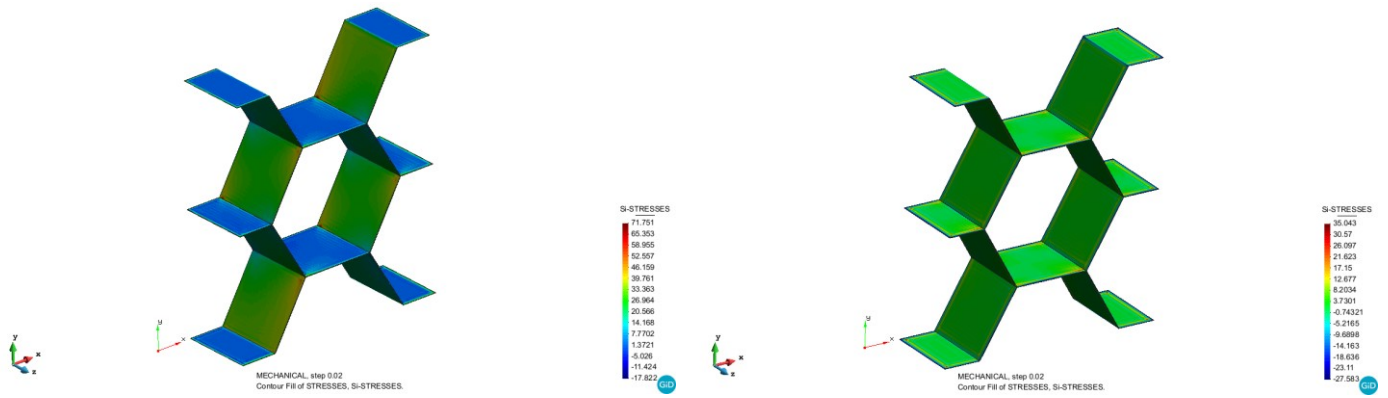


Figure 4.64. The microscopic S11 stresses on the RVE_02 of element 60732, element 24353 and element 38672 (Upside: element 60732, down left: 24353, down right: 38672)

The S33 principal tension stress field on the cores of the plates is shown in figure 4.64. The large S33 stresses appear on the same areas where the S11 stresses are large. And the maximum S33 compression stress is -0.34478 MPa and this value is about doubling the value in the load case 1 in part 4.2.2.

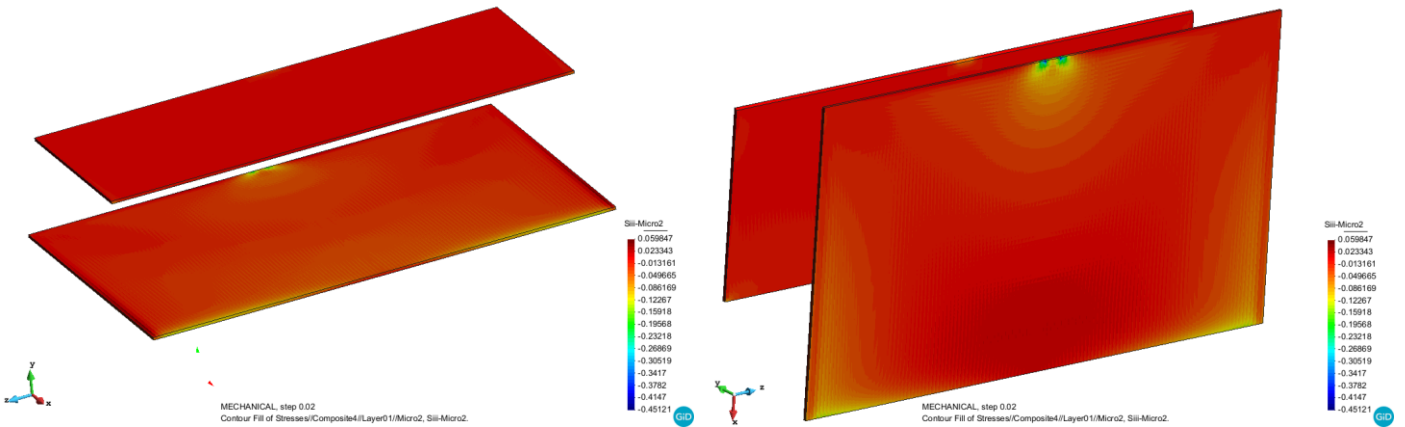
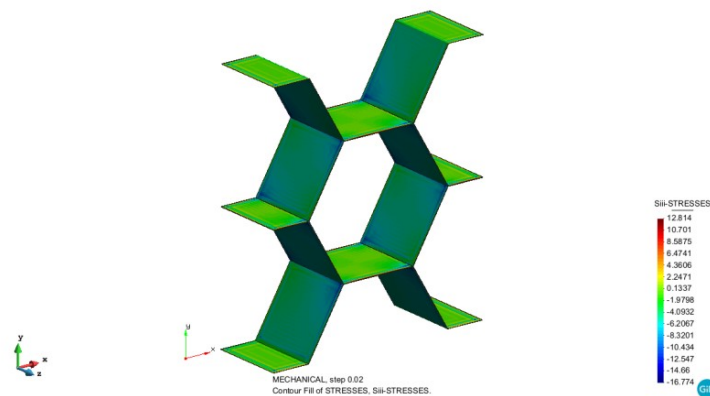


Figure 4.65. The S33 principal compression stress field on the cores of plates under load case 1



Analysis of the airplane interior cabin bin (Hatrack)

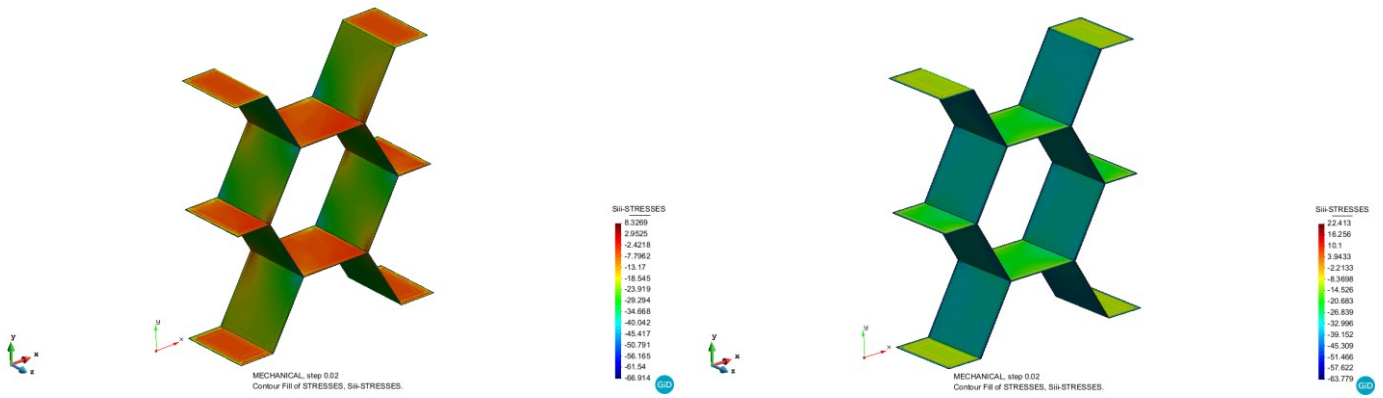


Figure 4.66. The microscopic S11 stresses on the RVE_02 of element 60732, element 24353 and element 38672 (Upside: element 60732, down left: 24353, down right: 38672)

In figure 4.66, we can see the microscopic S33 stress fields on the RVEs of chosen elements. The element 60734 RVE's maximum S33 stress is much smaller compared to other two element and the value is -16.774 MPa . On the RVE of element 24353, the S33 compression stress is also very large and the maximum S33 stress is -66.914 MPa . For the RVE of element 38672, its maximum S33 stress is -63.779 MPa , which is also very large.

As we can see, the maximum S11 and S33 stresses on the cores of plates are both lower than the stress thresholds of the honeycomb structure as a simple material, which is 2.4 MPa .

ii. Sides area

Skin

The S11 principal tension stress field on the skins of the sides is shown in figure 4.67. From this figure we can see that the S11 stresses are large on the upside boundary condition area of the outer skin and the cross areas between the skins of plates and sides. Except on these areas, the S11 stresses are small. The maximum S11 stress is 27.028 MPa , which is smaller than it in the load case 1 in part 4.2.2.

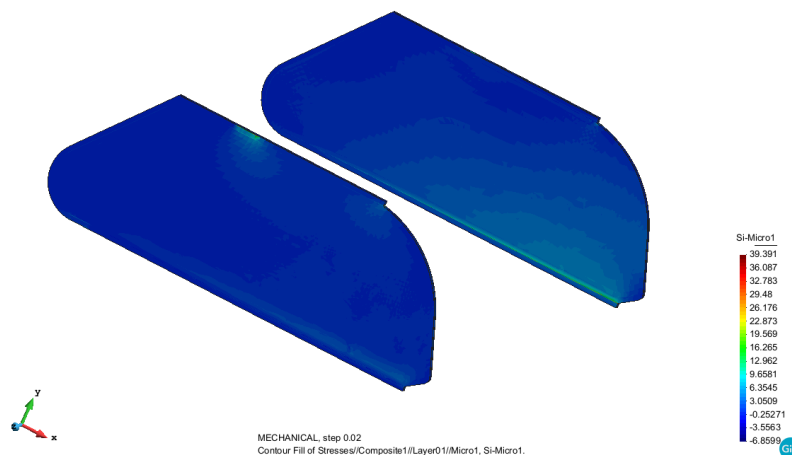


Figure 4.67. The S11 principal tension stress field on the skins of sides under load case 1

Figure 4.68 shows where the S11 principal tension stresses are large.

Analysis of the airplane interior cabin bin (Hatrack)

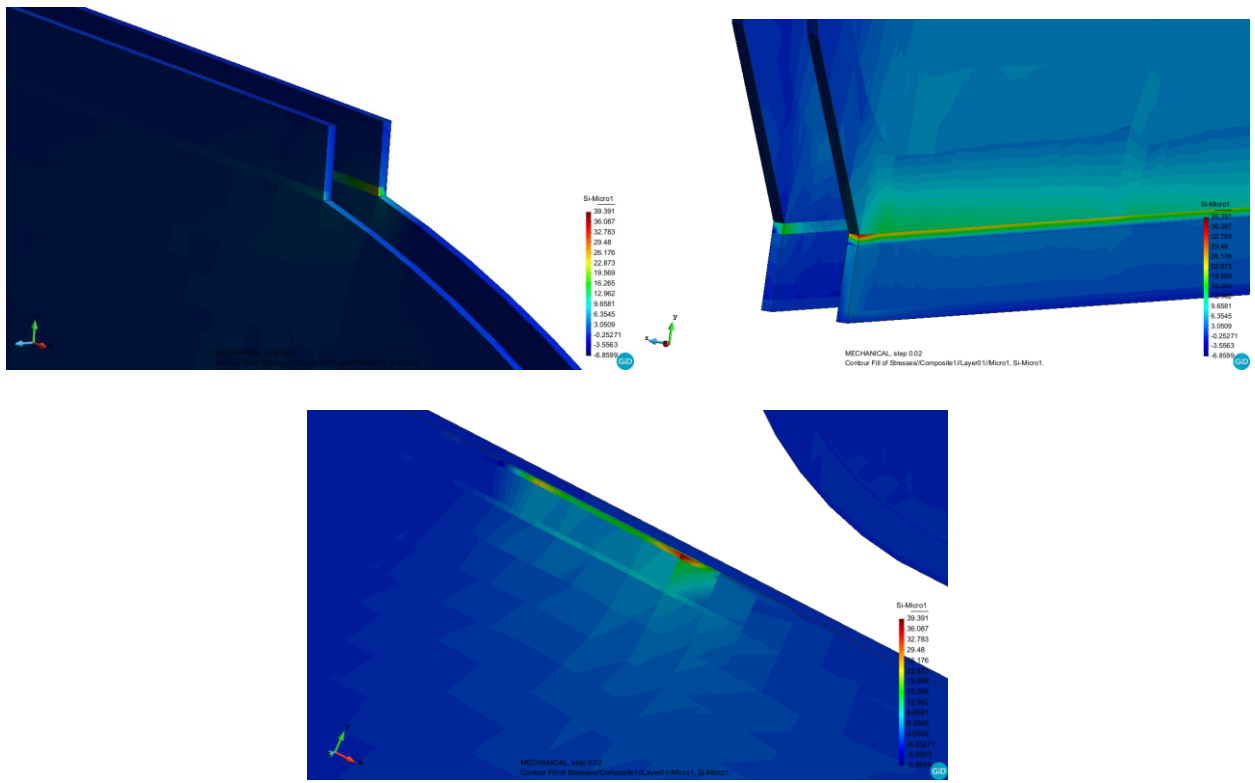


Figure 4.68. The large S33 principal compression stresses on the skins of sides under load case 1 (Up: cross areas between skins of the plates and sides, down: the upside boundary condition area on the outer skin of sides)

The S33 principal compression stress field on the skins of the sides is shown in figure 4.69. The maximum S33 stress is -40.873 MPa and it happens on the cross areas between the inside skin of bottom plate and the skins of sides. Comparing this maximum S33 stress with the corresponding value in the load case 1 in part 4.2.2, whose value is -51.369 MPa , its absolute value has decreased. As we know from above discussion, on this area, the S11 stress is also very large. Therefore, this area is the most dangerous area on the skins of the sides under the load case 1.

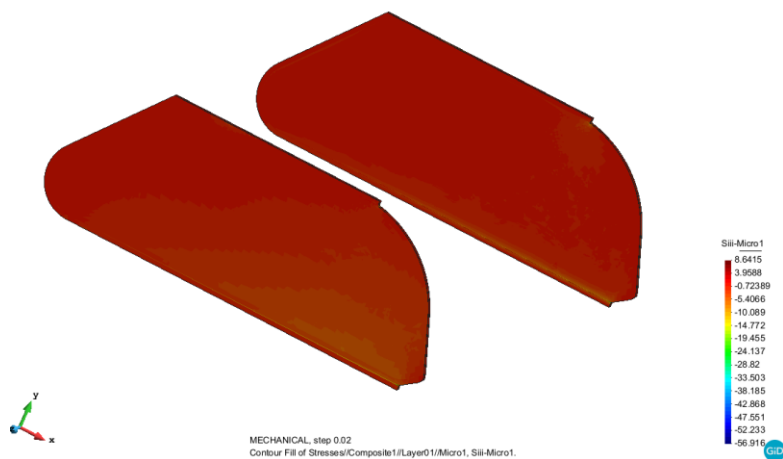


Figure 4.69. The S33 principal tension stress field on the skins of sides under load case 1

The large S33 principal compression stress area is shown in figure 4.70.

As we can see, the maximum S11 and S33 stresses on the skins of sides are both lower than the stress thresholds of the epoxy and ramie fibers.

Analysis of the airplane interior cabin bin (Hatrack)

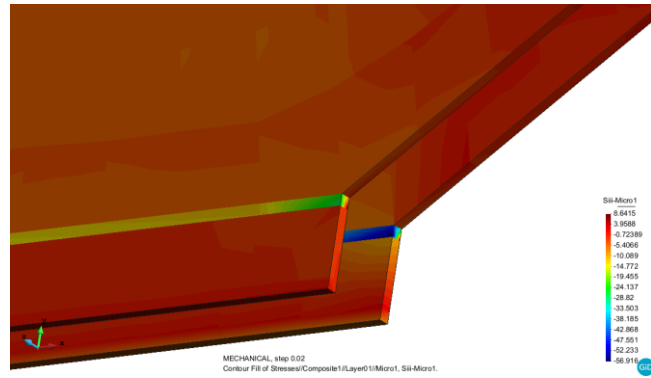


Figure 4.70. The large S33 principal compression stresses on the skins of sides under load case 1

Core

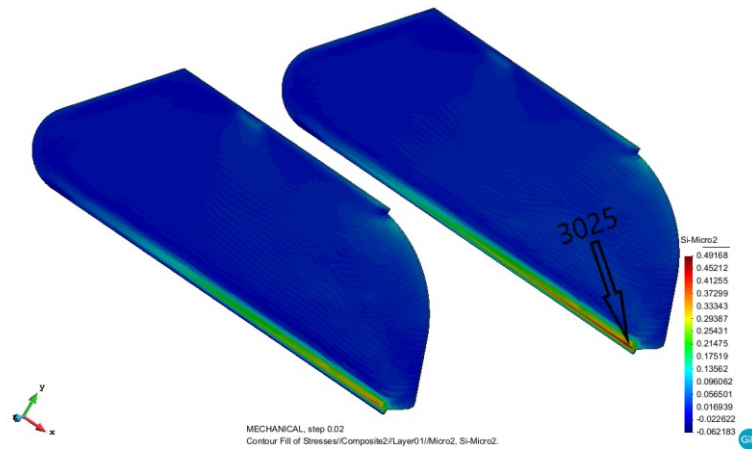


Figure 4.71. The S11 principal tension stress field on the cores of sides under load case 1

Figure 4.71 shows the S11 principal tension stress field on the cores of the sides. Like the situation we have discussed about the plates, the core of the sandwich structure has undertaken much smaller stresses compared to skins. The large S11 stresses are appearing on the areas around the cross areas between the cores of sides and plates. The maximum S11 stress is 0.42298 MPa . On other areas on the cores of the sides, the S11 stresses are small.

The chosen element for showing the microscopic S11 stress is element 3025, whose location is shown in figure 4.71. The microscopic S11 principal tension stress field on the RVE of element 3025 is shown in figure 4.72 and its maximum S11 stress is 123.94 MPa .

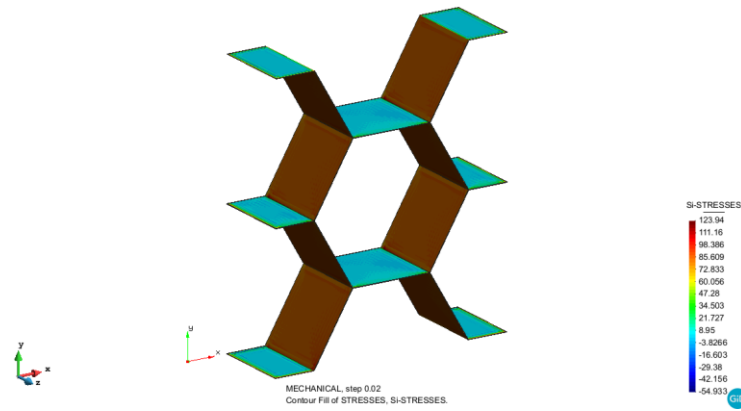


Figure 4.72. The microscopic S11 stresses on the RVE_02 of element 3025

The S33 principal compression stress field on the cores of the sides is shown in figure 4.73. The large S33 stresses appear on the bottom faces of the cores. The maximum S33 stresses appear on the bottom faces of the cores and its value is -0.99005 MPa . The element 3092 has been chosen to show the microscopic S33 stress and its location is shown in figure 4.73.

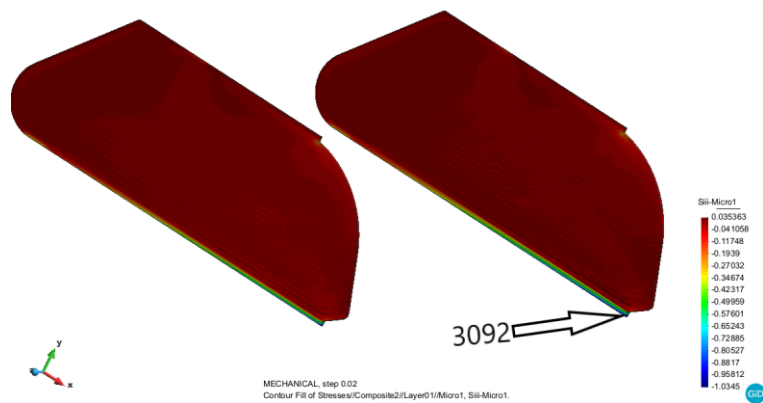


Figure 4.73. The S33 principal compression stress field on the cores of sides under load case 1

As we can see from figure 4.74, the microscopic S33 stresses on the RVE of element 3092 are very large. The maximum S33 stress is -198.48 MPa .

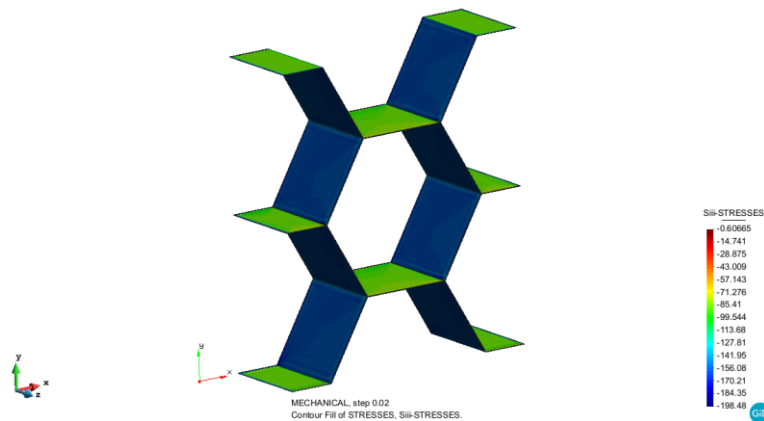


Figure 4.74. The microscopic S33 stresses on the RVE_02 of element 3092

Analysis of the airplane interior cabin bin (Hatrack)

As we can see, the maximum S11 and S33 stresses on the cores of sides are both lower than the stress thresholds of the honeycomb structure as a simple material, which is 2.4 MPa.

iii. Back area

Skin

The S11 principal tension stress field on the skins of the back part is shown in figure 4.75. Like the above results that we have seen, on the most areas of the skins, the S11 stresses are small. However, the area around the boundary condition area on the bottom of the back part has large stresses. The maximum S11 stress is 15.586 MPa and it is smaller than the its corresponding value in the load case 1 in part 4.2.2.

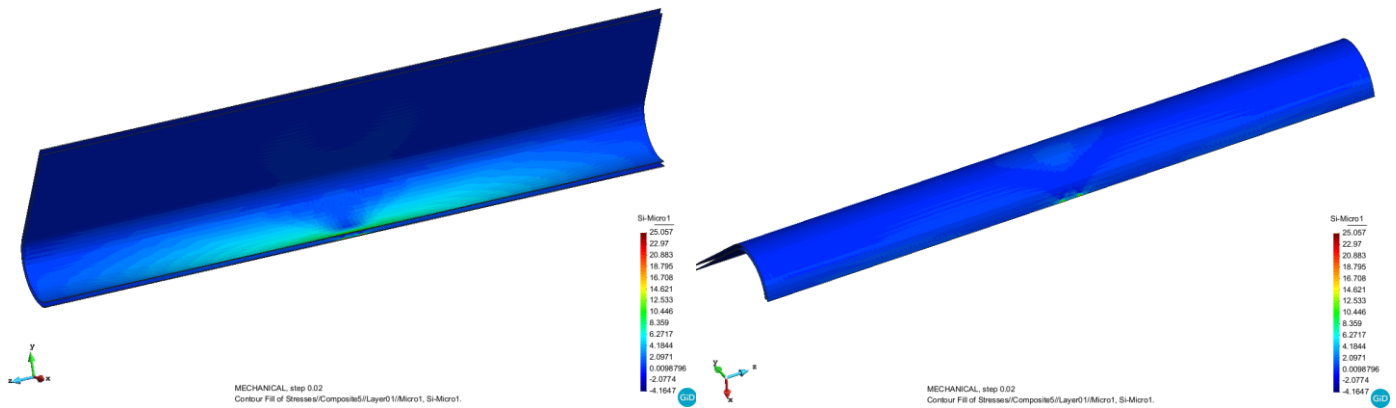


Figure 4.75. The S11 principal tension stress field on the skins of back part under load case 1

The S33 principal compression stress field on the skins of the back part has been shown in figure 4.76. Similar to what we have discussed about the S11 stress field, the large S33 stresses are also appearing around the area where the bottom boundary condition has been applied on. And on other areas of the back part, the S33 stresses are not large. The value of the maximum S33 compression stress is -22.277 MPa. As a comparison, the maximum S33 stress on the skins of the back part in the load case 1 in part 4.2.2 is -25.016 MPa. Therefore, the eco-composites help the structure to decrease its stress field on the skins of the back part.

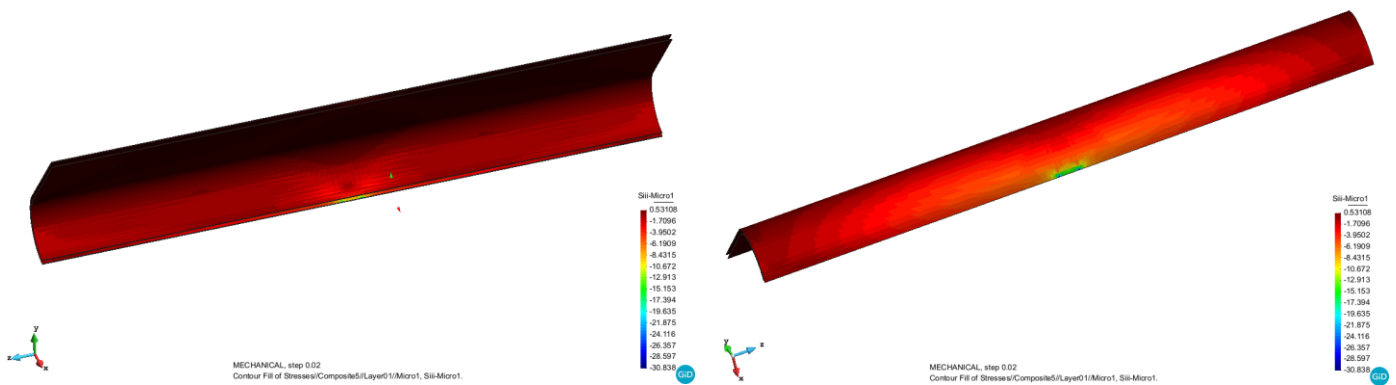


Figure 4.76. The S33 principal compression stress field on the skins of back part under load case 1

As we can see, the maximum S11 and S33 stresses on the skins of back part are both lower than the stress thresholds of the epoxy and ramie fibers.

Core

The S11 principal tension stress field on the core of the back part is shown in figure 4.77. Around the bottom boundary condition area on the back part, the S11 stresses are large. And this area with large S11 stresses is shown in red color. On other areas of the core, the S11 stresses are not large. The maximum S11 stress is 0.17882 MPa. Figure 4.77 also gives the locations of the element 53437 and element 38571 that we will use to show the microscopic stresses.

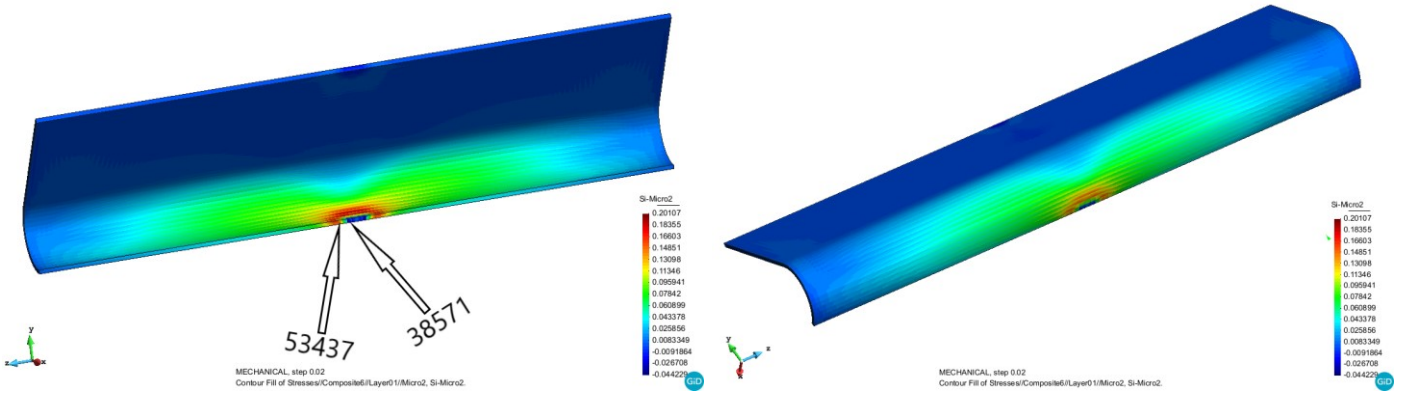


Figure 4.77. The S11 principal tension stress field on the core of back part under load case 1

Figure 4.78 shows the microscopic S11 principal tension stress field on the RVE of element 53437. The maximum S11 stress is 103.75 MPa.

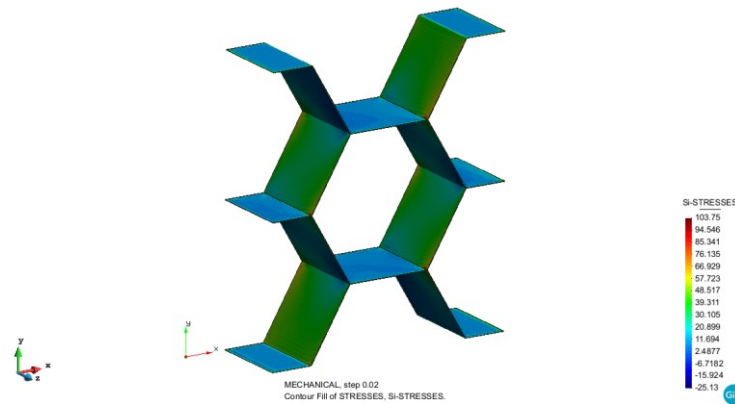


Figure 4.78. The microscopic S11 stresses on the RVE_02 of element 53437

The S33 principal compression stress field on the core of the back part is shown in figure 4.79. The maximum S33 stress happens on the bottom boundary condition area on the core and its value is -0.29068 MPa.

Analysis of the airplane interior cabin bin (Hatrack)

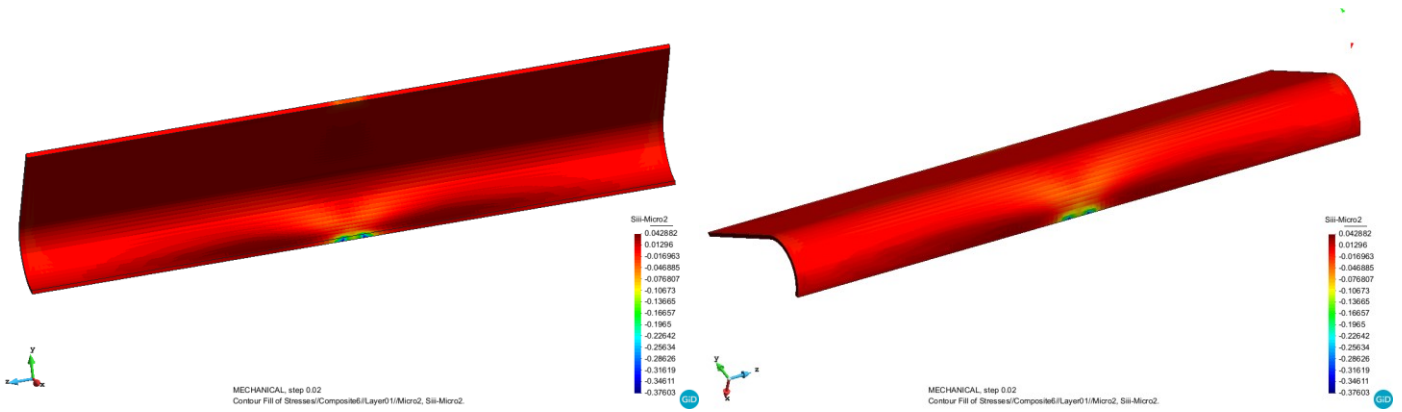


Figure 4.79. The S33 principal compression stress field on the core of back part under load case 1

The microscopic S33 principal tension stress field on the RVE of element 38571 is shown in figure 4.80. The maximum S33 stress is $-124.29 MPa$.

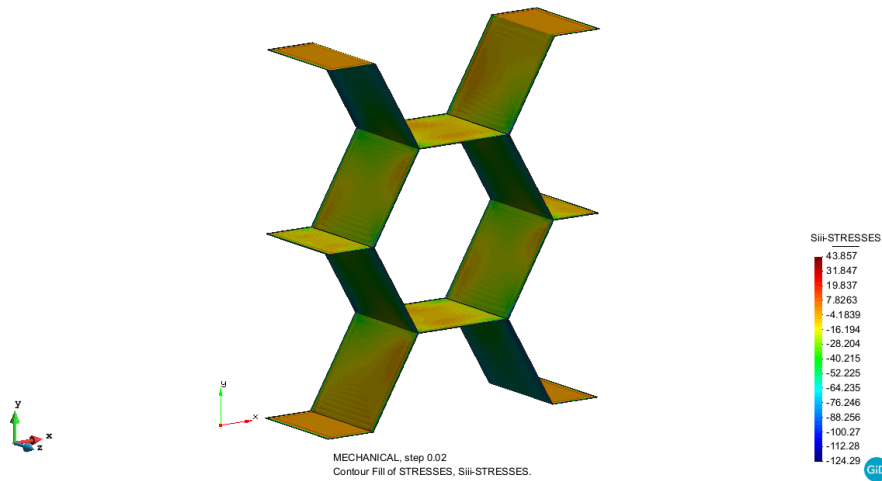


Figure 4.80. The microscopic S33 stresses on the RVE_02 of element 38571

As we can see, the maximum S11 and S33 stresses on the cores of back part are both lower than the stress thresholds of the honeycomb structure as a simple material, which is $2.4 MPa$.

Bending stress field

The bending stress field will only be discussed on the bottom plate, as the bending effects are much clearer on this region. The directions of the bending Stresses S_{xx} and S_{yy} have already been shown in above figure 4.24.

Skin

The S_{xx} bending stress field on the skins of the plates is shown in figure 4.81. The skins on the upside plate have small stresses. The large tension stresses occur on the bottom condition area on the inside skin. For the

Analysis of the airplane interior cabin bin (Hatrack)

compression stresses, we can also find the large stresses on the bottom condition area and the areas around it. The RVEs are chosen from this area to show the Sxx stresses and their numbers are 24102 and 24598, which are respectively located on the bottom boundary condition area on the inside skin and the outer skin. Figure 4.81 also shows the positions of these two elements.

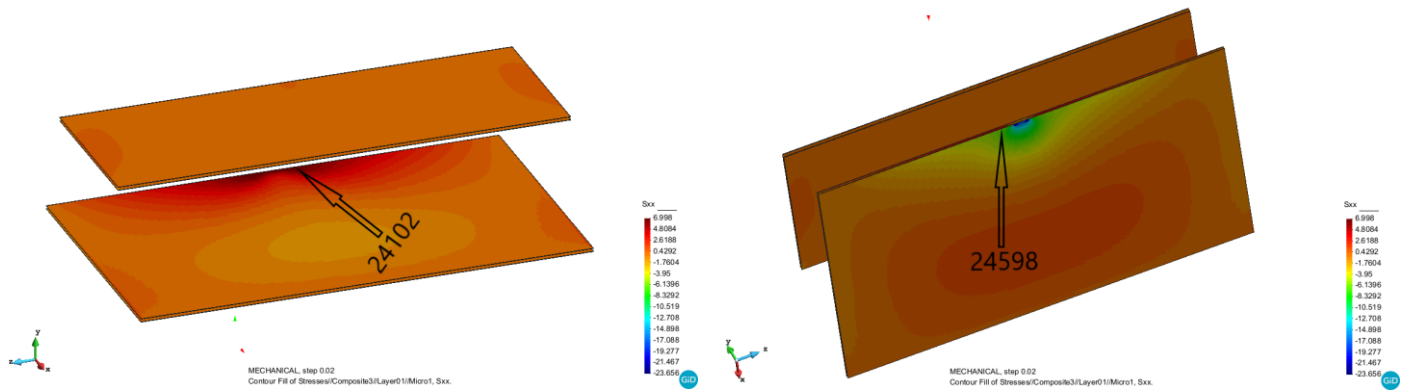
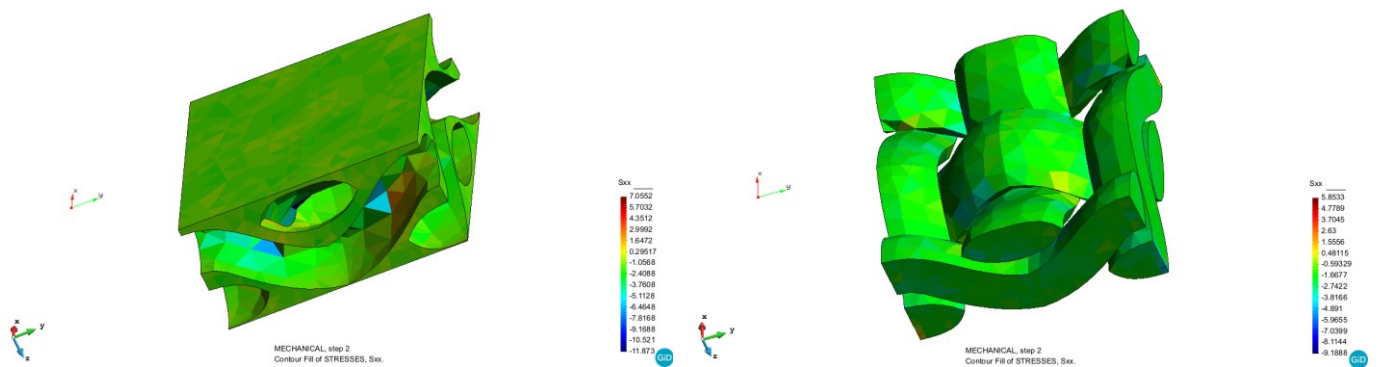


Figure 4.81. The Sxx bending stress field on the skins of plates under load case 1

Figure 4.82 shows the microscopic Sxx stress field on the RVEs of element 24102 and element 24598. From this this figure we can see that the matrix has undertaken larger stresses than the fibers. As we discussed above, the microscopic stresses are close to the macroscopic stresses in RVE_01. For the RVE of element 24102, the maximum Sxx tension stress and compression stress both happen on the matrix and their values are 7.0552 MPa and -11.873 MPa. The situation is same for the RVE of element 24598. The maximum Sxx tension and compression stresses are also found on the matrix and their values are 9.858 MPa and -12.255 MPa.



Analysis of the airplane interior cabin bin (Hatrack)

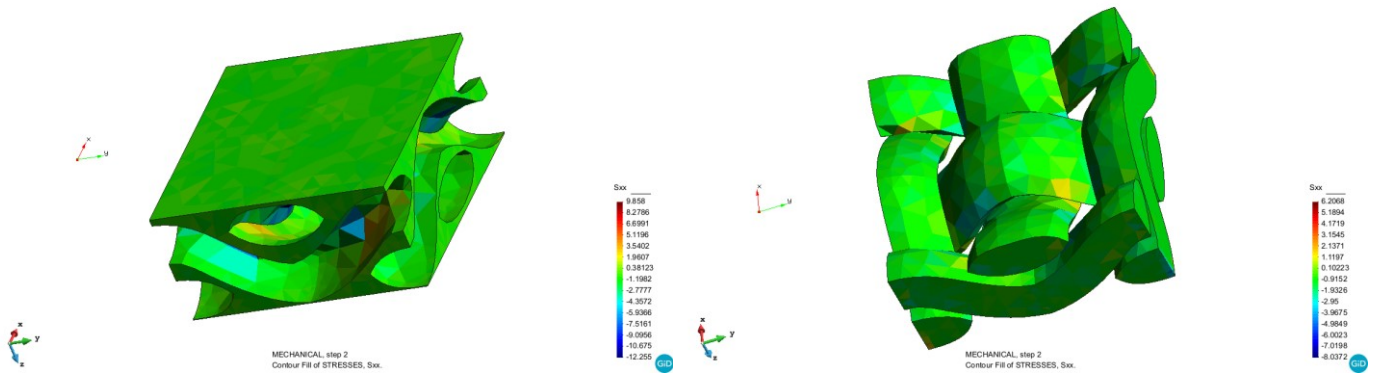


Figure 4.82. The microscopic Sxx bending stress field on the RVE_01 of element 24102 and element 24598 (Up: 24102, down:24598, left: matrix, right: fibers)

The Szz bending stress field on the skins of the plates is shown in figure 4.83. For the inside skin of the bottom plate, the bottom boundary condition area and the two front corners possess large tension stresses. On the front and middle area, we can find the large compression stresses. As we can see, the situation of the outer skin of the bottom plate is converse. The chosen RVEs are from above areas on the skins of the bottom plate. Figure 4.83 also shows the positions of element 25162, element 38707, element 38780 and element 39259, which are used to show the microscopic Sxx and Szz bending stresses.

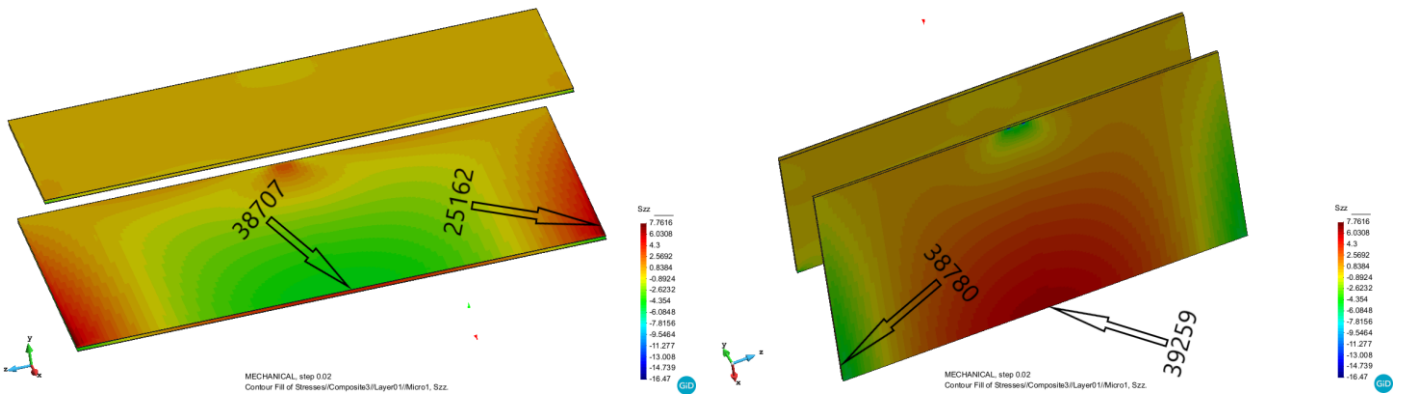


Figure 4.83. The Szz bending stress field on the skins of plates under load case 1

The microscopic Szz stress fields on the RVEs of element 24102 and element 24598 are shown in figure 4.84, representing bottom boundary condition area. We can see that the stresses on the matrix are much larger than the stresses on the fibers. The maximum Szz tension and compression stresses on the RVE of element 24102 are 3.4119 MPa and -5.0959 MPa . For the RVE of element 24598, the maximum Szz tension and compression stresses are 4.7173 MPa and -5.2403 MPa .

Analysis of the airplane interior cabin bin (Hatrack)

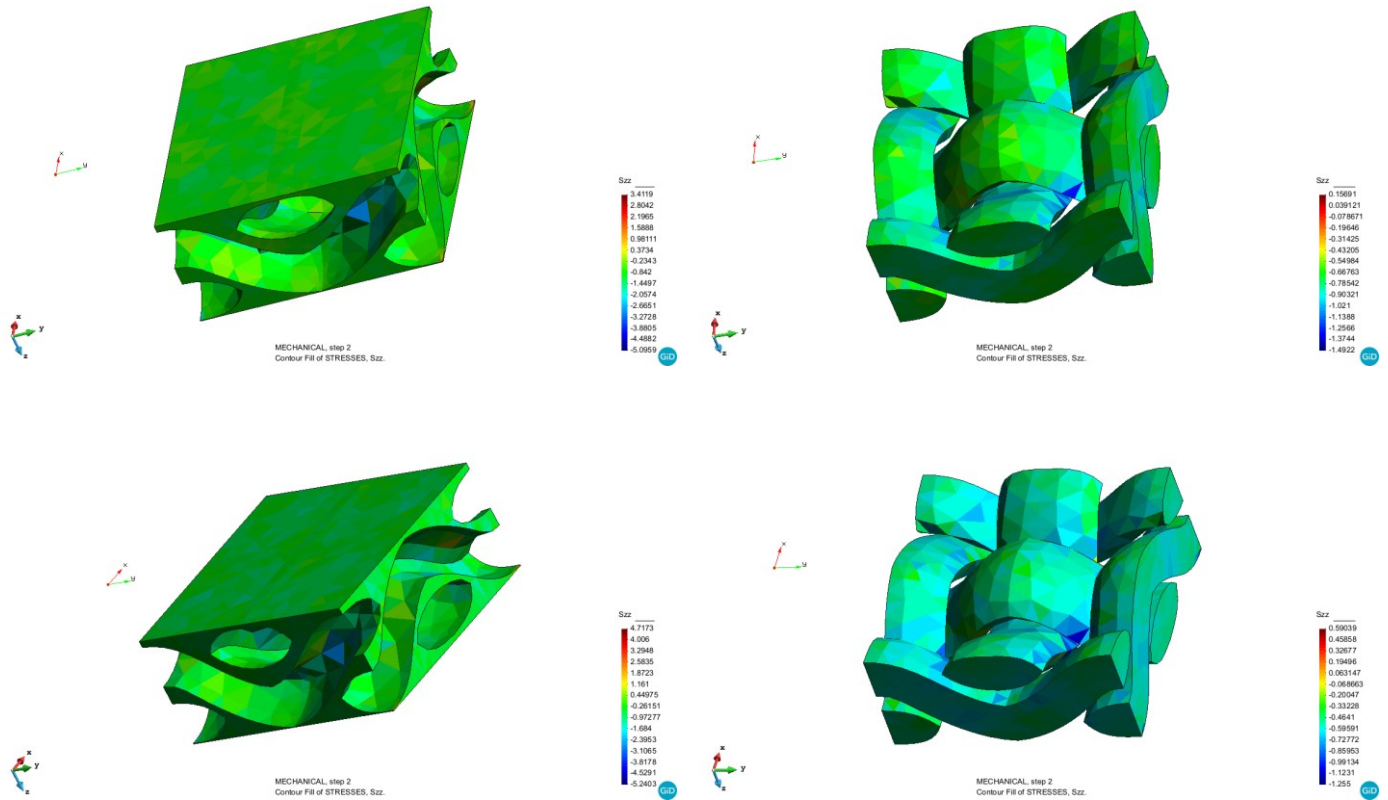
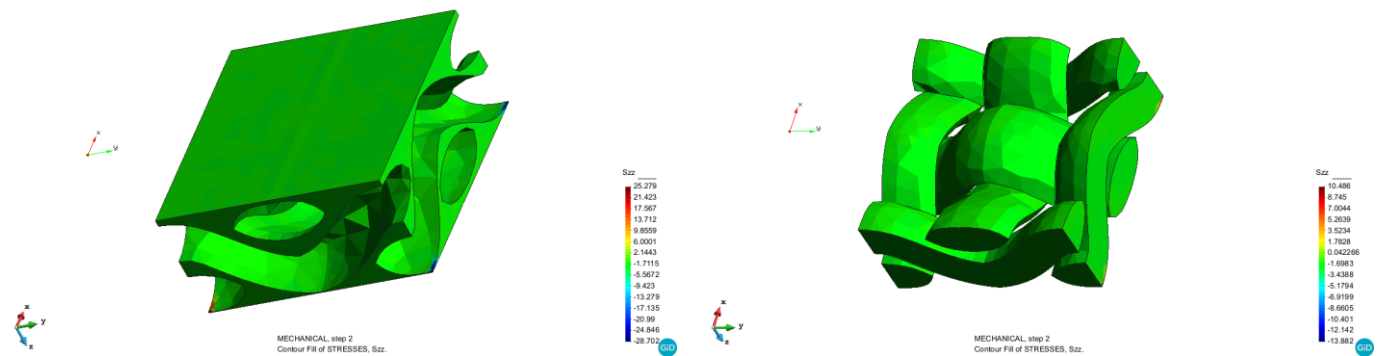


Figure 4.84. The microscopic Szz bending stress field on the RVE_01 of element 24102 and element 24598 (Up: 24102, down:24598, left: matrix, right: fibers)

The Szz stress fields on the RVEs of element 25162 and element 33780, located on the front corners on the skins of the bottom plate, are shown in figure 4.85. As it has been presented, the stresses on the matrix are still larger than the stresses on the fibers. The stresses are uniform on the most parts, including the matrix and the fibers. The maximum Szz tension and compression stresses on the RVE of element 25162 are 25.279 MPa and -28.702 MPa . For the RVE of element 33780, the maximum Szz tension and compression stresses are 13.746 MPa and -24.296 MPa .



Analysis of the airplane interior cabin bin (Hatrack)

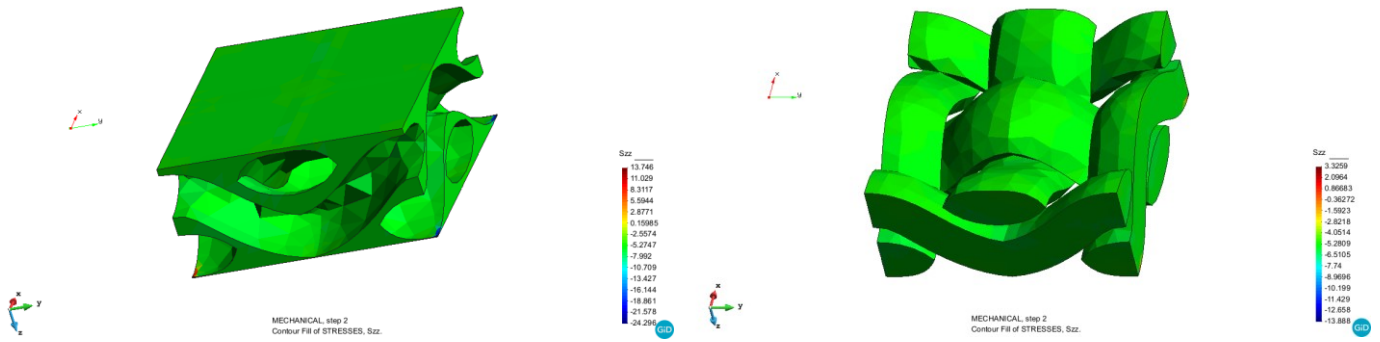


Figure 4.85. The microscopic Szz bending stress field on the RVE_01 of element 25162 and element 33780 (Up: 25162, down:33780, left: matrix, right: fibers)

The Szz stress fields on the RVEs of element 38707 and element 39259 is shown in figure 4.86 and they represent the front and middle area of the skins of the bottom plate. As we can see, the stresses on following RVEs are not uniform like we have seen above. For the element 38707, located on the inside skin, the matrix and the fibers are all under compression stresses and the maximum Szz compression stress in its RVE is -10.32 MPa and it appears on the matrix. Conversely, for the RVE of element 39259 which is on the outer skin, the stresses are tension stresses and the maximum tension stress in its RVE is also found on the matrix with the value 9.6566 MPa .

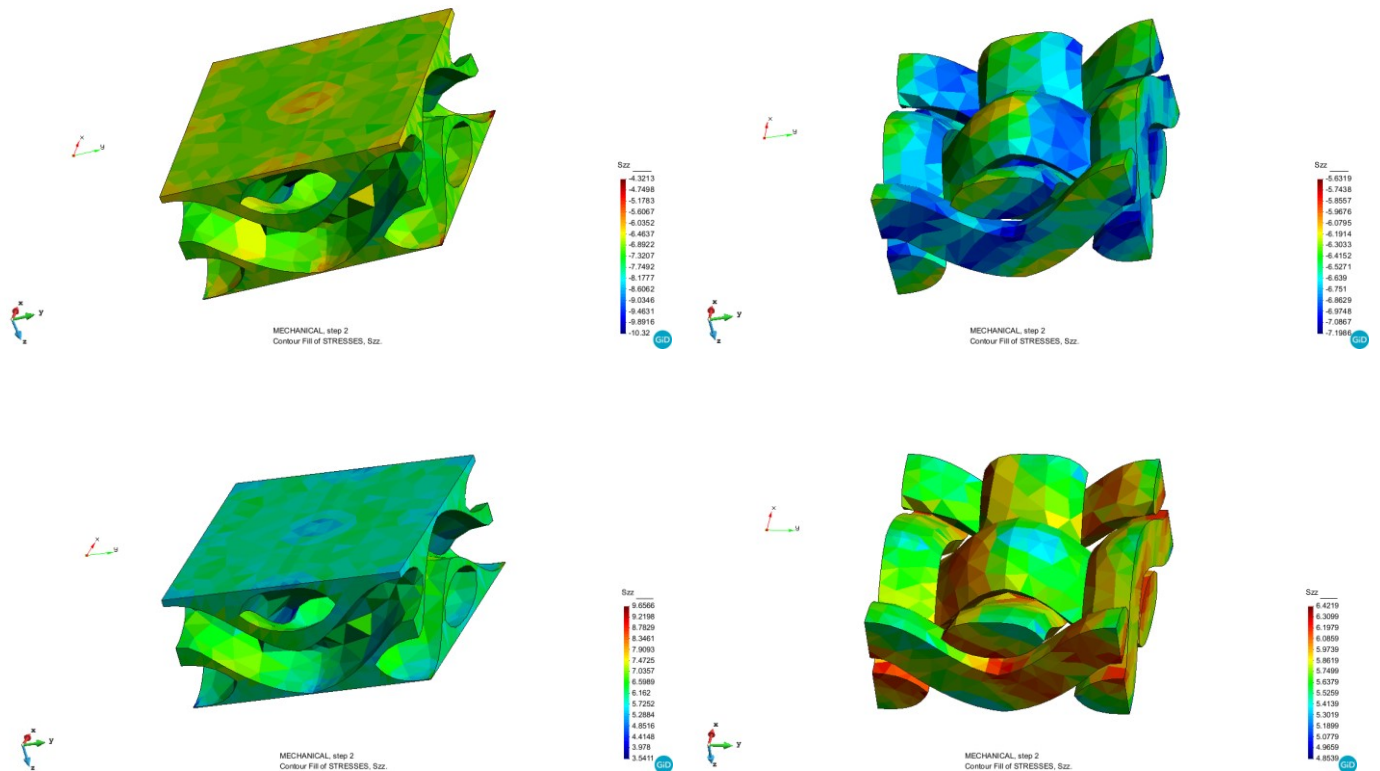


Figure 4.86. The microscopic Szz bending stress field on the RVE_01 of element 38707 and element 39259 (Up: 38707, down:39259, left: matrix, right: fibers)

Core

Analysis of the airplane interior cabin bin (Hatrack)

The S_{xx} bending stress field on the cores of the plates is shown in figure 4.87. On the bottom boundary condition area, the large compression stresses can be found. For the large tension stresses, they are happening on the area near the bottom boundary condition and the two front corners of the bottom core. As we have discussed above about the principal stresses, the stresses on the cores are much smaller than the stresses on the skins. The results are same for the bending stresses in this part. However, since the honeycomb structure has very large empty spaces and the macroscopic stresses have been derived from the volumetric average of the stresses in the RVE, the real stresses will be much larger on the honeycomb structure. Therefore, the material used to manufacture the honeycomb cores should possess high stiffness and high strength.

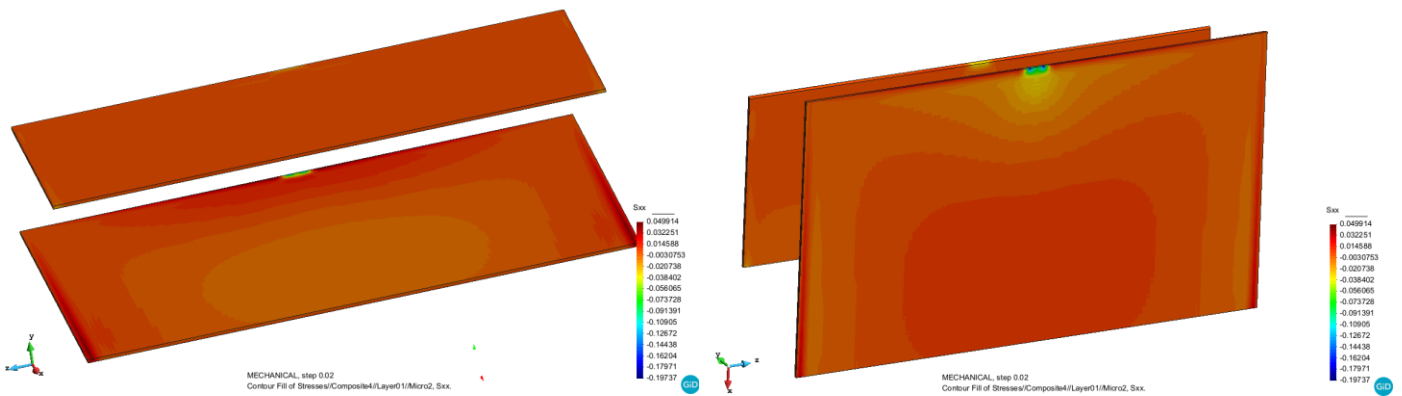


Figure 4.87. The S_{xx} bending stress field on the cores of plates under load case 1

The S_{xx} stress field on the RVE of element 60734 (Shown in figure 4.63), located on the left side of the bottom core, is shown in figure 4.88. On this RVE, the stresses are much larger than the macroscopic stresses on the cores. This result proves that the existence of the empty spaces in the RVE leads to the huge increases of the microscopic stresses compared to the macroscopic stresses. The maximum S_{xx} tension and compression stresses in the RVE of element 60734 are 35.15 MPa and -15.047 MPa .

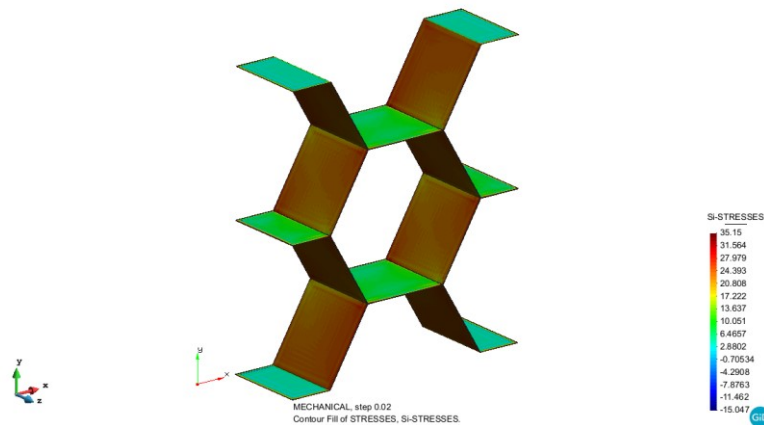


Figure 4.88. The microscopic S_{xx} bending stress field on the RVE_02 of element 60734

The RVEs in figure 4.89 are selected from the bottom boundary condition area and this figure has shown the S_{xx} stress field on these RVEs. The elements are 38672 and 24353 (Shown in figure 4.63). As we can see,

Analysis of the airplane interior cabin bin (Hatrack)

both RVEs have large compression stresses. The RVE of element 24353 also has very large tension stresses. The maximum Sxx tension and compression stresses in the RVE of element 38672 are 13.058 MPa and -38.425 MPa. For the RVE of element 24353, the maximum tension and compression stresses are 30.094 MPa and -33.717 MPa.

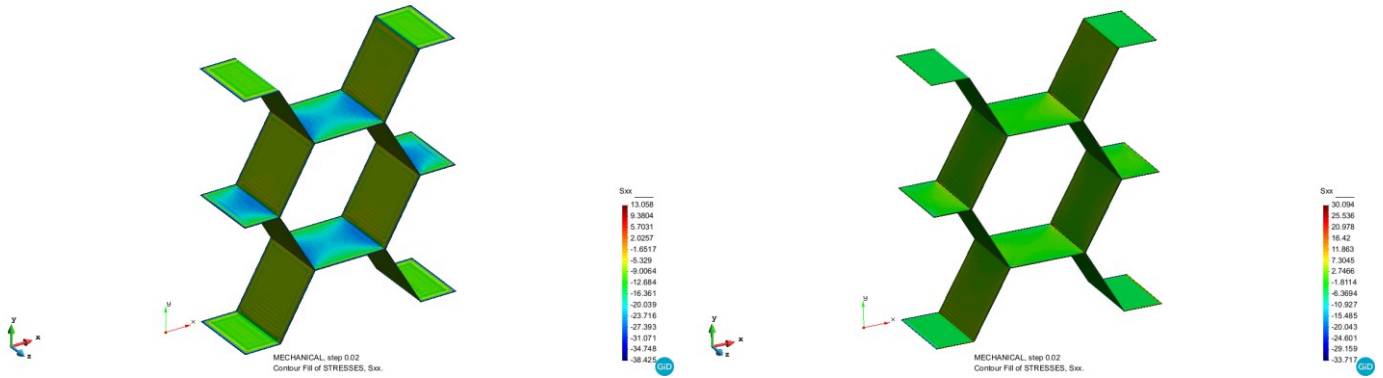


Figure 4.89. The microscopic Sxx bending stress field on the RVE_02 of element 38672 and element 24353 (Left: 38672, right: 24353)

The Szz bending stress field on the cores of the plates is shown in figure 4.90. The bottom boundary condition area, the two front corners and the front and middle area of the bottom core have both large tension and compression stresses.

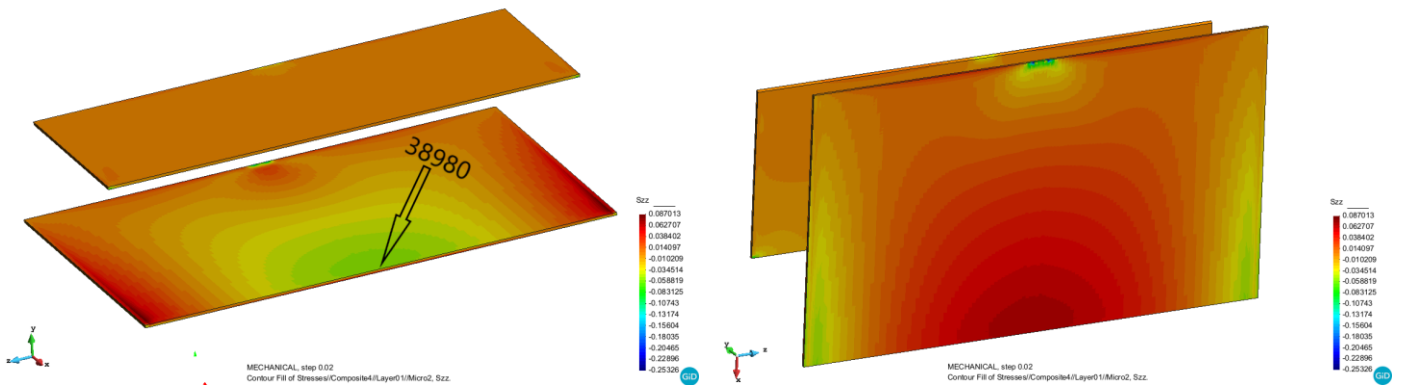


Figure 4.90. The Szz bending stress field on the cores of plates under load case 1

Figure 4.91 shows the Szz bending stress field on the RVE of element 60734 (Shown in figure 4.63) selected from the left front corner of the bottom core. The maximum Szz tension and compression stresses are 12.814 MPa and -16.774 MPa. The position of element 38980 is also shown in figure 4.91.

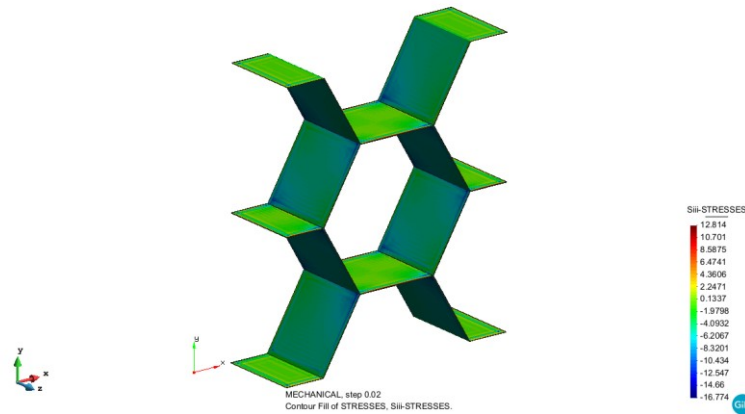


Figure 4.91. The microscopic S_{zz} bending stress field on the RVE_02 of element 60735

The S_{zz} bending stress field on the element 38672 and element 24353 (Shown in figure 4.63) has been shown in figure 4.92 and these two elements are located on the bottom boundary condition area. The compression stresses are large on these two RVEs and the tension stresses on the RVE of element 38672 are also large. The maximum S_{zz} tension and compression stresses on the RVE of element 38672 are 20.818 MPa and -30.696 MPa . For the RVE of element 24353, the maximum S_{zz} tension and compression stresses are 9.9575 MPa and -19.641 MPa .

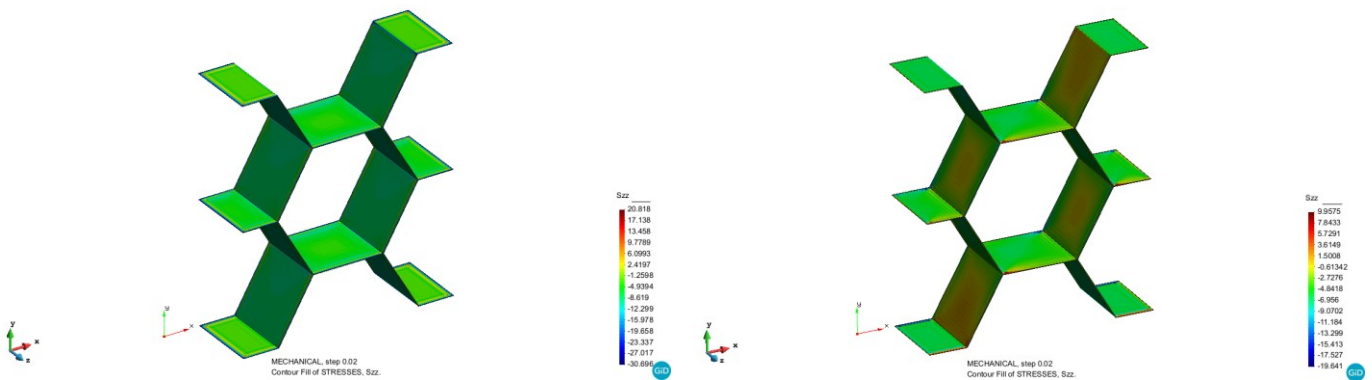


Figure 4.92. The microscopic S_{zz} bending stress field on the RVE_02 of element 38672 and element 24353 (Left: 38672, right: 24353)

Another area where the S_{zz} stresses are large is the front and middle area of the bottom core. Therefore, the element 38980 has been selected and the S_{zz} stress field on the RVE of this element is shown in figure 4.93. As we can see, this RVE is under compression stresses. And the maximum S_{zz} compression stress is -6.061 MPa .

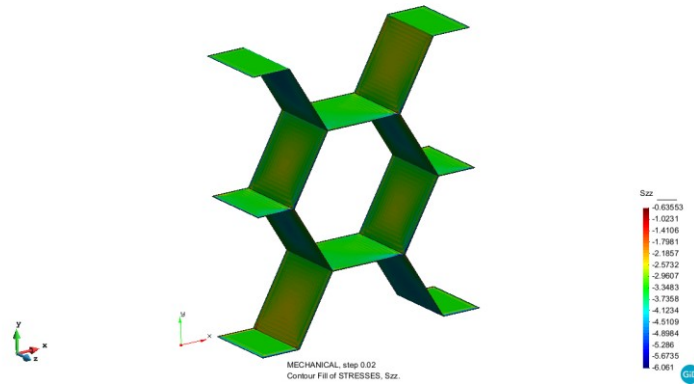


Figure 4.93. The microscopic Szz bending stress field on the RVE_02 of element 38980

Comparison

Table 4.9 shows that the application of the eco-composites has decreased the S11 and S33 stresses on the skins of the structure compared to the former design with isotropic materials.

The maximum S11 and S33 stresses on different skin parts of the cabin bin				
Skins	Isotropic materials (S11, MPa)	Eco-composites (S11, MPa)	Isotropic materials (S33, MPa)	Eco-composites (S33, MPa)
Skin of the plates	15.554	13.823	-41.822	-34.798
Skin of the sides	29.539	27.028	-51.369	-40.873
Skin of the back part	19.905	15.586	-25.016	-22.277

Table 4.9. The maximum S11 and S33 stresses on different skin parts of the cabin bin

Table 4.10 has shown the comparison between the S11 and S33 stresses on the cores of the structure under the situations that the eco-composites are implemented or not and this comparison is based on the average perspective. From table we can see that the application of the eco-composites will increase the S11 and S33 stresses on the core parts of the cabin bin even from an average perspective. Actually, the stresses on the cores will increase significantly, leading to the demand to use highly stiff and highly strong materials for the cores.

The maximum S11 and S33 stresses on different core parts of the cabin bin				
Cores	Isotropic materials (S11, MPa)	Eco-composites (S11, MPa)	Isotropic materials (S33, MPa)	Eco-composites (S33, MPa)
Core of the plates	0.08534	0.13217	-0.15684	-0.34478
Core of the sides	0.15557	0.42298	-0.45437	-0.99005
Core of the back part	0.14193	0.17882	-0.16354	-0.29068

Table 4.10. The maximum S11 and S33 stresses on different core parts of the cabin bin

4.3.3 Conclusions

i) The application of eco-composites has helped the structure to decrease its stress field on the skins of the structure. However, the stresses on the core parts will become much larger than the situation of using isotropic materials.

ii) The areas where the large S11 and S33 stresses have appeared on need reinforcements to protect the structure from being damaged.

iii) Because of the large empty spaces of the eco-honeycomb RVE model and the computation procedure that the macroscopic stresses are calculated by taking the volumetric average of the microscopic stresses in the RVE, the stresses on the honeycomb core are actually much larger than the stresses shown in macroscopic scale. As a result, it is needed to analyze the performance of the RVE in order to study the real stresses on the cores when the average stresses on the macroscopic scale have not provided this information.

iv) The stresses on the cabin bin with isotropic materials or eco-composites are all lower than the stress thresholds of corresponding materials.

5 Conclusions

Before the simulation works, the theories of FEM, multiscale homogenization and FE^2 homogenization procedure have been discussed. Through the presentations of these theories, the formulations and working flow behind PLCd code become clear, which is necessary for conducting this work. Then the following work has successfully simulated the simple supported beam and the cabin bin, under different load cases using the isotropic materials and eco-composites. And the analysis of the cabin bin made of eco-composites is conducted by using the multiscale analysis procedure. There are some conclusions given by the results.

First, from the beam model we can see that the solutions are convergent and the errors will be very small if we use enough elements. And using quadratic elements will give lower errors compared to using linear elements. Another conclusion is that the stress concentration will lead to errors on the area where it happens. Therefore, the MIN and MAX functions of GiD should be used to get real maximum stresses.

Then, for the simulation of the cabin bin with isotropic materials, the results show that the load case 1 (completely loaded cabin bin) is more dangerous, even though the load case 2 (load applied only to half of the cabin bin) will add a torque force on the structure. And the areas where the stresses are large are upside boundary condition area on the sides, bottom boundary condition area on the bottom plate and the back part, and the cross areas between the sides and bottom plates. In order to reduce the stress concentrations, we can take measurements like replacing the materials on these area with stiffer materials. The conclusion about the sandwich structure is that the core parts have undertaken much smaller stresses, which allows us to use the lighter material for the cores to decrease the weight of the structure.

For the simulation of the cabin bin with eco-composites using multiscale analysis procedure, the first conclusion is that the application of the eco-composites will decrease the stress field on the skins of the structure. For the core parts, the actual stresses on the cores will increase because of the large empty spaces in the honeycomb structure. However, the macroscopic stresses on the cores will keep very small since the computation of the macroscopic stresses is taking the volumetric average of the microscopic stresses in the RVE. For the increases of stresses on the core parts after using the eco-composites, we can avoid the damage by using the material with high stiffness and high strength. As a result, the benefit of sandwich structure that it will help the structure to decrease its weight can be achieved safely.

The last conclusion is that the stresses on the cabin bin with isotropic materials or eco-composites are all lower than the stress thresholds of corresponding materials.

6 References

- [1] Bachmann, J.; Yi, X.; Gong, H.; Martinez, X.; Tserpes, K.; Ramon, E.; Paris, C.; Moreira, P.; Fang, Z.; Li, Y.; et al. *Outlook on ecologically improved composites for aviation interior and secondary structures*. CEAS Aeronaut. J. 2018, 9, 533-543.
- [2] PLCd-Manual. *Non-linear thermomechanic finite element code*, developed at CIMNE, 1991-present.
(<https://web.cimne.upc.edu/users/plcd/>)
- [3] C. Truesdell; R. Toupin. *The Classical Field Theories, Handbuch der Physik III/I*. Springer-Verlag, Berlin, 1960.
- [4] Oller, S.; Neamtu, L.; & Oñate, E. *Una generalización de la teoría de mezclas clásica para el tratamiento de compuestos en serie/paralelo*. Congreso Nacional de Materiales Compuestos, pp. 433-438, 1995.
- [5] Oñate, E.; Neamtu, L.; & Oller, S. *Un modelo constitutivo para el análisis por el “MEF” para materiales compuestos*. In J. Güemes & C. Navarro (Eds.), *Materiales Compuestos '97*, pp. 206-211, 1997.
- [6] Otero, F; Oller, S; & Martínez, X. *Multiscale Computational Homogenization: Review and Proposal of a New Enhanced-First-Order Method*. Volume 25, Issue 2, pp. 479-505, 2018.
- [7] Ostoja-Starzewski, M. *Microstructural Randomness Versus Representative Volume Element in Thermo-mechanics*. Journal of Applied Mechanics, 69(1):25-35, 2002.
- [8] Oñate, E. *Introduction to the finite element method*. CIMNE, Lectures for the master program of computational mechanics, 2008
- [9] Otero, F. *Multiscale Numerical Modelling of Microstructured Reinforced Composites*, PhD thesis, Escola Técnica Superior d'Enginyers de Camins, Canals i Ports de Barcelona, Universidad Politècnica de Catalunya, 2015. Advisor: Oller, S; Martínez, X.
- [10] R. Hill. *A self-consistent mechanics of composite materials*. Journal of the Mechanics and Physics of Solids, 13(4):213-222, 1965.
- [11] J. Mandel. *Plasticite Classique Et Viscoplasticite*. International Centre for Mechanical Sciences, Courses and lectures, Springer-Verlag, Udine, 1971.
- [12] Frederic Feyel. *Multiscale FE² elastoviscoplastic analysis of composite structures*, Computational Materials Science, 16:344-354, 1999.
- [13] Frederic Feyel. *A multilevel finite element method (FE²) to describe the response of highly non-linear structures using generalized continua*, Comput. Methods Appl. Mech. Engrg, 192:3233–3244, 2003.
- [14] Otero, F; Martínez, X; & Oller, S. *An efficient multi-scale method for non-linear analysis of composite structures*. Composite Structure, Volume 131, pp.707-719, 2015
- [15] BASF Corporation. *Divinycell F: properties data*. (<https://aerospace.basf.com/>)

References

- [16] Gruit Group. *General Datasheet: PF 811*. (<https://www.gurit.com/>)
- [17] Hexcel Corporation. *HexWeb® A1 and A10: product data*. (<http://www.hexcel.com/>)
- [18] Simmons (Mouldings) Ltd. *Epoxy resin*. (<http://www.epoxyworktops.com/>)
- [19] Doshi Group. *Ramie fiber*. (<http://www.doshi-group.com/>)